Effect of Cooling Circuit Duration on Formation of Solidification Shrinkage in A356 Casting Automotive Wheels

Rafael Jung Hoon Lee

A Thesis submitted to
Auckland University of Technology
in partial fulfilment of the requirements for the degree of
Master of Engineering (ME)

2006

School of Engineering

Primary Supervisor: Zhan Chen

Acknowledgements

It has been a long four year journey to finish this research and there are so many people who have helped me through this journey to whom I would like to express my gratitude.

First, my industrial supervisor Dr. Darius Singh. Darius, I would like to thank you for the support and inspiration that you have given me from day one. Your passion for what you do has been a huge influence on me and shaped who I am as an engineer today. Also your great skills on Power Point presentations and diagrams have been so inspirational!

My academic supervisor, Dr. Zhan Chen. I don't know where to begin. I am just so grateful that you never hesitated to tell me when I was doing things wrong. Looking back, all I can say is "thank you" for guiding me to the right place. I am also thankful for your endless patience, waiting for me to complete this work. One just wonders how it is ever possible to be so patient.

There is another group of people to whom I would like to show my deepest gratitude. Everyone that I have worked with at ION Automotive of New Zealand, I am deeply sad how everything turned out at the end, but I want to thank every one of you for giving me the valuable opportunity to grow in every possible way. I had a great time working with you all and I wish you all the very best.

To my family, especially my Mum and Dad. Dad, thank you for your phone call every week reminding me about this research. Mum, thank you for your humour and optimism that helped me through. But most of all, just "thank you" for everything you have done over the past 27 odd years.

A big thank you to all my friends, thank you for that question you always asked me - "how is your thesis going?" Now I can say, "I have done it!"

Finally nearly last but definitely not the least …

To my lovely wife and best friend Adithi.

Thank you.

Thank you for your faith in me, you knew from day one that I could do this.
Thank you for your patience, you never made me feel pressured. Only now I know how grateful I am for that.
Thank you for just being there in my life, that's all I can say.
Really, nothing that I say can express how grateful I am for you in everyway.

Thank you God for helping me through this!

To Meroo, Chutney, Rusty and Teenie House Forever!

Abstract

Low Pressure Die Casting (LPDC) process is one the most common casting process to produce structural automotive components, such as alloy wheels and suspension components. It has been identified that cavity filling and solidification process are two most critical aspects to produce premium quality casting components.

During the solidification process of casting alloy, it is a well known phenomenon that metal experiences volumetric shrinkage due to its density difference between liquid and solid phase. When this volumetric shrinkage is not properly compensated, then a casting defect commonly known as solidification shrinkage occurs. The solidification shrinkage has very detrimental effects on structural integrity required for premium quality casting such as aluminium alloy wheels.

Literature and practical experiences of foundry men show that it is critical to achieve unidirectional solidification pattern by avoiding an isolated hot spot in order to minimise the solidification shrinkage. However, it is found that the geometry of industrial casting applications is often constrained by other design factors that would not naturally avoid these isolated hot spots. The subject of this research, aluminium alloy wheels, is not excluded from this constraint.

In aluminium alloy wheels, an isolated hot spot is commonly observed in an area known as rim and spoke junction due to its geometry constraints. Consequently, the solidification shrinkage is commonly experienced, which is undesirable due to its detrimental effects for the structural integrity of alloy wheels. In order to minimise the solidification shrinkage, forced cooling method is applied to avoid an isolated hot spot. The control of this forced cooling is achieved by cooling media, flow rate of cooling media and duration cooling circuit.

Foundry experiments in industrial environment were conducted producing aluminium alloy wheels using commercially treated A356 (Al-Si) alloy, where different durations of cooling circuit were used to understand the sensitivity of solidification shrinkage formation to the duration of cooling circuit. This was followed by metallurgical structure analysis and numerical modelling to suggest the sensitivity of cooling circuit duration in controlling solidification shrinkage.

The major finding conclusion of this research is that control of the shrinkage formation is not very sensitive to the duration cooling circuit. It is suggested that as casting solidifies initially from the mould wall, it retracts away from the cast-mould interface due to thermal contraction. Consequently, air gap is formed between casting and mould interface, creating an effective thermal resistance layer. Thereafter, heat transfer across the cast-mould interface is not sensitive to the change in the cooling channel which is a distance to the cast-mould interface.

Some limitations of numerical modelling and metallurgical analysis were also identified during this research and recommendations were made to improve the accuracy of local hot spot prediction in production of aluminium alloy wheels. More specifically, numerical modelling of the effect of grain refinement and use of non homogeneous material property (particularly fraction of solid) for rapidly chilled area. Fraction of eutectic rather than secondary dendrites arm spacing is a proper microstructure parameter that can be used to locate the hot spot.

Table of Contents

Table of Figures

1 Introduction

1.1 Wheel Manufacturing Process at ION Automotive

ION Automotive (ION) is a relatively large sized aluminium alloy casting manufacturer using low pressure die casting (LPDC) process. ION's main products are structural automotive components, such as aluminium alloy casting wheels and suspension cross members. Its Manukau based operation, employing up to 500 employees, has an annual production capacity of 1.75 million casting wheels and 10,000 suspension cross members.

In order to understand the significance of solidification process control on manufacturing of high quality casting products at ION, its manufacturing process needs to be discussed first. A schematic diagram of the overall manufacturing process of casting wheels at ION is shown in Figure 1-1. The manufacturing process can be categorised in to the following four distinctive stages as shown below.

- Melt preparation.
- Metal casting process.
- Machining process.
- Painting process.

In this introduction section, only the first two processes (Melt preparation, metal casting process) will be discussed as they are closely related to this research.

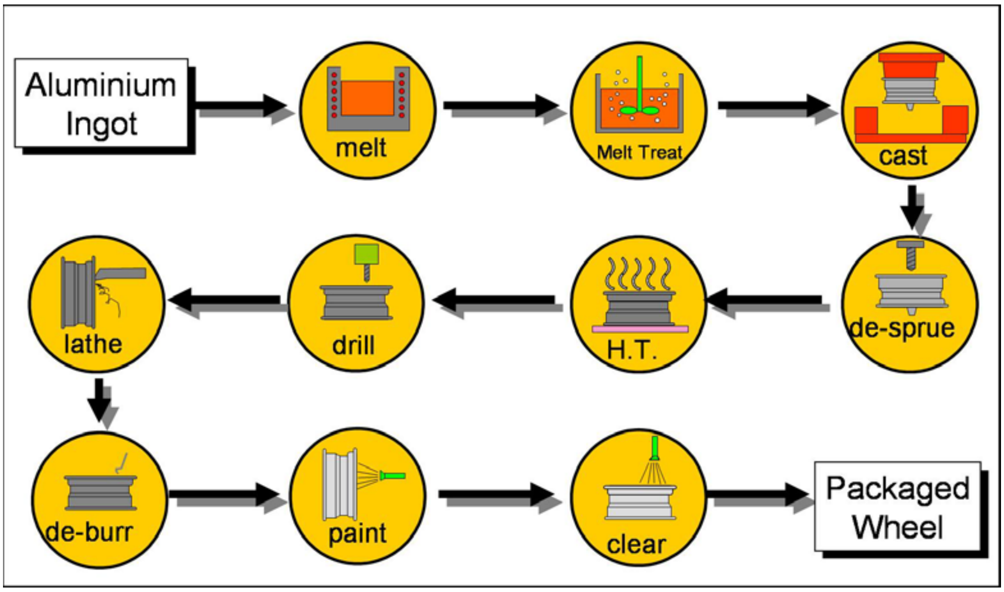

Figure 1-1 Overall manufacturing process of aluminium alloy casting wheels at ION Automotive.

1.1.1 Melt Preparation

Melt preparation process is the first step of the manufacturing process. Its primary purposes are to melt raw material and treat the molten metal to ensure that adequate metal quality is achieved.

For manufacturing casting wheels at ION, premium A356 aluminium alloy is used, whose composition is shown in Table 1-1. Raw material of A356 is supplied in a form of ingots from the local supplier. Then using two thirty tonne gas fired melting furnaces, ingots are melted and ready for melt treatment process.

Table 1-1 Alloy composition of typical A356 aluminium alloy. [1]

	Elements							
	Si	Fe	Cu	Mn	Mg	Zn	Ti	Al
Composition (%)	6.5-7.5	0.50	0.25	0.35	0.25-0.45	0.35	0.25	Balance

The primal purposes of melt treatment

Degassing – Molten aluminium has a very high solubility of hydrogen gas that can be absorbed from the moist in ambient air. Dissolved hydrogen gas in aluminium alloy can later on result in gas pores in casting products. Therefore it is necessary to treat the molten metal through degassing process.

Fluxing – Fluxing is a common term used in casting process to describe an addition of chloride or fluoride based salt. Cleaning of metal is provided by addition of fluxing salt that reacts with non-metallic inclusions in the melt. This reaction then form a cluster called dross, which can be separated from the melt.

Alloy addition – In the case of casting wheel manufacturing at ION, three main types of alloying elements are added in a form of aluminium master alloy.
Al-Mg: Mg is added to a specified level for A356, shown in Table 1-1, to provide required mechanical properties.

Al-Sr: Strontium is added in aluminium silicon alloy to provide modified eutectic structure, where eutectic is transformed from needle like structure to globular structure. It is shown that modified structure increases fatigue strength of aluminium silicon alloy.

Al-TiB: Titanium boride is added to provide nucleation sites for solidification of aluminium silicon alloy. Provision of increased number of nucleation sites results in much finer grain structure, which increases yield strength and fluidity of aluminium silicon alloy.

1.1.2 Metal Casting Process

At ION, Low Pressure Die Casting (LPDC) process was used to produce casting components. LPDC process is one of the most widely used casting processes in metal forming industry. Its relatively superior mechanical strength over other metal casting processes, gravity or high pressure die casting and low to medium capital make it most suitable for a mass production of premium structural applications (Casting wheels, suspension components etc.). A schematic diagram of LPDC is shown in Figure 1-2.

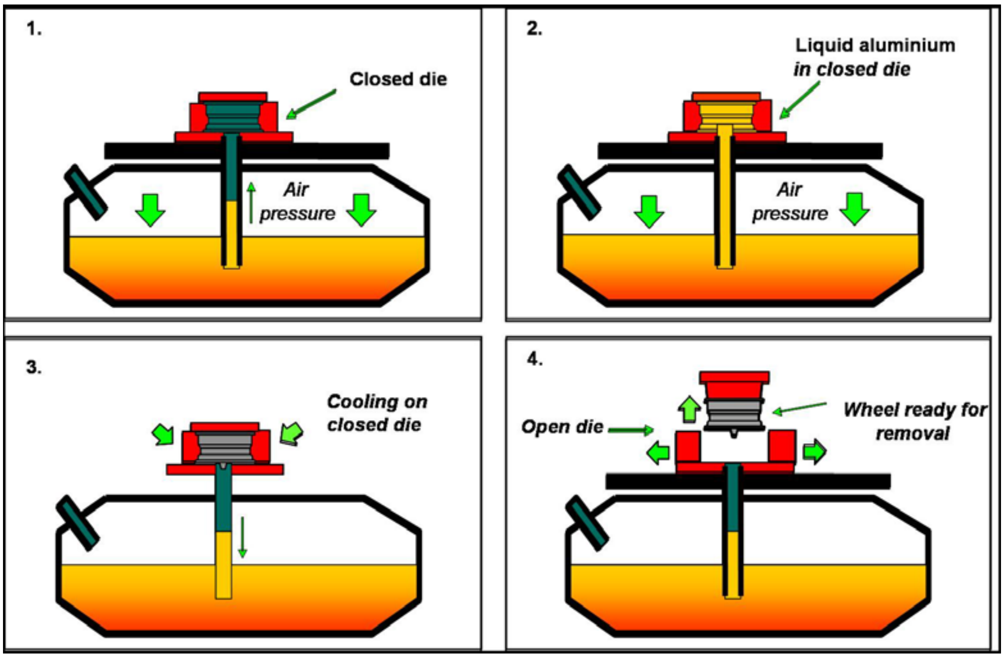

Figure 1-2 A schematic diagram of LPDC.

In the basic configuration of LPDC process (shown in Figure 1-2), large volume of molten metal (ranging from 800 Kg to 1.5 tonne) is delivered into a pressure tight furnace, referred to as a holding furnace. A platform with a mould cavity is located on top of the holding furnace and it is connected by a riser tube. As air in the holding furnace is pneumatically pressurised, molten metal starts to flow into the mould cavity through a riser tube against the gravity.

The key objectives of filling process control in LPDC process, step 1 in Figure 1-2, are to minimise the level of turbulence during the cavity filling and ensure a complete filling of the cavity. Increased level of turbulence during the filling has shown to create entrapped air bubbles and oxide inclusions in the casting components. As a result, reduction of fatigue life and mechanical strength of casting components are commonly observed. While, it is critical to ensure non turbulent filling by reduced filling speed, it is also critical to avoid excessively slow filling. As molten metal flows over mould cavity surface, heat transfer between molten metal and cavity surface takes place. Consequently, the temperature of molten metal would drop and its fluidity is decreased. In extreme cases, where too slow filling with excessive heat loss from the molten metal, metal temperature would drop below its liquidus point and cease to flow. Therefore, a properly controlled filling process is where a balance is achieved between a minimised turbulence and temperature loss.

As mould cavity is completely filled, a series of cooling circuits at strategic locations in the mould cavity are activated to control the solidification profile. The objective of solidification control is to minimise solidification shrinkage. A typical example of this defect is shown in Figure 1-3. Shrinkage porosity, which is one of the most common casting defects, is particularly detrimental in many structural casting applications. It is a well known fact that a presence of shrinkage porosity, hence a discontinuity in casting structure can severely reduce mechanical strength of casting components. Also in some applications, where pressure tightness is critical (e.g. casting wheels, cylinder heads and manifolds etc.), it is also shown that pressure tightness can be severely reduced by shrinkage porosity. Shrinkage porosity is particularly important in manufacturing of aluminium alloy wheel casting, as it requires both superior mechanical property and pressure tightness. More detailed discussion of shrinkage formation and prevention will be discussed in the following section.

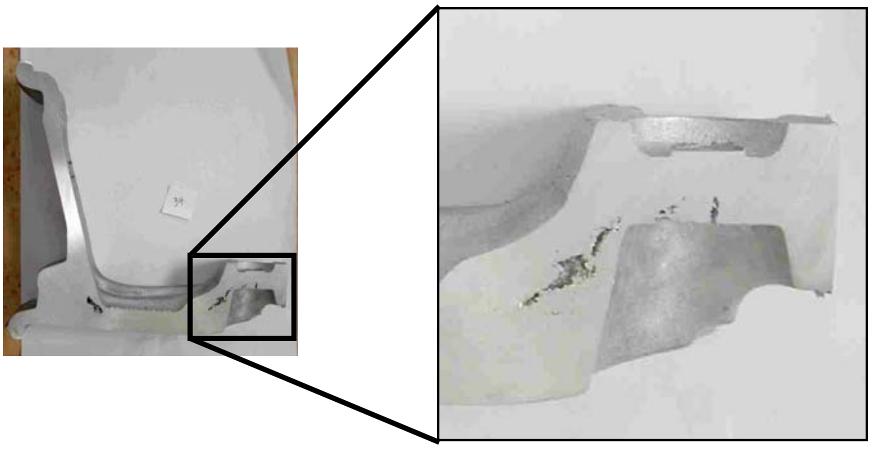

Figure 1-3 Typical shrinkage porosity found in aluminium alloy casting using LPDC.

1.2 Solidification Shrinkage

The root cause of shrinkage porosity is attributed to a basic physical phenomenon of solidification. Typical aluminium alloy experiences 7% volumetric shrinkage during its phase change from liquid to solid due to density discrepancy between those two phases. Voids formed by contraction of casting during solidification need to be compensated by movement of either liquid or solid phase. This compensation of solidification contraction by liquid or solid is commonly known as “feeding”. Failure of efficient feeding or adequate compensation of contraction during solidification would result in discontinuity in casting structure or shrinkage porosity.

1.2.1 Compensation of Solidification Shrinkage

Efficient feeding in casting component can be achieved by a controlled solidification pattern, known as unidirectional solidification. Unidirectional solidification describes a solidification order, where casting part furthest from the riser (reservoir of liquid metal for feeding) solidifies first followed by its adjacent part towards the riser. An example of an ideal unidirectional solidification profile is shown in Figure 1-4. Local solidification time of each location within the casting, labelled A, B and C, shows that the thinnest part, labelled 'A', solidifies first followed by 'B'. Relatively longer solidification time of section 'B' than that of section 'A' means that it remains in liquid phase while the section 'A' goes through solidification. Therefore, any solidification shrinkage in the section 'A' can be compensated by feeding from the section 'C', which is a riser in this case, through the section 'B'.

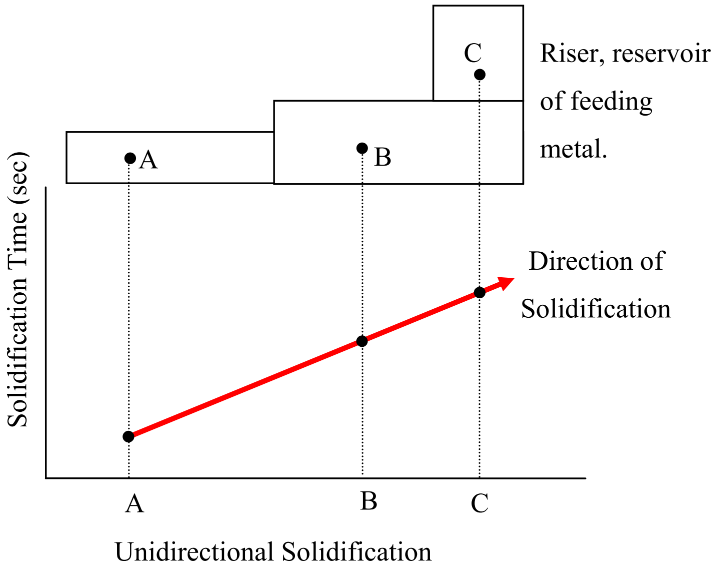

Figure 1-4 Illustration of ideal unidirectional solidification in a simple shaped casting.

In case of non unidirectional solidification, illustrated in Figure 1-5, the local solidification time of section 'A' is longer than the section 'B'. Therefore, section 'B' would solidify before solidification of the section 'A' is completed. Consequently, any feeding from the riser, section 'C', would be impeded as its feeding channel (the section 'B') is solidified. As a result, any solidification shrinkage in section 'A' remains unfed or uncompensated.

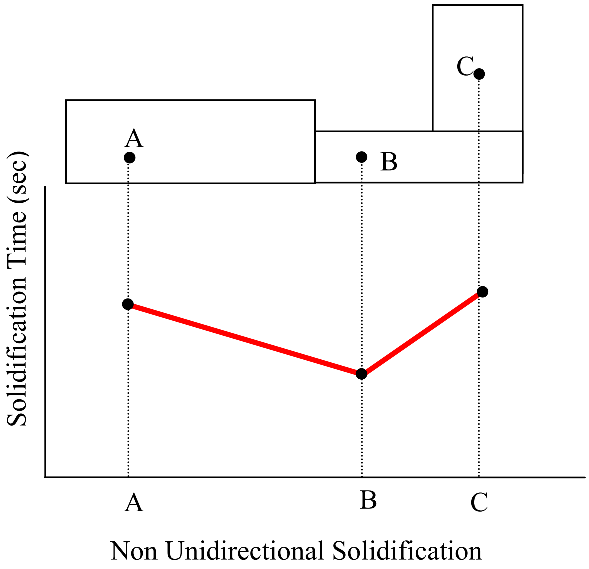

Figure 1-5 Illustration of undesired non-unidirectional solidification in a simple shaped casting.

Therefore in the case of wheel casting, as shown in Figure 1-6, it is desired that the rim part of wheel solidifies first while spoke section can provide feeding. Then it is followed by solidification of spoke section, while hub section would provide feeding and so on. A cross section of a typical wheel casting and a schematic of directional solidification are shown in Figure 1-6.

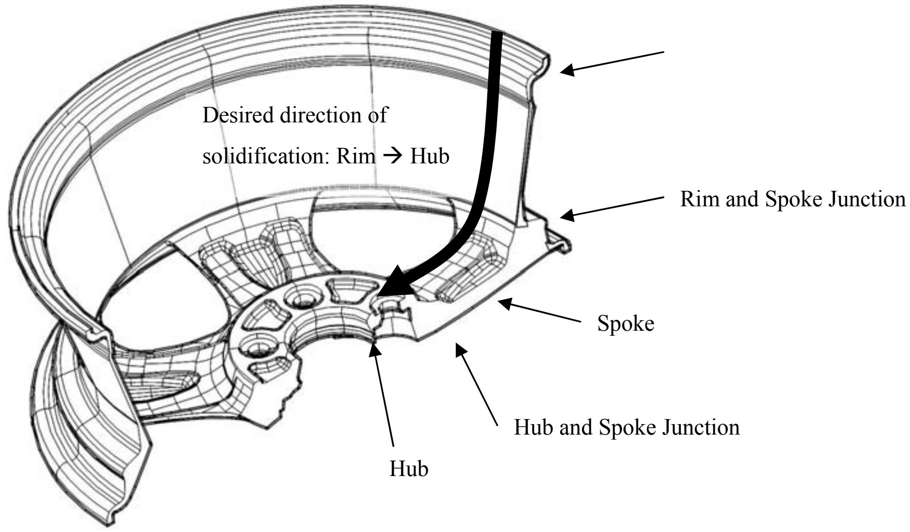

Figure 1-6 A schematic of diagram of desired directional solidification in wheel casting.

In the design process of casting components, it is most logical to design a casting that its geometry can naturally induce the directional solidification. A simple example would a wedge shape casting, where thin edge would naturally cool down and solidify much quicker than the thicker bottom part. However, in the design process of wheel castings and other complex shape castings, it is often that geometry of product is constrained by various other factors, such as design requirement by customers and styling of products. Therefore, it is necessary to design a comprehensive thermal control to achieve a directional solidification even with a complex geometry.

1.2.2 Control of Solidification Shrinkage at ION

Design of a thermal control system at ION mainly involves a series of cooling circuits placed at various locations within the mould cavity. An example of a typical mould cavity for a casting wheel is shown in Figure 1-7, showing both forced air and water cooling circuits. A combination of cooling circuit duration, activation sequence and cooling media flow rate is used as main control parameters. In order for cooling circuit to be effective, a right balance of above control parameters should be achieved.

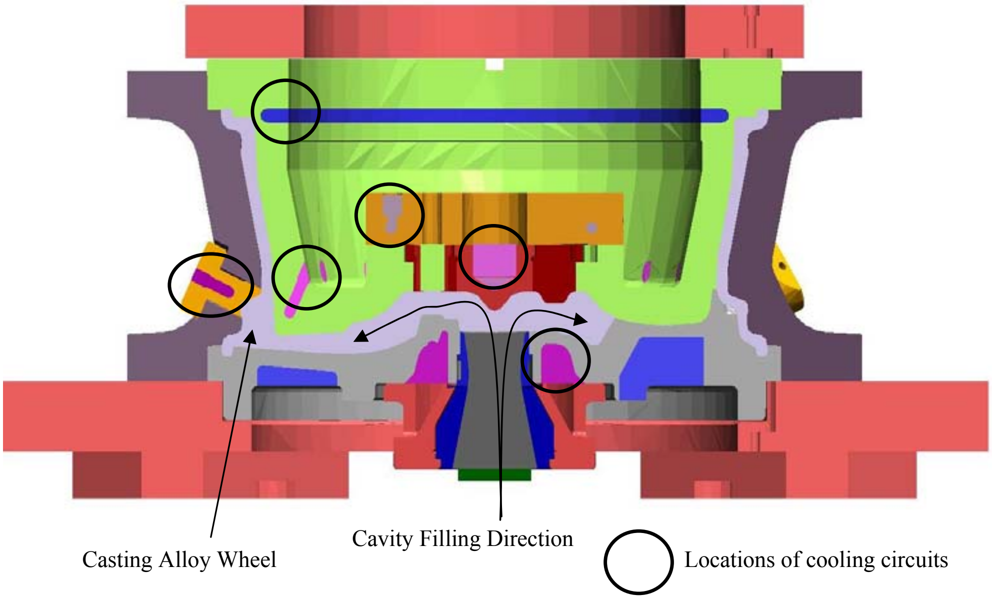

Figure 1-7 An example of thermal control system designed at ION.

Rim and spoke junction (RSJ) of a casting wheel, which is the focus of this study, is considered in Figure 1-8 to illustrate the significance of balanced control parameters. RSJ is selected for this study as it is prone to shrinkage porosity in the junction area. This is mainly due to its geometry where relatively large mass at the junction is surrounded by very thin sections, which are rim and spoke part of the wheel. In RSJ, desired direction of solidification is in the order of rim, junction then spoke section. In Figure 1-9, desired direction of solidification is represented in terms of relative solidification time at each location (rim, junction and spoke). This shows that solidification time of junction is longer than the rim section; hence solidification shrinkage of the rim can be compensated by the junction. Later on, solidification shrinkage of the junction can be compensated by the spoke section, as it shows longer solidification time than the junction. However, naturally increased solidification time of the junction due to its large geometry would alter the solidification order. The effect of increased solidification time is illustrated in a red dotted line in Figure 1-9. Therefore it is necessary to reduce the solidification time of certain area using a forced cooling in order to achieve the desired direction of solidification. In the current thermal control system at RSJ, a water cooled cooling circuit, referred to as chill is located directly targeting the mass of junction area. Intended effect of this forced cooling circuit is illustrated in Figure 1-9 to achieve the desired directional solidification.

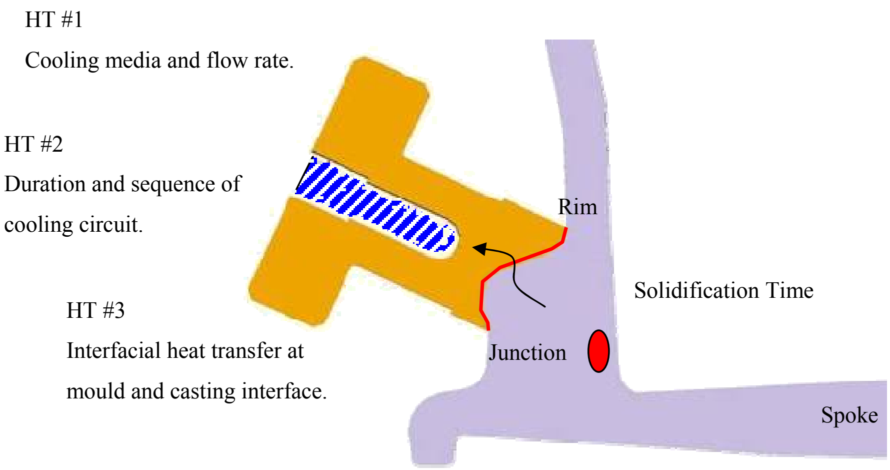

Figure 1-8 Thermal control system at rim and spoke junction (RSJ).

There are three parameters of a forced cooling circuit that determine its effectiveness in controlling solidification pattern of casting. They are shown in Figure 1-8, labelled HT #1, #2 and #3. Heat transfer through cooling circuit and its interface with casting is governed by theses three elements and local solidification is then controlled. Details of these elements are as follows.

- Control of heat transfer through control of cooling medium, HT #1 in Figure 1-8. Air and water are two most commonly used cooling medium and their flow rates and temperatures are considered as critical control parameters.
- Timing of cooling control, HT #2 in Figure 1-8. In the case of time based cooling circuit control, duration of each cooling circuit is considered.
- Control of heat transfer through cooling circuit and casting interface, HT #3 in Figure 1-8. Heat transfer through cooling circuit and casting surface and formation of casting microstructure is considered.

Influence of the above elements in heat transfer through cooling circuit and solidification behaviour will be discussed in more detail in the proceeding section.

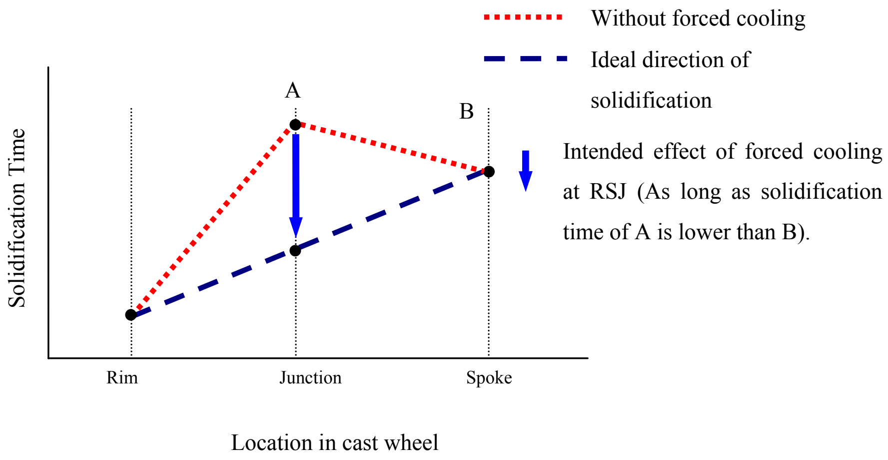

Figure 1-9 Graphical representation of different direction solidification scenario at RSJ.

1.3 Chapter Summary

A brief introduction to the manufacturing process of an aluminium wheel casting at ION Automotive, New Zealand was presented. In more detailed discussion of casting process, solidification shrinkage was identified as the most common yet detrimental casting defect.

It was shown that directional solidification is a key to minimise shrinkage porosity through an effective feeding. However, in many cases of complex shape castings, aluminium casting wheels in particular, casting geometry is not in favour of a naturally induced directional solidification. Therefore, a series of forced cooling regime is implemented in design of casting process and tooling to effectively control local solidification behaviour. Rim and spoke junction of the wheel casting was presented as the main subject of this research due to its tendency to suffer from solidification shrinkage. Detailed discussion of thermal control at the rim spoke junction to minimise the solidification shrinkage has shown the following three key aspects in terms of its effectiveness to control solidification shrinkage.

- Control of heat transfer through control of **cooling medium**, HT #1 in Figure 1-8.
- **Timing of cooling control**, HT #2 in Figure 1-8.
- Control of **heat transfer through cooling circuit and casting interface**, HT #3 in Figure 1-8.

1.4 Research Scope and Objectives

The main objective of this research is to understand the effect of the above key elements of controlling forced cooling on solidification behaviour of aluminium wheel casting to reduce the shrinkage porosity. Detailed objectives are as follows.

1. To conduct a set of controlled experiments to produce casting samples with different levels of thermal control (i.e. cooling) at the chill and metal interface.
2. To perform a series of qualitative x-ray micrograph analysis of casting samples from Objective 1. This is to qualitatively analyse the effect of different thermal control levels on solidification defects.
3. To perform a microstructural analysis of samples form Objective 1 to quantify the effect of different levels of thermal control on overall solidification patterns.
4. Numerical modelling of heat transfer at the chill metal interface and solidification pattern of a casting.
5. Validation of numerical modelling with quantitative microstructural analysis results.

2 Literature Review

The aims of the literature review in this section are as follows.

1. To understand the importance of directional solidification in order to minimise the formation solidification shrinkage.
2. To understand the heat transfer of the casting system, particularly at the casting and cooling circuit interface.
3. To understand the effect of three thermal control factors, as shown in Figure 1-8, on heat transfer of the casting system.
4. To identify the knowledge gap in which one of three thermal control factors requires deeper understanding to improve the effectiveness of the thermal control system.
5. To understand the relationship between thermal condition of casting and its microstructure.

2.1 Directional Solidification

It is clearly understood in the previous chapter that minimised solidification shrinkage is required to ensure high quality structural casting. The rim spoke junction of an automotive wheel, as shown in Figure 1-8, was presented as an example and a main subject of this research. In minimising solidification shrinkage, it was suggested that an effective feeding through unidirectional solidification was necessary.

It was also illustrated in the previous chapter that unidirectional solidification is represented in terms of local solidification or thermal gradient at various locations within a casting, as shown in Figure 1-4. Use of local solidification time or thermal gradient has been extensively used by foundry engineers to gauge or visualise directional solidification, hence sound casting. It is observed that a particular area of casting surrounded by solidification time contours, namely an isolated hot spot, is prone to solidification shrinkage. This observation led to numerous empirical design rules in casting developed by foundry engineers to avoid this isolated hot spot. [2]

One of the pioneering work by Niyama [3] successfully demonstrated theoretical modelling of shrinkage formation during solidification in this regard. It looked at formation of shrinkage in relation to restriction of interdendritic fluid flow due to development of dendritic solidification structure. Niyama's work looked at local thermal gradient and cooling rate at various locations of casting to establish a criteria function of solidification shrinkage, known as Niyama's Function. Niyama's work not only provided the theoretical significance of thermal gradient in solidification shrinkage formation, but also established a subjective measure of shrinkage formation. In this work, Niyama also confirmed foundry engineers' observation of isolated hot spots and its tendency to form solidification shrinkage.

Further development in research of criteria functions saw a series of modified Niyama's functions to aluminium alloy applications, where Niyama's function was originally based on steel alloys [4 - 11]. Review of those modified criteria functions shows that criteria function based thermal gradient is applicable in aluminium alloy castings, provided that correction factors are added to account the effect of dissolved hydrogen gas on shrinkage formation. This further highlights the theoretical significance of thermal gradient or unidirectional solidification in minimising solidification shrinkage.

2.2 Heat Transfer at Cooling System Casting System

It is shown in the previous chapter that various cooling circuits are placed in a typical casting die of aluminium alloy wheels. It is also illustrated that these cooling circuits at strategic locations play a critical role in improving casting quality by allowing better direction of solidification

In thermal control of a typical low pressure permanent mould casting process, there are three major methods [2].

- Increased surface area of outside of die cavity area to dissipate more heat through natural convection (e.g. cooling fins).
- Increased die mass in certain areas to absorb more heat from the cavity (e.g. heat sinks) or controlled thickness of mould coating.
- Forced cooling using water or air through cooling channels (forced convection).

Over the years, it is experienced by casting process engineers that forced cooling is the most efficient and the fastest approach to control the thermal profile of casting cavity. Likewise at ION, the major thermal control method is through forced cooling method. Therefore, the remaining of literature review looks at physical description of forced cooling and known effects of some of its critical parameters.

The following section looks at mathematical and physical significance of forced cooling circuit, which is referred to as HT#1 and HT#2 in Figure 1-8.

2.2.1 Mathematical Approximation of Cooling Circuits

A specific case of forced cooling is considered, namely forced cooling in a tube or an enclosure. In a typical cooling circuit arrangement, a cooling channel is drilled in a steel die block. A uniform heat flux is assumed from all direction of cooling channel, as shown in Figure 2-1. Additionally idealised distribution both temperature and velocity of cooling fluid in y direction is assumed, as illustrated in Figure 2-2.

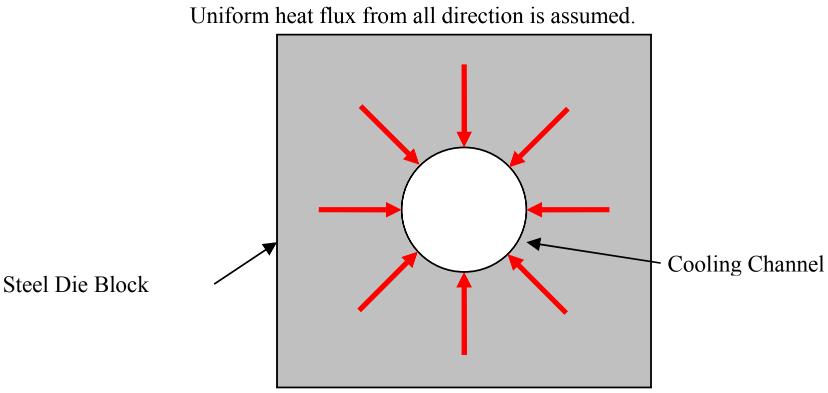

Figure 2-1 A schematic diagram of heat flux around a cooling channel in a steel die.

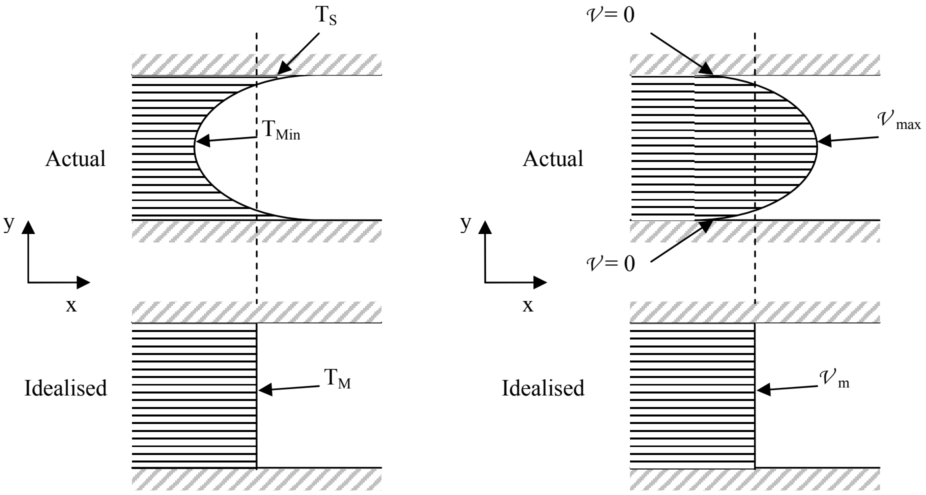

Figure 2-2 Illustrations of idealised distribution of temperature and velocity in cooling channels.

Furthermore, the following assumptions are made.

- Conservation of mass – no loss or gain of mass between inlet and outlet of cooling channel.
- No work done on the fluid – no work interactions on fluid.
- No friction between fluid and tube layer.
- Constant C_P for the flow media is assumed.

Therefore convection heat transfer at any location within the cooling channel can be expressed by the following equation.

$$Q = hA\Delta T = hA(T_S - T_m)$$

Equation 2-1

Where

h = Convection heat transfer coefficient

A = Surface area of cooling channel

T_S = Surface temperature of cooling channel

T_m = Idealised mean temperature of cooling fluid

A schematic diagram of energy balance of flow through a tube section is shown in Figure 2-3.

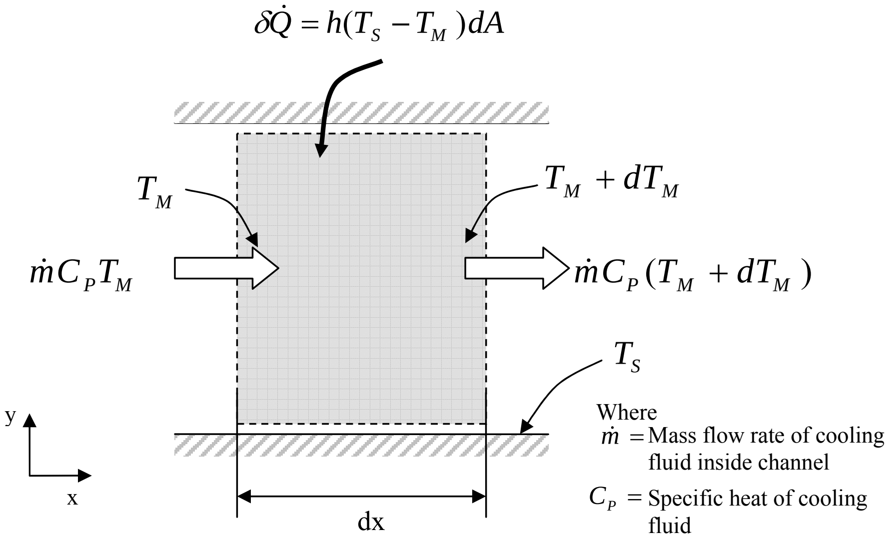

Figure 2-3 A simple energy balance diagram of flow through a channel.

With an assumption of no work done on the fluid and no friction at the boundary, the above energy balance relationship shown in Figure 2-3 gives the following.

$$\dot{m}C_P dT_m = h(T_S - T_m)dA$$

Equation 2-2

With aforementioned assumptions of constant C_P for cooling fluid and conservation of mass through the channel, it is shown in Equation 2-2 that a change in temperature of cooling fluid is solely governed by heat transfer between the surface of the cooling channel and cooling fluid. The convection heat transfer coefficient, shown as h in Equation 2-2, plays a key role in this equation as a mathematical representation of heat transfer between cooling channel surface and cooling fluid under various conditions.

In an effort of determining h values in various conditions of cooling channel, empirical method is typically used. This is primarily due to the complex nature of heat transfer phenomena, which is affected by other complicated factors such as presence of turbulent flow, degree of friction at the cooling channel surface and geometry of cooling channel. When heat transfer in a cooling channel of simple of geometry or simplified geometry is considered, first laminar or turbulent nature of fluid flow is determined by calculation of Reynolds Number, Re. Reynolds Number is a non-dimensional quantity, which is a ratio of the inertia forces to the viscous forces of the fluid, as shown in Equation 2-3. It is known that fluid becomes a turbulent nature when it exceeds the critical Reynolds Number, which varies depending on geometry. The critical Reynolds Number for a tube is known to be 2300, where a transition between full laminar to turbulent flow begins and by 4000 it is considered a fully developed turbulent flow. [12]

$$\mathrm{Re} = \frac{\text{Inertia Forces}}{\text{Viscous Forces}} = \frac{\mathrm{v}_\infty \delta}{\nu}$$

Equation 2-3

where

v_∞ = free-stream velocity, (m/s).

δ = characteristic length of the geometry, (m).

v = kinematic viscosity, (m^2/s).

Subsequently, another non-dimensional quantity, named Nusselt Number, Nu, is introduced. Nusselt Number expresses the ratio of the convection heat transfer and conduction heat transfer, as shown Equation 2-4 and Figure 2-4.

$$Nu = \frac{\dot{q}_{conv}}{\dot{q}_{cond}} = \frac{h\delta}{k}$$

Equation 2-4

where

$\dot{q}_{conv} = h\Delta T$

$\dot{q}_{cond} = k\dfrac{\Delta T}{\delta}$

k = thermal conductivity of fluid, (w/m).

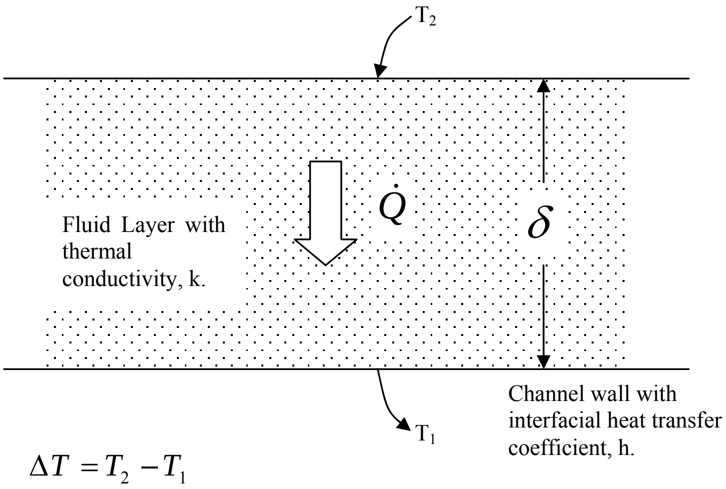

Figure 2-4 Illustration of heat transfer through a small layer of fluid.

Therefore, Nu = 1 indicates that heat transfer shown in Figure 2-4 is a conduction through fluid layer and greater the Nusselt Number larger the heat transfer by convection. Nusselt Number is significant in determining the convection heat transfer coefficient h as it has the following empirical relationship with previously discussed Reynolds Number for both laminar and turbulent flow. [12]

$$Nu = 1.86\left(\frac{\mathrm{Re}\,\mathrm{Pr}\,D}{L}\right)^{1/3}\left(\frac{\mu_b}{\mu_s}\right)^{0.14} \qquad \text{(Laminar flow)}$$

$$Nu = 0.023\,\mathrm{Re}^{0.8}\,\mathrm{Pr}^{1/3} \text{ (Turbulent flow)}$$

Equation 2-5

where

μ_b = bulk mean temperature of fluid.

μ_s = surface temperature of cooling channel.

D = diameter of tube.

L = length of tube.

Pr = Prandtl number, the dimensionless parameter for the thermal boundary layer.

f = friction factor for turbulent flow.

Substituting Equation 2-5 into Equation 2-4 yields the following relationship between empirically determined properties, Re and Pr, and convection heat transfer, as shown below.

$$\frac{h\delta}{k} = 1.86\left(\frac{\mathrm{Re}\,\mathrm{Pr}\,D}{L}\right)^{1/3}\left(\frac{\mu_b}{\mu_s}\right)^{0.14} \qquad \text{(Laminar flow)}$$

$$\frac{h\delta}{k} = 0.023\,\mathrm{Re}^{0.8}\,\mathrm{Pr}^{1/3} \qquad \text{(Turbulent flow)}$$

Equation 2-6

Despite its simple appearance of Equation 2-6, determining correct value of heat transfer coefficient can be extremely difficult in many cases. The difficult is more apparent when more complicated shapes of cooling channel are considered rather than simplified shapes, where the most of empirical effort was focused on. Correct evaluation of Re and Pr alone in a complex shaped flow channel involving turbulent flow can be a complicated fluid dynamic problem. Therefore in many cases, where simply convection heat transfer coefficient value is required for the purpose of further numerical analysis, a method known as inverse engineering approach is used in conjunction with some experimental data. Through this method, approximated value of convection heat transfer coefficient can be determined. A schematic diagram of inverse engineering approach is shown in Figure 2-5.

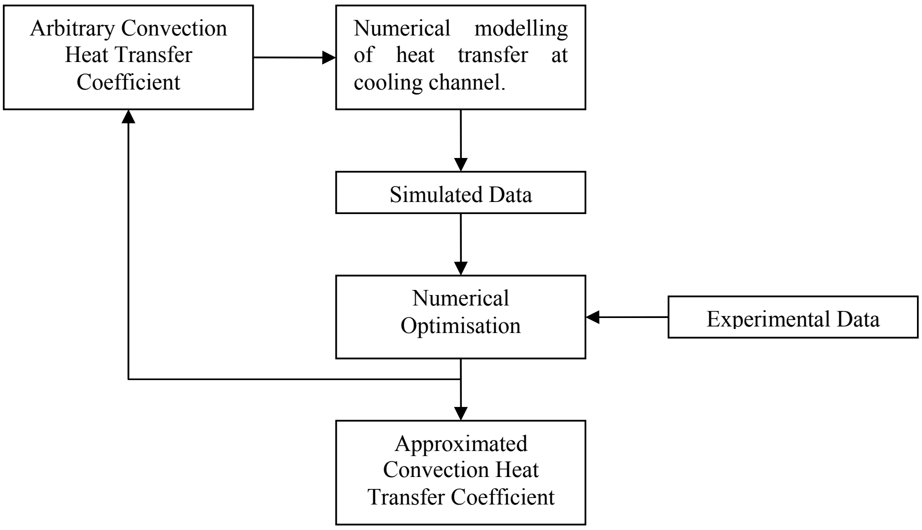

Figure 2-5 Inverse engineering approach to empirically determine interfacial heat transfer coefficient, h.

In this method, an arbitrary value of heat transfer coefficient is initially assumed. It is then used in a numerical modelling of heat transfer, where the output is compared against the experimental data using a numerical optimisation approach. Several literature looks at different numerical optimisation techniques to determine heat transfer coefficient based in iterative on approach [13, 14, 15, 16, 17]. However, the detail of various numerical optimisation methods will not be discussed in this literature review as it is out of scope for the current research work.

2.2.2 Effect of Cooling Media on Heat Transfer

In order to understand the effect of different cooling parameters on convection heat transfer coefficient at the cooling circuit, several researchers looked at determining convection heat transfer coefficient with different experimental condition. (using aforementioned numerical optimisation methods). Namely cooling media flow rate and temperature.

Booth and Allsop [18], demonstrated that water flow rate is only significantly influential on heat transfer coefficient for a very small range. It shows that only at very low flow rate the heat transfer differs significantly. It is due to possible boiling of water at very low flow rate and leading to erratic behaviour in heat transfer. Once the flow rate reaches a certain level, the flow rate shows very little effect. Very similar result is also reported by Manilal *et. al.* [19]. In this research, it is highlighted that in case of water cooling, water temperature is more influential than actual flow rate.

Manilal *et. al.* [19] however, reported that flow rate becomes more influential on convection heat transfer when air is used as main cooling fluid. Using experimental data and numerical optimisation, it is demonstrated that there is a linear relationship between convection heat transfer coefficient and a range of flow of rate. However, it was noted that over certain flow rate, there is a little increase in heat transfer coefficient with increase in flow rate.

2.3 Heat Transfer at Mould and Casting Interface

In this section, the fundamental study of heat transfer at the mould and casting interface is reviewed. Firstly, heat transfer in its physical significance is discussed and its mathematical approximation is followed. Lastly, a discussion on a series of previously published literature on the effect of some casting process parameters on overall heat transfer mechanism is discussed.

Physical Mechanism of Heat Transfer at Casting Mould Interface

At the interface of casting and mould, there are number of heat transfer mechanisms that are considered. Firstly, in order to better understand the nature of heat transfer mechanism at the interface, physical nature of the interface at microscopic level is analysed.

A schematic diagram of the casting mould interface at microscopic level is shown in Figure 2-6. Regardless of how smooth the mould surface might appear, at microscopic level there are varying ranges of surface irregularity. Due to this surface irregularity, the heat transfer mechanism at the metal mould interface is considered as a combination of different heat transfer mechanisms with varying level of dominance rather than one single dominating mechanism. However, it is a general consensus in literature that the following heat transfer mechanisms are the predominant and most significant. [20]

Comment [RL1]: This sentence is too long.

- Conduction through point to point contact (liquid to solid or solid to solid).
- Conduction through air gap.
- Radiation from metal surface through air gap.

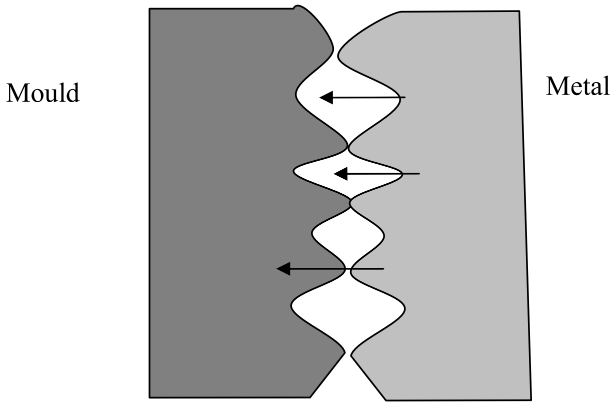

Figure 2-6 A schematic diagram of casting mould interface at microscopic level.

Conduction through a point to point contact

When the liquid metal fills the cavity during the filling, the liquid part comes in contact with peaks of irregular surfaces of mould. As liquid metal comes in contact with peaks of mould surface, nucleation of solid metal takes place and initial solid to solid contact is established. This mechanism of solid to solid contact during the initial filling and early stage of solidification was initially proposed by Prates and Biloni [21]. It was based on the postulation that surface peaks at a microscopic level would provide nucleation sites for solidification and become points of contact for conduction. Later study by Ho and Pehlke [20] confirmed this postulation. Ho and Pehlke showed experimental data of increased heat transfer in early stage of filling and solidification in their study. Through, inverse and numerical modelling methods, Ho and Pehlke proved this postulation by Prates and Biloni.

Conduction and radiation through air gap

Another important aspect of postulation on heat transfer mechanism due to surface peaks proposed by Prates and Biloni [21] was a suggestion of an air gap formation at the interface of mould and metal. A combination of restricted wetting ability of liquid metal due to surface tension and contraction of liquid metal during its initial solidification was suggested as a main mechanism of air gap formation in between valleys of surface peaks.

Advancing from this postulation, Ho and Pehlke [20] suggested further refined models to explain heat transfer mechanisms in the later stage of solidification. Three most probable mechanisms were proposed, namely convection in the air gap, conduction and radiation through air gap. However, a simple calculation of Grashof number for such a thin layer of air gap indicates that convection in this case is negligible. Therefore the main mechanism of heat transfer in the air gap at the interface is focused on a combination of conduction and radiation through air gap.

In their early study, Ho and Pehlke [20] used a simple superposition of both radiation and conduction through air gap to model heat transfer at the interface with a reasonable accuracy. In their later study [22,23], use of inverse modelling based on convection and radiation mechanism successfully modelled the heat transfer at the interface with an improved accuracy. In the same study [23], heat transfer at the interface was modelled using the quasi steady state approximation by summing the effect of conduction and radiation through a measured thickness of air gap. The study showed that there was a close agreement between the initial inverse modelling result and later quasi steady state approximation of conduction and radiation. This confirms that the proposed model of heat transfer at the interface is a combination of conduction and radiation through air gap.

2.3.1 Mathematical Approximation of Heat Transfer at Interface

Heat transfer at the interface can be expressed as a sum of three mechanisms discussed in the previous section as shown below.

$$\dot{Q} = \dot{Q}_S + \dot{Q}_G + \dot{Q}_R$$

Equation 2-7

where

$\dot{Q}_S$ = Heat transfer by conduction through solid contact.

$\dot{Q}_G$ = Heat transfer by conduction through air gap.

$\dot{Q}_R$ = Heat transfer by radiation through air gap.

In order to simplify the expression, the above equation can be expressed in analogous manner using Newton's law of cooling. [12]

$$\dot{Q} = h_c A \Delta T_{Interface}$$

Equation 2-8

where

A = Contact area at the interface.

$\Delta T_{Interface}$ = Effective temperature difference at the interface.

h_c = Convective heat transfer coefficient.

h_c in most of heat transfer problem is referred to as convective heat transfer coefficient. However, in this specific case of interfacial heat transfer problem, it is otherwise referred to as thermal contact conductance or interfacial heat transfer coefficient. h_c in this case is a sum of the following.

$$h_c = h_S + h_G + h_R$$

Equation 2-9

Again, subscript S, G and R refers to three main mechanisms of interfacial heat transfer, conduction through solid contact (h_S), conduction (h_G) and radiation (h_R) through air gap respectively.

$h_S \propto k_m / c(P/H)^{\frac{1}{2}}$ Rapier *et. al.* [24]

$h_G = k_G / x_G$

$$h_R = \varepsilon\sigma(T_1^2 + T_2^2)(T_1 + T_2)$$

Referring back to Newton’s Law of Cooling, heat transfer at the interface can be expressed in the following, Equation 2-10. It is also graphically illustrated in Figure 2-7.

$$Q = (h_S + h_R + h_G)A(T_1 - T_2)$$

Equation 2-10

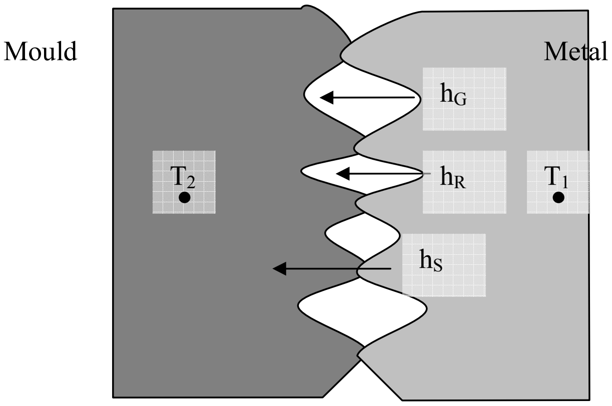

$$Q = (h_S + h_R + h_G)A(T_1 - T_2)$$

Figure 2-7 A schematic diagram of heat transfer at the mould and metal interface showing a combination conduction, convection and radiation through air gap.

In the interest of determining interfacial heat transfer coefficient for various casting applications, establishing individual heat transfer coefficient (h_S, h_R and h_G) can be very complicated. Therefore, above three heat transfer coefficients are further simplified into a single term, interfacial heat transfer coefficient (h_C). Another important aspect of simplification is that rather than irregular surface contact between the mould and casting, as shown in Figure 2-7, perfect surface contact is assumed. A schematic of this simplification is shown in Figure 2-8.

.

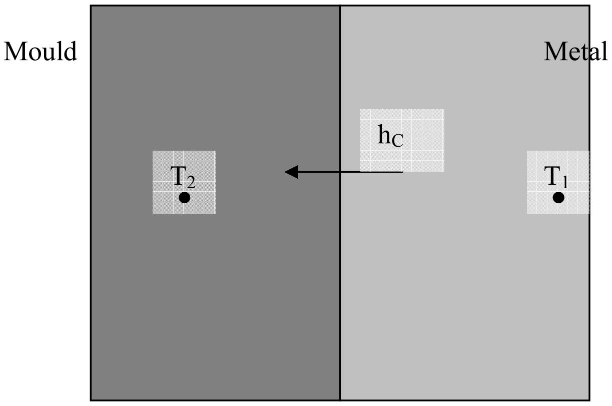

$$Q = h_C A(T_1 - T_2)$$

Figure 2-8 Illustration of simplification of heat transfer at the casting mould interface using interfacial heat transfer, h_C.

Interfacial heat transfer coefficient, h_C, is then empirically determined by measuring temperature gradient across the casting and mould interface. There are several methods of inverse optimisation to establish the interfacial heat transfer coefficient as a function of time or temperature. Details of inverse optimisation technique will not be discussed in detail as it is not the main scope of this research. However, a discussion of literature on determining interfacial heat transfer with varying casting conditions and their effects will be presented in the following section.

2.3.2 Effects of Casting Variables on Interfacial Heat Transfer

Casting super heat and mould temperature

Two most influential thermal parameters in casting process are initial mould temperature and superheat of metal entering the mould cavity. Superheat is defined as excessive temperature above the liquidus temperature of casting alloy.

A comprehensive research by Muojekwu et. al [25] looked at effect of varying superheat, ranging from 0°C to 120°C , on interfacial heat transfer coefficient between Al-Si alloy and a copper chill. The maximum value and overall profile of interfacial heat transfer comparison shows that increased superheat produced higher interfacial heat transfer coefficient in both maximum value and overall profile. Similar results are reported by Gafur *et. al.* [26], where superheat raging from 45°C to 140°C applied and interfacial heat transfer coefficient between pure Al and a copper chill was determined.

It is suggested by Muojekwu *et. al.* [25] that this increase in interfacial heat transfer coefficient with increased superheat is due to increased fluidity of molten metal improving the surface contact. This surface contact in this regard refers to h_S in Equation 2-10. Again similar explanation is presented by Gafur *et. al.* [26]. Evidence of this theory is also shown by Michel *et.al.* [27], where increased mould temperature produced increased interfacial heat transfer coefficient. It is understood that increased mould temperature means that the molten metal in the cavity can retain its superheat longer, hence improved the surface contact and h_S .

Chill materials

Muojekwu et. al [25] in their research also looked at four different chill materials (copper, brass, steel and cast iron) and their respective effects on interfacial heat transfer coefficient. The results clearly showed that increased thermal diffusivity of chill material increased both maximum value and overall interfacial heat transfer coefficient. This result is also supported by other researchers [28, 29], where copper chills show higher interfacial heat transfer coefficient than steel chills.

An important point by Muojekwu et. al [25] is that interfacial heat transfer towards the later stage of solidification shows very little difference between different chill materials. The authors suggested that this is an indication of air gap development at the chill and casting interface. Presence of air gap suggests that conduction through an air gap (h_G in Equation 2-10) becomes a more dominant factor in determining heat transfer from casting to chill. Consequently, thermal diffusivity of different chill materials becomes less dominant. Similar results are observed other reported studies. [28, 29,30]

Coating methods

It is a commonly used technique in foundries to apply various types of coating on chill and mould surfaces for the following reasons.

- Protection of chill and mould material from corrosive alloys, such as aluminium alloys.
- Provide insulating characteristics as a mean of thermal control of dies.

In controlling thermal characteristics of surface coatings, its insulating capacity is increased by either increased coating thickness or increased surface roughness. In research work by Chiesa [31], insulating coating materials with varying conditions were applied and their insulating capacities were measured by interfacial heat transfer coefficient. Chiesa reported that increased coating thickness provided much less increase in insulating capacity when compared to increased surface roughness. This indicates that conduction through air gap, shown as h_G, is much more dominant factor determining heat transfer across the mould and casting interface than conduction through solid contact

h_S . Similar results are reported elsewhere, indicating that conduction through solid contact being much less influential that conduction through air [25, 27].

Number of literature reported the presence of additional pressure during solidification [32, 33] increases interfacial heat transfer coefficient. It is a general consensus among these authors that the presence of additional pressure due to either by contraction pressure or applied pressure increases solid to solid contact between mould and casting. Therefore it increases h_G in Equation 2-10.

2.4 Microstructure of Al-Si Alloys

Growth of a typical microstructure is discussed in this section. Understanding of microstructure formation is critical in this research as it is used as a measure of thermal history of casting section. In this section of literature review, brief theory on a typical microstructure formation, namely dendrite structure, and its relationship with thermal parameters are discussed.

2.4.1 Typical Microstructure Development of Al-Si Alloys

After nucleation of solid particles, solute is diffused and constitutional undercooling takes place. Then depending on level of undercooling, different modes of solid growth is determined – planar growth, cellular growth and dendrite growth, as shown in Figure 2-9. In this literature review, only dendritic growth will be considered.

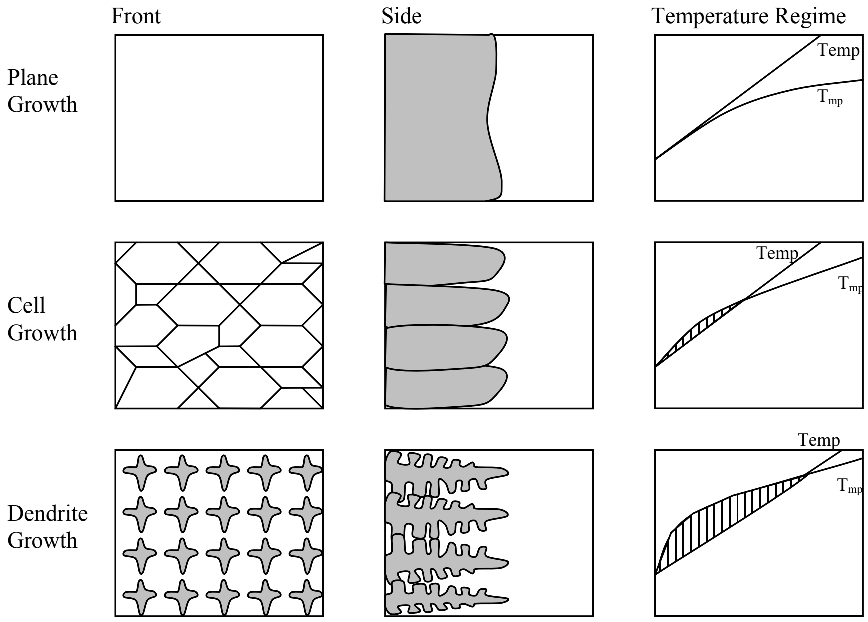

Figure 2-9 Different modes of solid growth, plane growth, cell growth and dendrite growth [34].

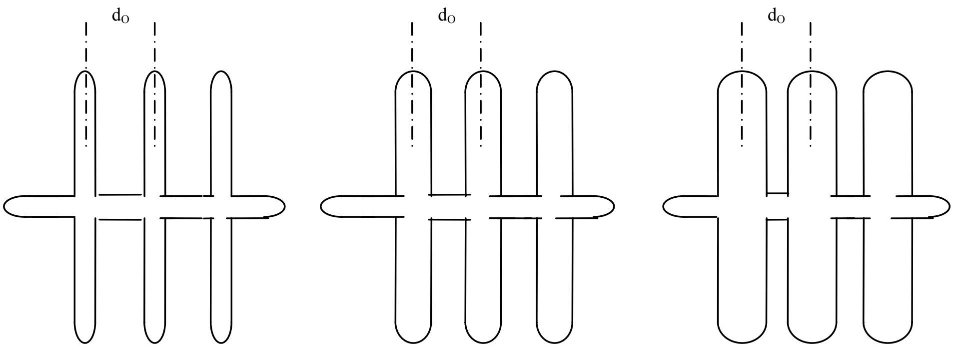

Figure 2-10 Early model of dendrite arm growth by Flemings [35].

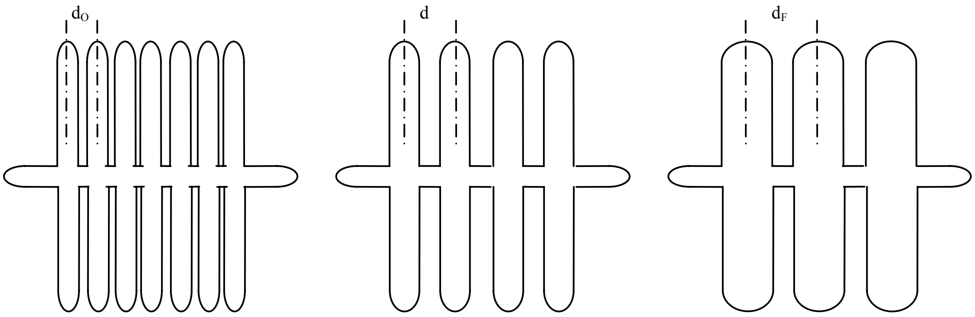

Figure 2-11 Corrected model of dendrite growth by Flemings [36].

The above model of dendrite coarsening was suggested by Flemings [35]. It was originally suggested by Flemings [35] that the initial dendrite arm spacing d_O would remain more less same as the final dendrite arm spacing d_F . It is understood that individual dendrite arms would continue to grow after maintaining its initial dendrite arm spacing, as shown in Figure 2-10. However, Flemings' later work [36] looked at modified model of dendrite arm coarsening. Rather than the original idea of individual arm coarsening while maintaining its original arm spacing, it concluded that there are several dendrite arms initially with much smaller original arm spacing d_O . Then as solute diffusion controlled arm growth continues, one dendrite arm becomes a dominating one while adjacent arms remelt. This continuous remelting of adjacent arms allows the initial dendrite arm spacing to grow. As more arms remelt even larger dendrite arm spacing is produced as shown in Figure 2-11. Additionally, Flemings presented five difference modes of dendrite arm coarsening, illustrating various cases of dendrite arm structure formation as shown in Figure 2-12.

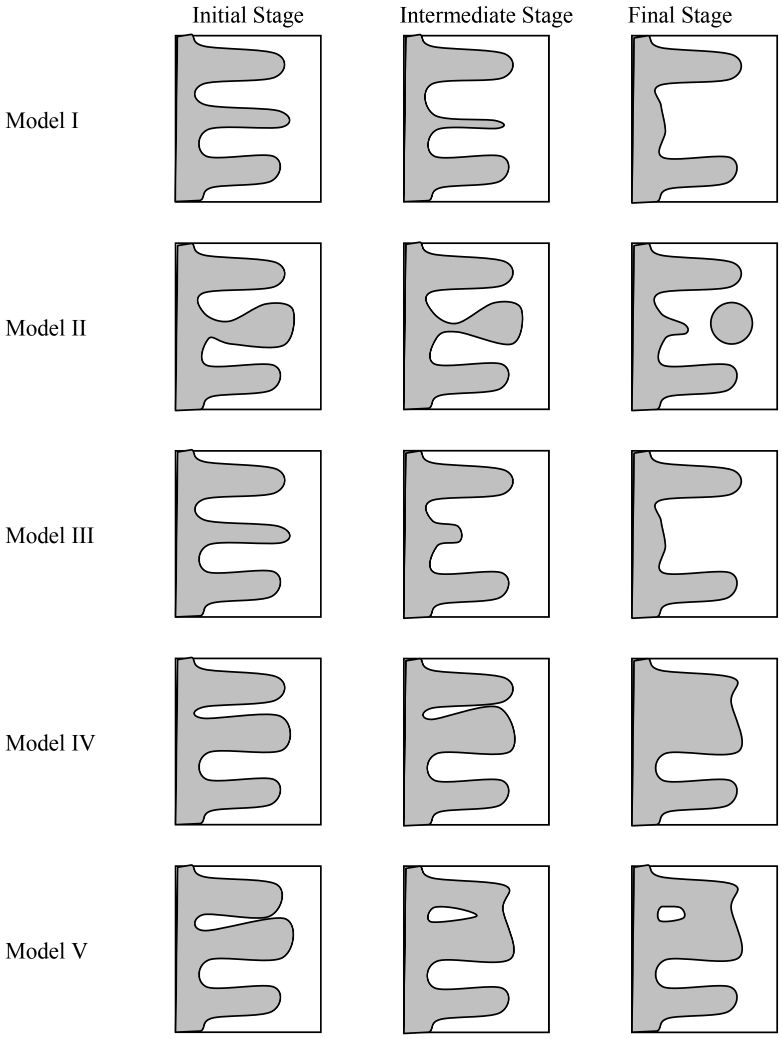

Figure 2-12 Dendrite coarsening model [36].

2.4.2 Microstructure and Thermal Parameters

It was reported by Flemings [35] in 1966 that there is a power law relationship between secondary dendrite arm spacing and thermal parameters. It was validated by using the experimental data of Al-4.5%Cu that secondary dendrite arm spacing and solidification time have a power law relationship. It was suggested that with longer solidification time, hence slower cooing rate, longer period of remelting is allowed for dendrite arms. Therefore much larger individual dendrite arms with larger dendrite arm spacing are produced as a result. Based on diffusion controlled coarsening model, Flemings suggested the following relationship between the solidification time and final dendrite arm spacing, as shown in Equation 2-11.

$$d = A\theta_f^a$$

Equation 2-11

where

$A =$ Alloy specific constant

$\theta_f =$ Local solidification time

$a =$ Alloy specific exponent

Based on Flemings' equation, notable further modification was made by Kirkwood [37] as shown in Equation 2-12. An additional parameter of M, expressed as a coarsening parameter in Equation 2-13.

$$\lambda_2 = K(Mt_F)^{1/3}$$

Equation 2-12

Where

$\lambda_2 =$ Secondary Dendrite Arm Spacing

$K =$ Alloy specific constant

$M =$ Coarsening parameter

$$M(m^3/s) = -\frac{\Gamma D}{(1-k_0)m_L(C_E - C_0)}\ln\left(\frac{C_E}{C_0}\right)$$

Equation 2-13

where

$\Gamma =$ Gibbs-Thomson coefficient

$m_L =$ Liquid line slop in Al alloy phase diagram

$k_0 =$ Solute partition coefficient

$D =$ Liquid solute diffusivity

$C_E =$ Eutectic composition

$C_O =$ Alloy composition

Various researchers have validated the accuracy of Kirkwood model under various casting conditions and different alloys. Peres *et al* [38] reported that the Kirkwood model with a numerical factor of 5 with varying coarsening parameter M for four different Al-Si alloys closely match their experimental values. A list of different coarsening parameters and respective Al-Si alloy is shown in Table 2-1.

Table 2-1 List of different coarsening parameters used for various Al-Si alloys. [38]

Alloys	Coarsening Parameter (M)
Al-3wt%Si	7.73E-18
Al-5wt%Si	6.30E-18
Al-7wt%Si	5.43E-18
Al-9wt%Si	4.883E-18

The above coarsening parameters for formation of dendritic arms relate to a typical cooling curve or Al-Si alloy, shown in Figure 2-13. The part of cooling curve corresponds to formation and coarsening of dendritic arms is labelled reaction ‘1’ and ‘2a+2b’. Detail of those reactions is shown in Table 2-2.

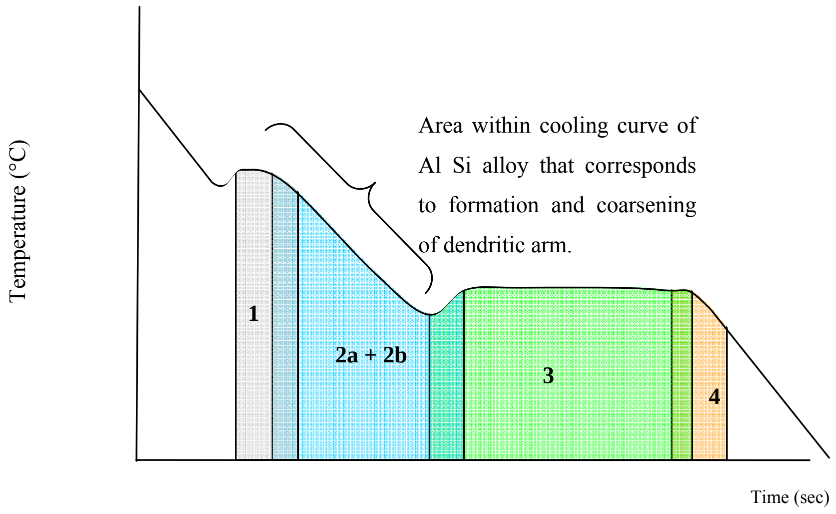

Figure 2-13 A typical cooling curve of Al-Si alloy showing areas where formation and coarsening of dendritic arms take place.

Table 2-2 List of different reactions take place during solidification of Al-Si alloy. [1]

Reaction No.	Reactions	Remarks
1	$Liq. \rightarrow Al$	Formation of dendrite arms.
2a	$Liq. \rightarrow Al + Al_{15}(Mn, Fe)_3 Si_2$	Coarsening of dendrite arms.
2b	$Liq. \rightarrow Al + Al_5 FeSi + Al_{15}(Mn, Fe)_3 Si_2$	Coarsening of dendrite arms.
3	$Liq. \rightarrow Al + Si + Al_5 FeSi$	Formation of Si eutectic.
4	$Liq. \rightarrow Al + Si + Mg_2 Si$	

Contrast to a close match between the Kirkwood model and the experimental data by Peres *et al* [38], experimental data using sand casting samples by González-Rivera *et al* [39] shows a quantitative discrepancy while showing good qualitative agreement between the Kirkwood model and the experimental data. The fact that there is a good qualitative agreement confirms that the basic relationship between secondary dendrite arm spacing and solidification time is roughly proportional to the root of cube, as it was shown elsewhere [40].González-Rivera *et al* stipulated that "*the quantitative discrepancy observed might be related the difference between experimental and predicted local solidification time, to the limitations of the coarsening model implied in Kirkwood model, including the applicability of the selected ripening parameter* (coarsening parameter) *to the case of the experimental alloy or to experimental error associated to the SDAS* (Secondary Densrite Arm Spacing) *measurement method used in this work"*. This highlights the importance of numerical correction factor in Kirkwood model that different thermal conditions and other factors that could affect coarsening of dendrite arms need to be considered.

2.5 Chapter Summary

In the introduction, it is highlighted that presence of directional solidification is required to minimise the solidification shrinkage. It is also shown that thermal control is one of the keys to achieve directional solidification.

In the literature review, number of literature is shown to highlight the theoretical background and importance of directional solidification. Then thermal control, especially focusing on forced cooling, was discussed and the effect of different parameters (cooling media, flow rate and temperature). This refers to HT #1 in Figure 1-8.

Furthermore, a discussion on interfacial heat transfer between casting and mould, which correspond to HT #3 in Figure 1-8, and its physical and mathematical significance was discussed. Also, various casting parameters and their respective effect on interfacial heat transfer coefficient are discussed.

From this, it is concluded that there is not sufficient understanding in cooling circuit timing and its effect on thermal control dies. It is only intuitively guessed longer duration equals more heat removed from dies. Therefore, the main focus of this research is to analyse the cooling circuit duration and its effectiveness in thermal control of casting. In addition, literature review has shown that the measurement secondary dendrite arm spacing can be translated into local cooling rate of casting, which can be an indication of effectiveness thermal controls.

It is therefore proposed that the focus of this research is to determine the effect of cooling circuit timing on overall effectiveness of thermal control. It is also proposed that measurement of secondary dendrite arm spacing would be used as a microstructural indicator of effectiveness of thermal control.

3 Experimental and Analysis Procedures

3.1 Introduction

It was established in the previous chapter that duration of cooling circuit and its effects on thermal control were necessary to further understand the methods of ensuring directional solidification in a rim and spoke junction. Measurement of secondary dendrite arm spacing (SDAS) was presented as one of indirect methods to quantify different thermal history of casting samples. Therefore it was suggested that SDAS measurement can be used to quantify the effectiveness of different cooling duration in ensuring right thermal gradient, hence sound casting quality. The experimental work conducted was aimed towards to produce casting samples with different durations of cooling circuit and analytical methods to quantify its effects on effectiveness of thermal control.

3.2 Casting Experiments

As discussed in the previous section, a series of casting experiments was required to analyse the effect of different durations of cooling circuits on casting quality. Again, rim and spoke junction of a casting wheel, as shown in Figure 1-8, is the main focus of this experiment.

A particular model of casting wheel, referred by its model name D333, is selected for the purpose of casting experiment. A schematic diagram of D333 is shown in Figure 3-1. D333 model is selected as a subject of casting experiment for the following reasons.

- Large number of spokes. Each D333 wheel has fifteen spokes, producing significant number of rim spoke junction samples.
- Relatively simple profile at the rim and spoke junction for ease of microstructural and thermal analysis.

Figure 3-1 An illustration of D333 wheel used in the casting experiments.

A graphical representation of a typical timing based cooling circuit settings are shown in Figure 3-2 and their corresponding locations within tooling design of D333 are shown in Figure 3-3. Each setting consists of the following four components.

- Delay – Start of each cooling circuit is controlled by the delay parameter to ensure that each cooling circuit is activated to produce directional solidification.
- Air – For cooling circuit with air as main cooling media duration of its cooling cycle is controlled by air parameter. However, for water and air combined circuits such as side chill, air parameter can be used either to clear out the water passage or gradual increase of cooling to prevent thermal shock to the cooling circuit.
- Water – Control parameter for duration of water flow for water and air combined circuits.
- Purge – Purge is exclusively used to water and air combined circuits after water flow. This is to minimise the boiling effects of residual water in cooling circuits,

where boiling residual water can rapidly and often undesirably increase the cooling effect.

Cooling circuit labelled side chill is highlighted in Figure 3-3 to indicate its location relative to rim and spoke junction as shown in Figure 1-8. Side chill circuit is considered as the most influential cooling circuit to control the thermal balance of the rim and spoke junction due to its close proximity to that area. Therefore timing of side chill circuit was selected as a main variable in this experiment.

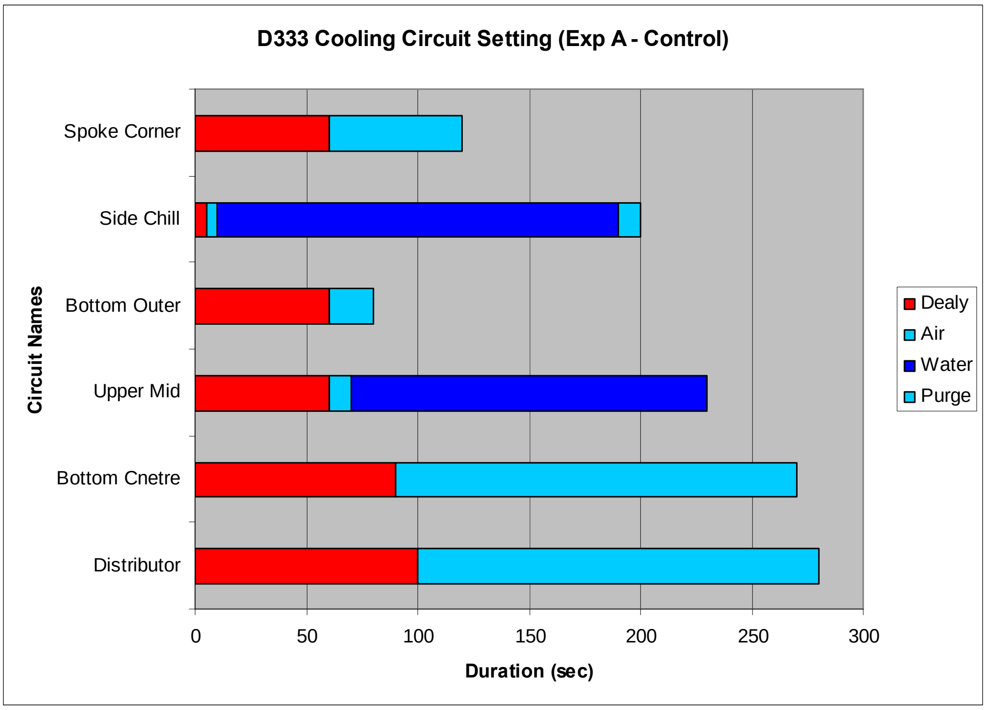

Figure 3-2 Timing based cooling circuit setting of D333 process.

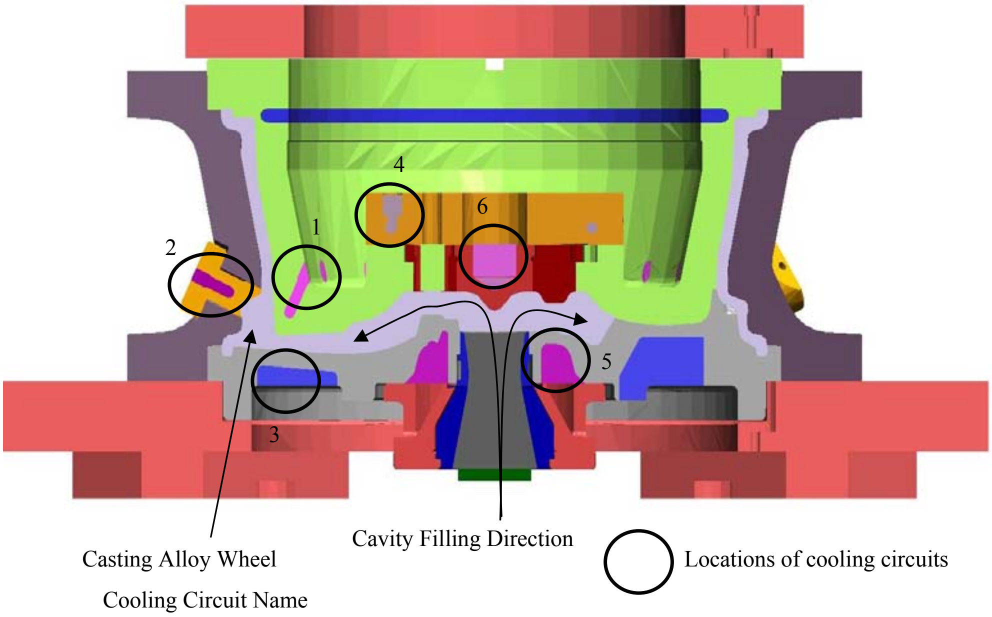

Cooling Circuit Name

1: Spoke Corner
2: Side Chill
3: Bottom Outer
4: Upper Mid
5: Bottom Centre
6: Distributor

Figure 3-3 Locations of various cooling circuits used in process setting of D333.

A detailed breakdown of the current side chill cooling circuit setting, set as a control, and three modified settings labelled Exp A-C are shown in Figure 3-4. Side chill circuit uses a combination of water and air as cooling fluid, where duration of each cooling fluid is carefully controlled. As previously mentioned, air parameter in side chill circuit is primarily used to clear out the water passage for a short duration of five seconds, hence providing the minimal cooling effect. Therefore, delay parameter and duration of water cooling were altered at three different levels to provide different cooling circuit duration, while overall cooling cycle of 200 seconds was maintained for all experiments. A summary of each experimental set up is shown in Table 3-1.

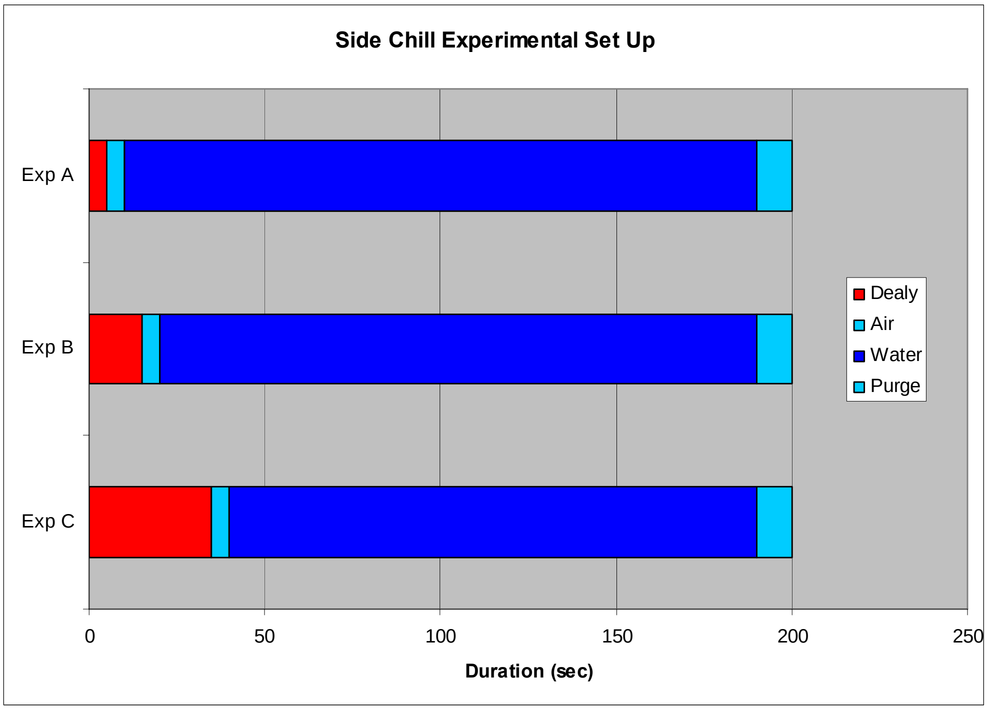

Figure 3-4 Detailed comparisons of side chill cooling circuit timing setting used for experimentation.

Table 3-1 Delay and duration of each cooling setting for the experiments.

Exp Label	Delay (sec)	Water (sec)
Exp A (Existing setting)	5	180
Exp B	15	170
Exp C	35	150

Timer setting of side chill cooling circuit for each experiment was adjusted through InTouch™ based control system on the casting machine. For each experiment, total 20 sample castings were gathered. However, it is important to note that the initial 10 samples of each setting were labelled "buffer" and discarded and only later 10 samples of 20 casting samples were used for analysis. It was assumed that those buffer samples were produced while the casting process experienced transient state after adjusting the cooling setting. Therefore, discarding these buffer samples for analysis was to ensure that samples for analysis were produced from a steady process. A schematic diagram of this particular sampling regime is shown in Figure 3-5.

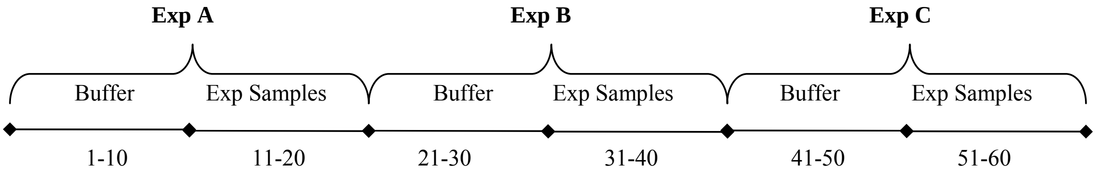

Figure 3-5 Sampling regime for the experiment.

3.3 Microstructural Analysis

Upon completion of casting experiments, several casting samples were selected and prepared for x-ray radiography and measurements of secondary dendrite arm spacing (SDAS).

Sample selection and preparation

For more detailed x-ray radiography, two casting wheels were selected from each casting experiment. 4th and 8th sample from 10 casting samples of each experimental setting were selected to ensure that the samples are produced from relatively steady process.

Due to a size restriction of x-ray radiography film used, only seven out of 15spokes of each wheel were selected. Total seven samples from evenly spread locations were selected for x-ray radiography analysis, as shown in Figure 3-6. Each spoke is labelled number 1 – 15 depending on its relative anti-clockwise location to a valve hole.

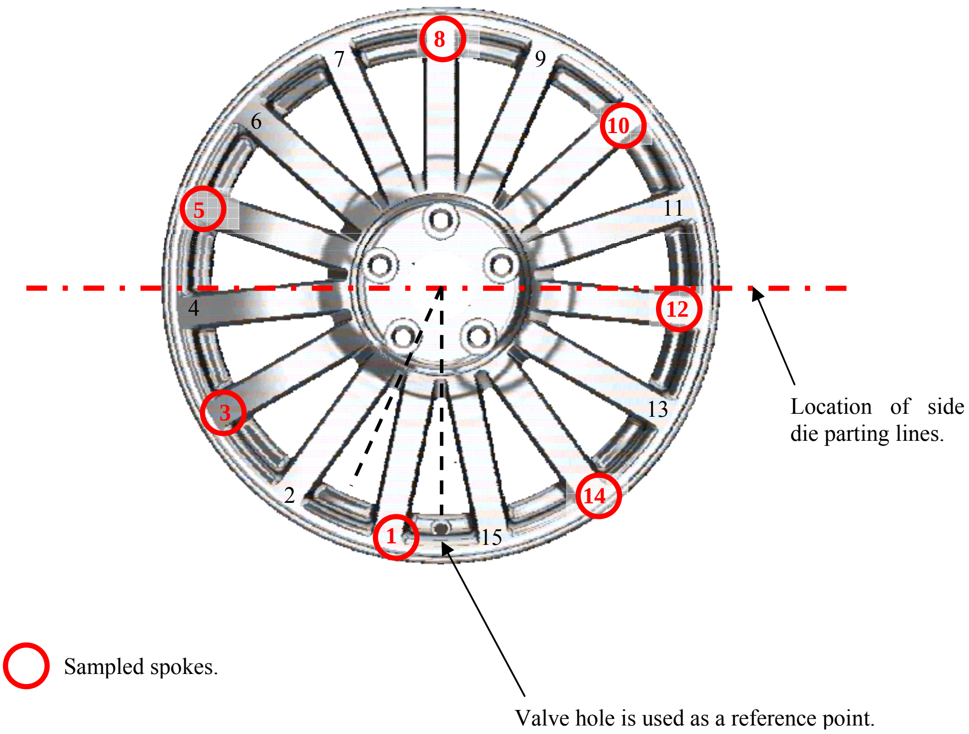

Location of side die parting lines.

Sampled spokes.

Valve hole is used as a reference point.

Figure 3-6 Locations of samples for x-ray radiography.

3.3.1 X-ray radiography

The purpose of x-ray radiography is to visually analyse the effect of each cooling setting by comparing the size of shrinkage porosity at the rim and spoke junction of each casting samples. Seven spokes from each cooling setting were selected, as shown Figure 3-6, using the method discussed in the previous section. Total 42 samples were then sectioned as shown in Figure 3-7, concentrating on rim spoke junction, and placed on A3 sized x-ray film for radiography. Each sample was then labelled according to labelling method shown in Figure 3-8.

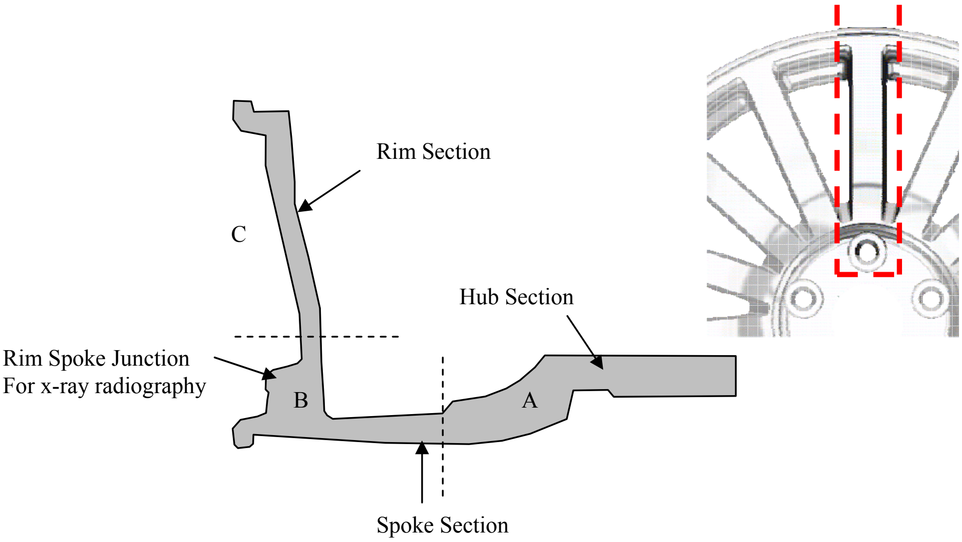

Figure 3-7 Location of samples for x-ray radiography and SDAS measurement.

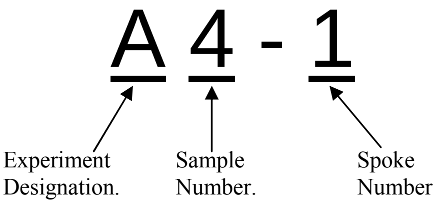

Figure 3-8 Sample labelling method.

3.3.2 SDAS Measurement

It was discussed in the previous chapter that there is a clear correlation between some thermal history parameters of a casting section, namely solidification time and cooling rate, and Secondary Dendrite Arm Spacing (SDAS). Therefore it was established that effectiveness of each cooling setting could be realised by SDAS measurements of casting samples, whose presence of shrinkage porosity was established from x-ray radiography analysis.

Sample A4-8 and D4-8 were selected and sectioned through its middle plane and polished using various grids of polishing pads to reveal its microstructure. The rim and spoke junction of each sample was then marked with 54 grids of 5mm by 5mm as shown in Figure 3-9, hence a specific location of each SDAS measurement can be identified. In order to precisely identify the location of each measurement within the grid, datum points for both x and z axis were defined. Spoke face is defined as a datum point for z-axis and bead seat is defined as a datum point for x-axis.

Using an optical microscope equipped with a digital camera, a montage of 5mm by 5mm grids was constructed in a manner shown in Figure 3-9. It was measured that the microscope was capable of taking an image with a resolution of 1024 pixels by 768 pixels. With the specification magnification used for SDAS measurement, it was determined that an actual area of 1.33 mm by 1 mm could be captured by a single frame of a digital image. By moving the specimen table of the microscope at set horizontal interval and in a sequence shown in Figure 3-9, microstructural image of each 5 mm by 5 mm grid could be captured, as shown in Figure 3-10. This is repeated for the rest of 54 grids, hence a digital image of the entire rim and spoke junction mapped and labelled. By this method, a specific location of each image could be recorded along with SDAS measurement, hence providing a very detailed SDAS mapping of the entire rim and spoke junction.

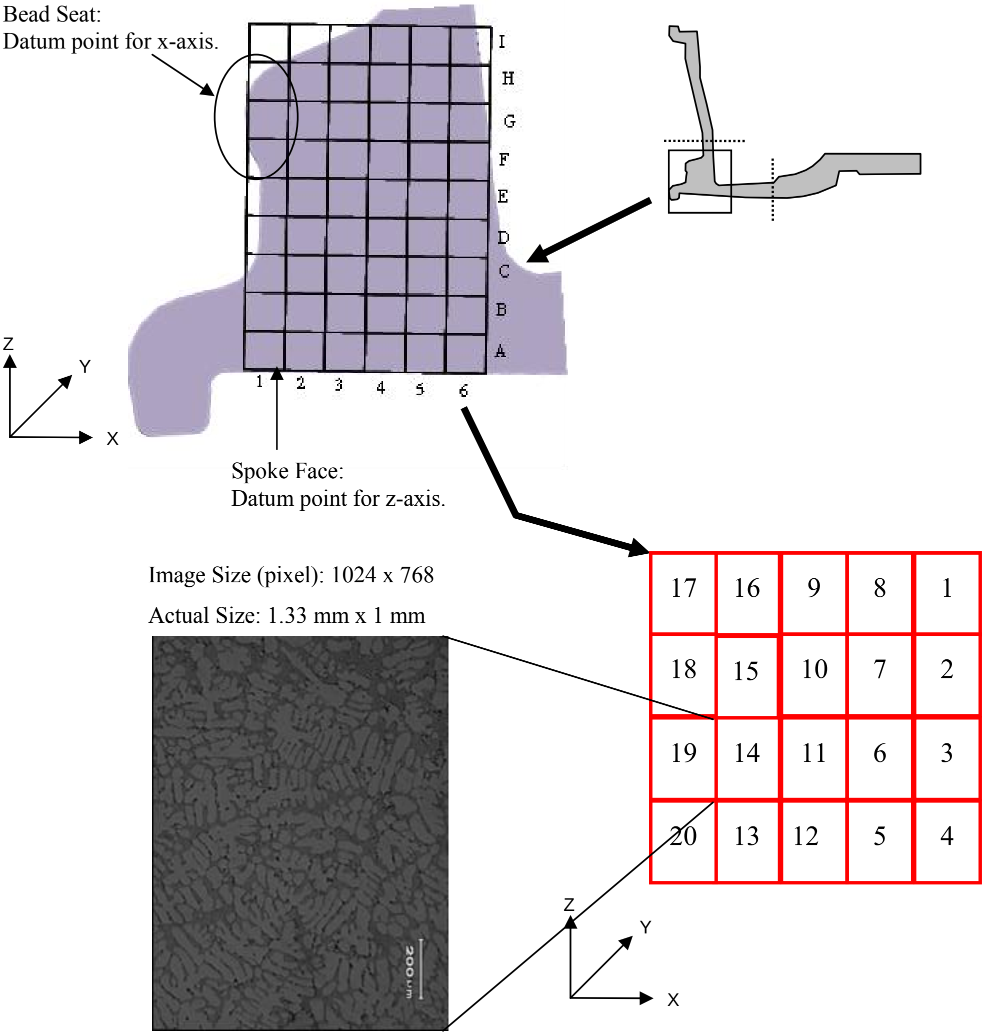

Bead Seat:
Datum point for x-axis.

Spoke Face:
Datum point for z-axis.

Image Size (pixel): 1024 x 768

Actual Size: 1.33 mm x 1 mm

17	16	9	8	1
18	15	10	7	2
19	14	11	6	3
20	13	12	5	4

Figure 3-9 Method of taking images for SDAS measurement.

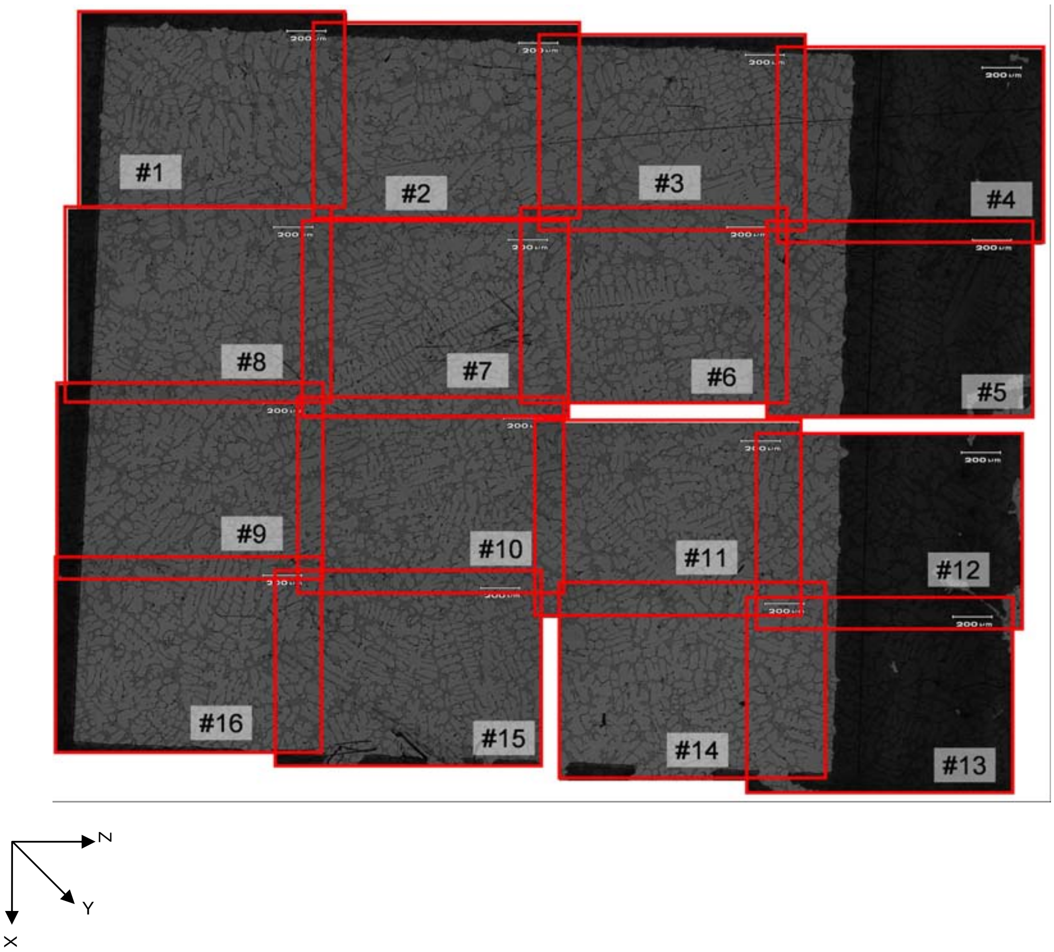

Figure 3-10 Combined images of 5mm by 5mm grid.

Each image is then analysed using commercially available digital image analysis software ImagePro™ to measure dendrite arm spacing. A sample screen shot of the software and its control panels are shown Figure 3-11.

First of all the scale bar shown in microscope image is measured for calibration purpose. Calibration of ImagePro™ software is done by measuring a known distance, e.g. a scale bar, and counting its corresponding number of pixels in the image. Therefore the same calibration factor can be used when measuring SDAS by counting the number of pixels in individual arm spacing.

Once the calibration is completed, each image is then digitally enhanced by using a low pass filter to improve the contrast between aluminium dendrite (lighter colour) and its surrounding eutectic (darker colour). By visually inspecting dendritic arms structures, a group of secondary arms that are originated from the same primary arm can be identified. They are often characterised by similar sized individual arms with the same growth direction. An example of typical image of secondary arms is shown in Figure 3-12. For an actual measurement of SDAS, a line is drawn perpendicular to the growth direction of secondary arms to indicate arms for measurements. By detecting the contrast between dendrite arms and eutectic structure, ImagePro™ can automatically identifies individual arm and centre to centre distance between each arm. It is shown in Figure 3-12 where yellow bars indicate position and approximated width of individual dendrite arm and red bars indicate estimated centre of individual dendrite arm.

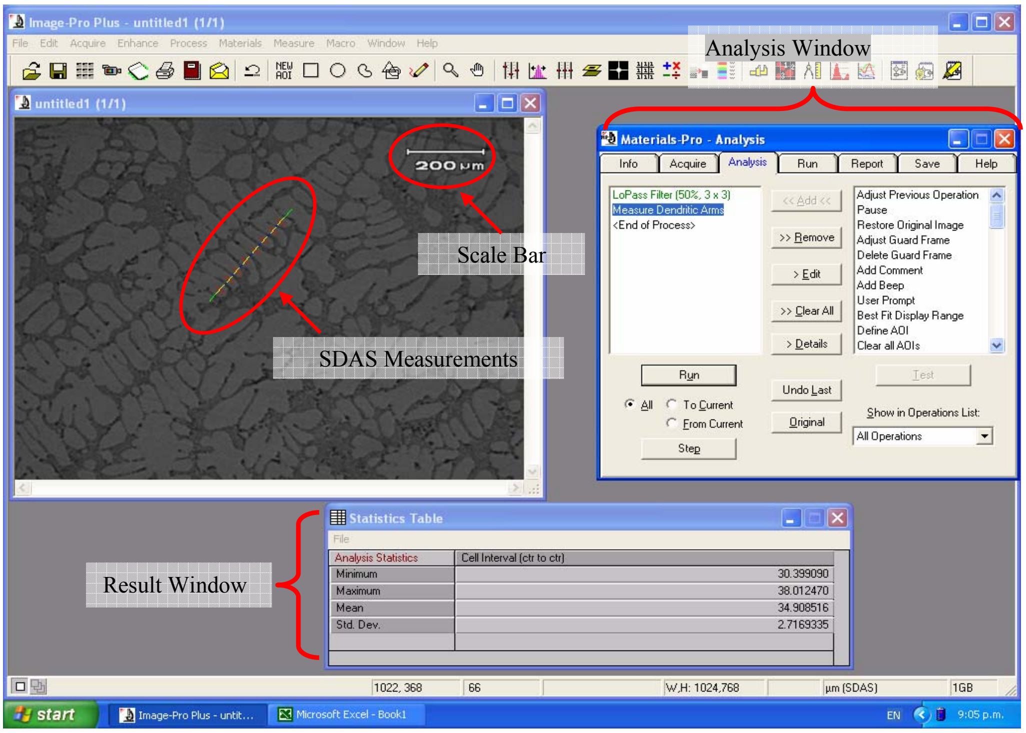

Analysis Statistics	Cell Interval (ctr to ctr)
Minimum	30.399090
Maximum	38.012470
Mean	34.908516
Std. Dev.	2.7169335

Figure 3-11 Sample screen shot of ImagePro™.

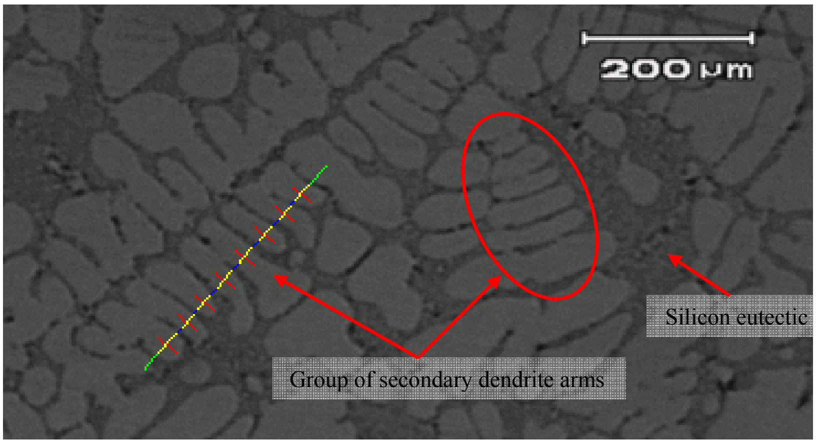

Figure 3-12 An example of secondary dendrite arm spacing measurement.

It is the centre to centre distance of each dendrite arm that is the main focus of SDAS measurement. Measured in unit of micron, SDAS is then recorded in Excel spread sheet. This is then repeated for the rest of 16 images representing a grid of 5 mm by 5 mm shown in Figure 3-9. An average value of SDAS from all 16 images is taken and recorded as average SDAS value for a specific location within rim and spoke junction. Through these SDAS measurements, a detailed mapping of SDAS, hence a local cooling rate, within the rim and spoke junction of each casting sample is expected.

3.4 Numerical Modelling

For numerical analysis of the Exp A and Exp C, commercially developed simulation package MAGMASoft™ is used. MAGMASoft™ consists of three components, pre-processor, computing module and post-processor.

In pre-processor module, all the necessary boundary and initial conditions of model are defined and enmeshment is performed to produce appropriate mesh size.

Boundary conditions of model can be grouped into the followings.

- Interfacial heat transfer coefficients between various die parts and casting.
- Cooling circuit heat transfer coefficient.

Interfacial heat transfer coefficient is defined as a resistance to heat flow between two different bodies of system. In the case of casting process simulation, there are three main types of interfacial heat transfer coefficient to be considered.

- Interface between casting and mould parts.
- Interface between two different mould parts.
- Interface between mould parts and ambient air.

Detailed literature review on interfacial heat transfer coefficient between casting and mould parts has been presented in the previous chapter - 2.3. Therefore it will not be discussed again in this chapter. However, a brief introduction on two other interfacial heat transfer coefficients will be presented in this section.

Interfacial heat transfer coefficient between two mould parts can be approximated as a constant value to simulate the metal to metal contact. Non perfect contact is assumed between two metal surfaces due to surface roughness of mould parts. Therefore a constant heat transfer coefficient is used to simulate the effect of small air gaps between two surfaces as discussed in previous section 2.3. Heat transfer coefficient of 1000 W/m^{2}K from the database of MAGMASoft™ is used for typical metal to metal contact [41].

In order to model the effect of cooling circuits, a range of effective heat transfer coefficient values were applied as discussed in the previous section 2.2. Experimentally determined values [19] for both water and air cooling through side chill cooling channels were used in this modelling. Very low value of heat transfer coefficient, 20 W/m^{2}K, is used to simulate the effect of no cooling fluid flow in the channel. For water and air, 1500 W/m^{2}K and 500 W/m^{2}K of effective heat transfer coefficients were used respectively. A summary of effective heat transfer coefficients for side chill cooling used in numerical modelling of casting experiment is shown in Figure 3-13.

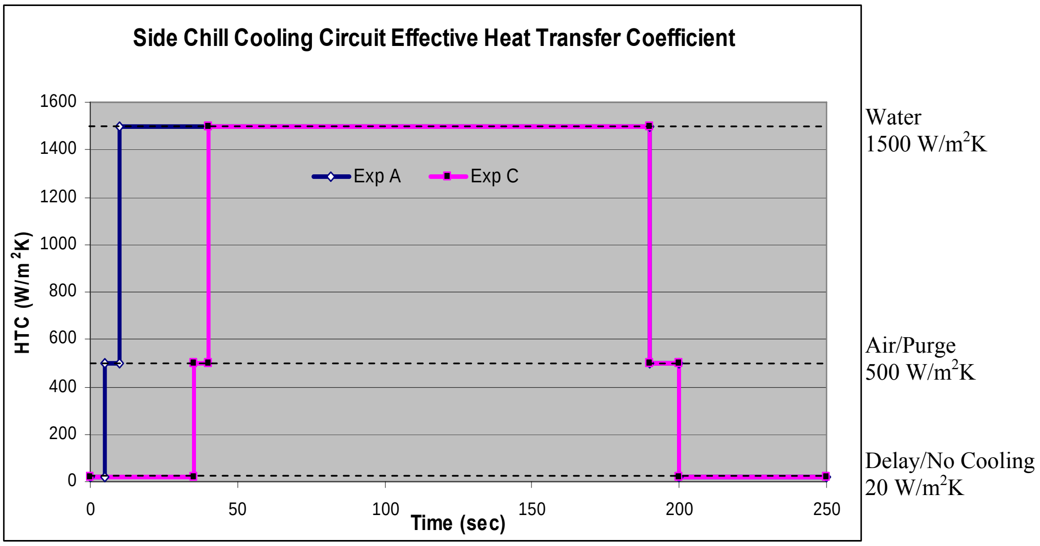

Figure 3-13 Interfacial heat transfer coefficient setting for the cooling circuit for numerical modelling.

Another important step in pre-processing is to specify the locations of control plots. Control plot is a terminology that is used in MAGMASoft™ modelling which describes a specified coordinate points that records numerical results of modelling. In this instance, three control plots are defined for representing each of SDAS measurement grids, as shown in Figure 3-14. The intension to take an average value of local cooling rate from three control plots for each grid, therefore average value of SDAS can be numerically calculated. This numerically calculated value of SDAS then can be compared against the measured SDAS of corresponding grid for further analysis.

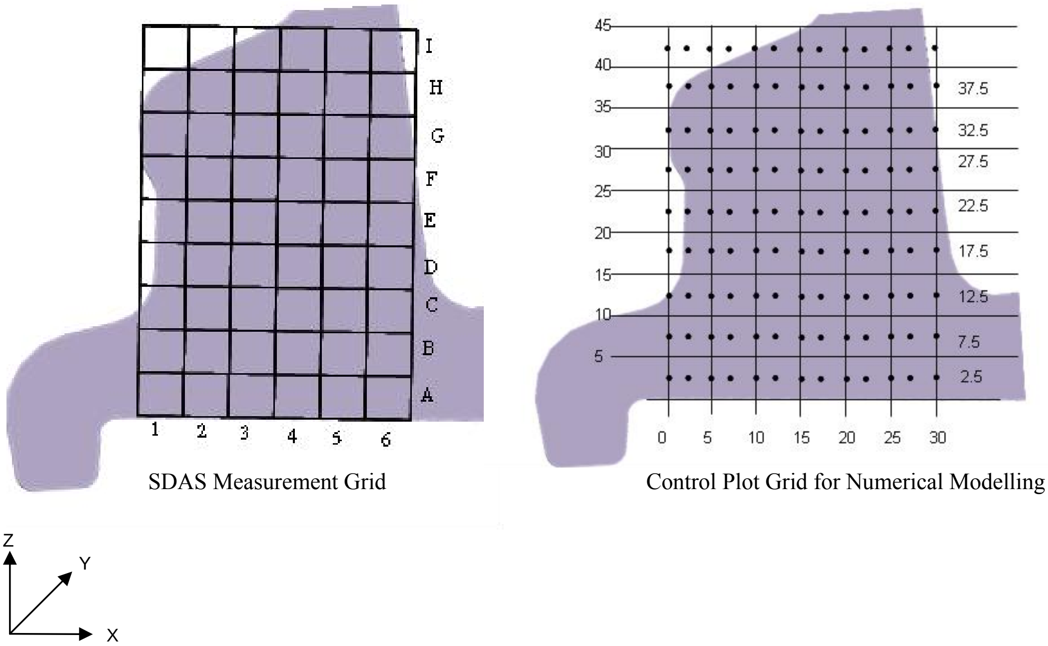

SDAS Measurement Grid

Control Plot Grid for Numerical Modelling

Figure 3-14 Locations of control plots, where numerical data is measured.

Each model with different experimental condition runs for 10 cycles, hence cyclic effects of die casting process can be considered. The numerical results from control plots are then taken from 10th cycle to ensure that the process has reached its stable condition.

3.5 Chapter Summary

Detailed experimental settings for Exp A and Exp C are discussed. This is then followed by sample preparation methods for secondary dendrite arm spacing measurements and x-ray radiography analysis. Finally details of numerical model set up were also presented. The results from secondary dendrite arm spacing (SDAS) measurements, x-ray radiography and numerical modelling will be discussed in detail in the following chapter.

4 Results and Discussion

In this chapter, results from the following areas will be discussed.

- Effect of cooling timing on morphology of solidification shrinkage through x-ray radiography analysis.
- Effect of cooling timing on local solidification time predicted by secondary dendrite arm spacing (SDAS) measurements.
- Numerical modelling of different cooling effect on numerically predicted solidification time.

4.1 Effects of Cooling Timing on Solidification Shrinkage

Solidification shrinkage porosity, which the main aspect of this research, has been measured using x-ray radiography. Due to relatively light density of aluminium alloy, x-ray radiography of porosity shrinkage often produces very weak contrast. A sample image of porosity shrinkage in rim spoke junction is shown in Figure 4-1. Despite its reasonably large size, it is yet difficult to visually identify it.

In order to properly identify the size of shrinkage porosity in each x-ray radiography image, a method of digitally enhancing the gamma of each image was used. Adjustment of the gamma improves the contrast of dark part of the image. Shrinkage porosity of x-ray radiography is shown as darker area due to its lighter density than aluminium alloy. Therefore, adjustment of the gamma would provide an adequate level of contrast for shrinkage porosity. The same image from Figure 4-1 is shown in Figure 4-2 after its gamma is adjusted to produce more prominent image of porosity shrinkage.

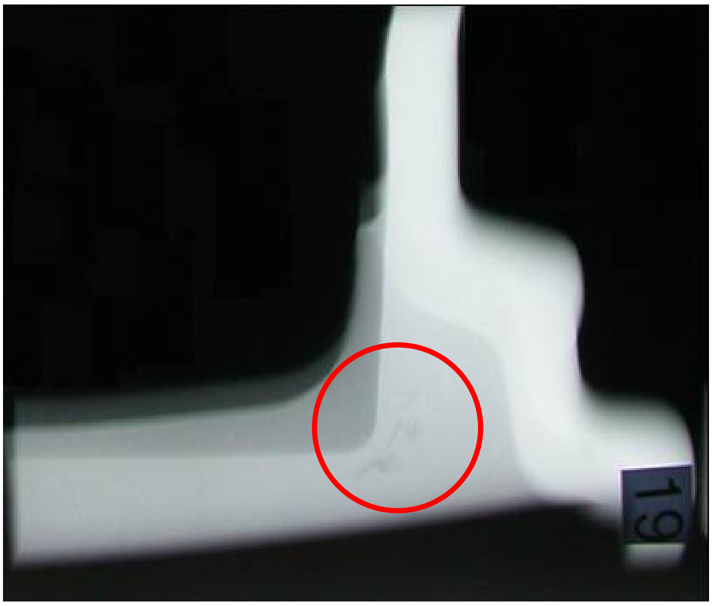

Figure 4-1 A sample x-ray image before processing.

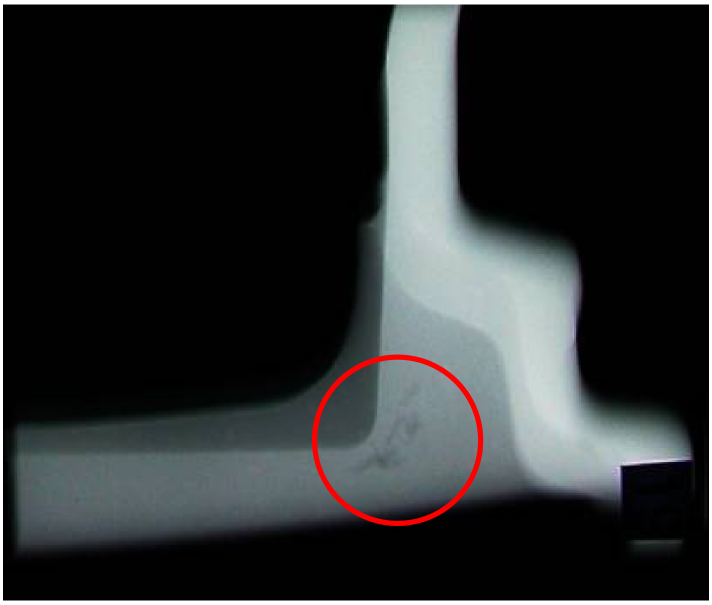

Figure 4-2 A sample x-ray image after processing.

Four different grades, ranging from 0 to 3, are used to gauge the relative size of shrinkage porosity in rim and spoke junction. Detailed definition and examples of each grade are as follows.

- Grade 0: No visible shrinkage porosity in a radiography image, Figure 4-3
- Grade 1: One small shrinkage porosity visible in a radiography image, Figure 4-4.
- Grade 2: One or more small cluster of shrinkage porosity visible in a radiography image, Figure 4-5.
- Grade 3: One or more large cluster of shrinkage porosity visible in a radiography image, Figure 4-6.

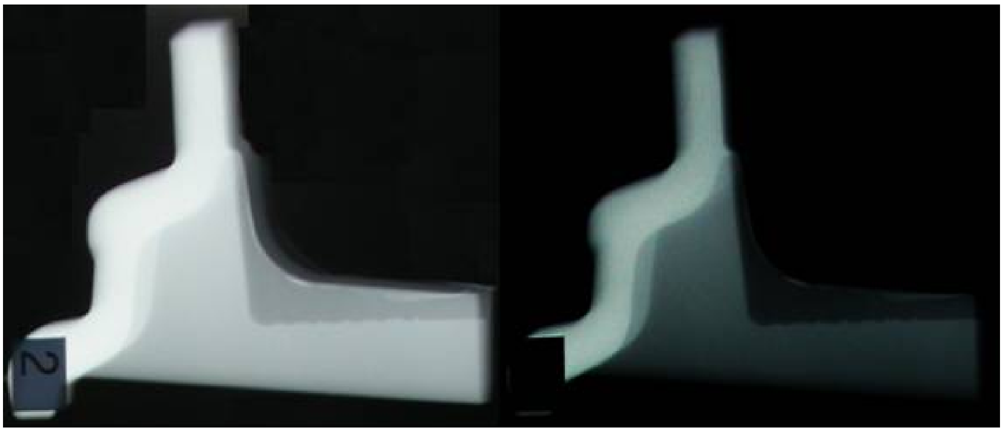

Example Grade 0:
Before gamma adjustment

Example Grade 0:
After gamma adjustment

Figure 4-3 A comparison of grade 0 samples.

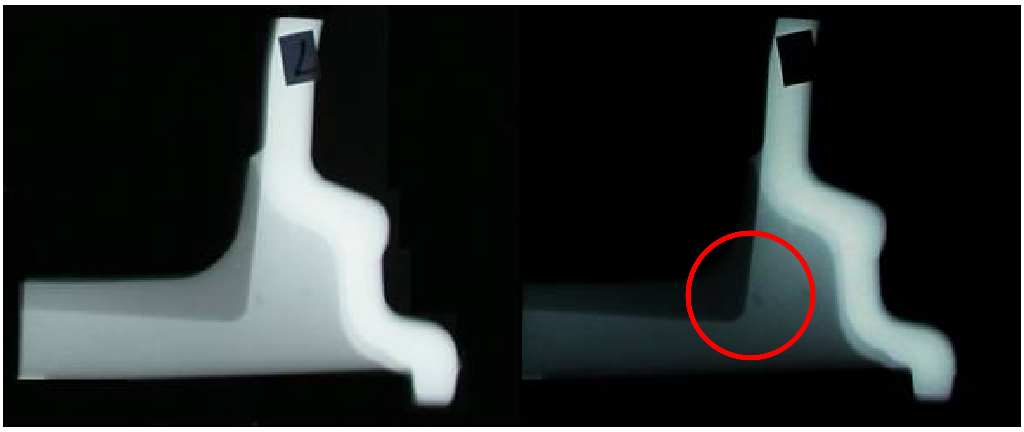

Example Grade 1:
Before gamma adjustment

Example Grade 1:
After gamma adjustment

Figure 4-4 A comparison of grade 1 samples.

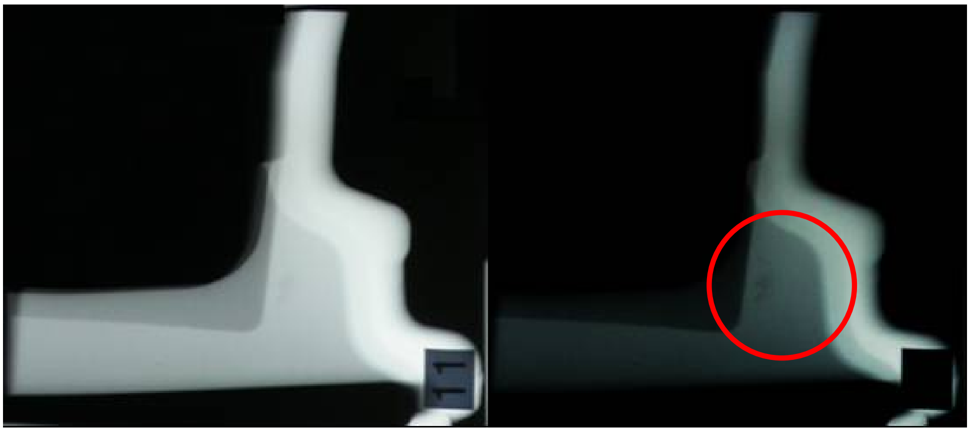

Example Grade 2:
Before gamma adjustment

Example Grade 2:
After gamma adjustment

Figure 4-5 A comparison of grade 2 samples.

Example Grade 3:
Before gamma adjustment

Example Grade 3:
After gamma adjustment

Figure 4-6 A comparison of grade 3 samples.

Collated images of individual sample are attached in Appendix A. Presentation of qualitative analysis of x-ray radiography results Exp A and Exp C (detail of experimental condition is presented in Table 3-1) is shown in Figure 4-7. Both x-ray results show increased number of shrinkage count for Exp C, while Exp A shows the least amount of shrinkage count. This supports the initial hypothesis that less cooling in rim and spoke junction increases the tendency of shrinkage porosity due to isolated hot spot.

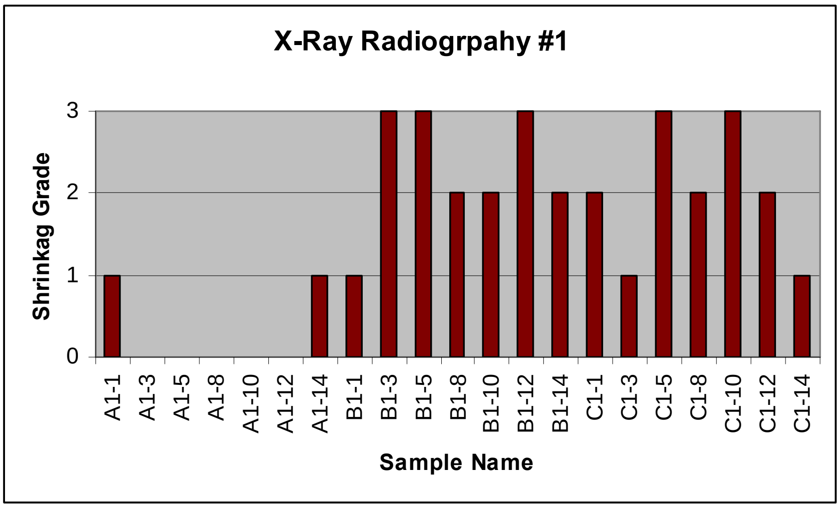

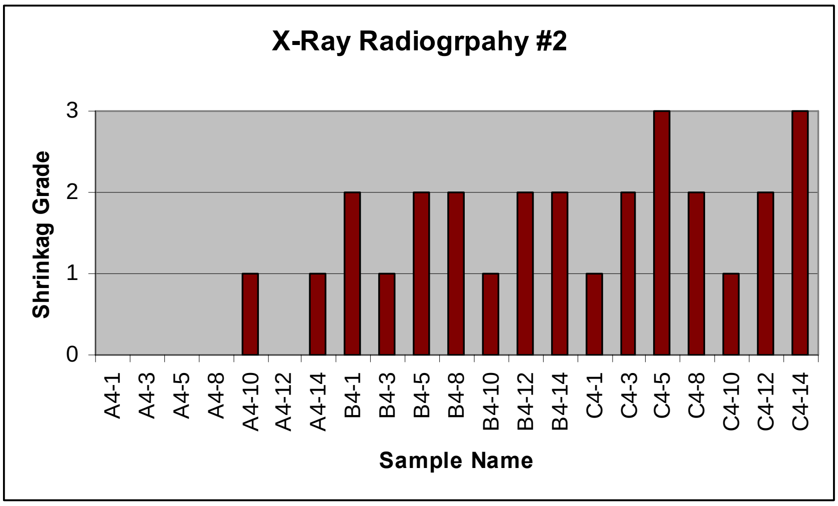

Figure 4-7 Results of shrinkage counting from Exp A and Exp C x-ray analysis.

Note: See Figure 3-8 for sample identification method.

4.2 Effect of Cooling Timing on SDAS

4.2.1 Processing of Results

Once SDAS is measured using digital image analysis software ImagePro™, it is then plotted in Excel spreadsheet as shown in Figure 4-8. As it was discussed in the previous section, 3.3.2, each recording then represents a measurement of SDAS at specific location within the cross section of the rim and spoke junction.

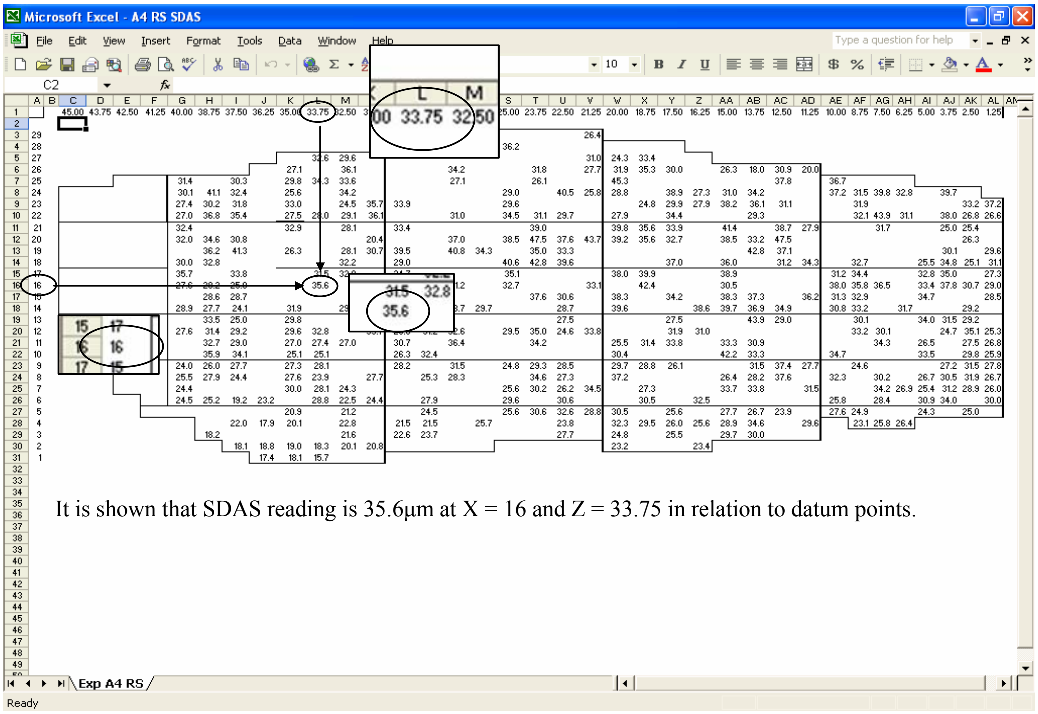

It is shown that SDAS reading is 35.6µm at X = 16 and Z = 33.75 in relation to datum points.

Figure 4-8 Sample of SDAS result recording showing a measurement at specific location.

Over 400 measurements were recorded for each timing delay of cooing condition. In order to present this large quantity of data in more effective way, it was necessary to further process the data by taking average value at set interval. A cross section of rim spoke junction with its chill location is shown in Figure 4-9. Considering the chill geometry, it was a reasonable assumption that major heat flow direction would be in he direction of x-axis. Therefore, it was decided that an average value of four measurements along z-axis at each point of x-axis. This average scheme is illustrated in Figure 4-9. Finally it is repeated for every 5mm interval to produce averaged SDAS along the x-axis of rim and spoke junction at the following height.

- SDAS measurements at z = 2.5 mm, 7.5 mm, 12.5 mm, 17.5 mm, 22.5 mm, 27.5 mm, 32.5 mm and 37.5 mm.

Overall results of SDAS measurements along the x-axis at the above interval are presented in Figure 4-10 to Figure 4-17.

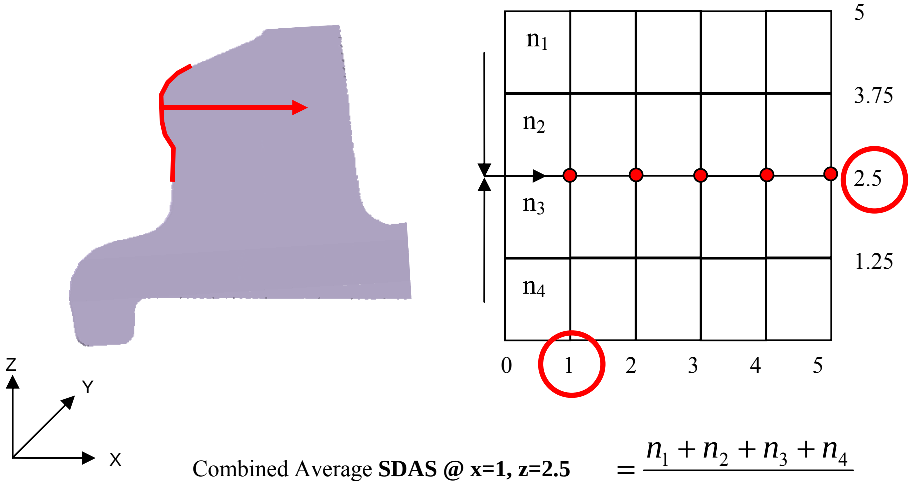

Combined Average **SDAS @ x=1, z=2.5** $= \dfrac{n_1 + n_2 + n_3 + n_4}{4}$

Figure 4-9 Averaging method of SDAS measurement for each 5mm by 5mm grid.

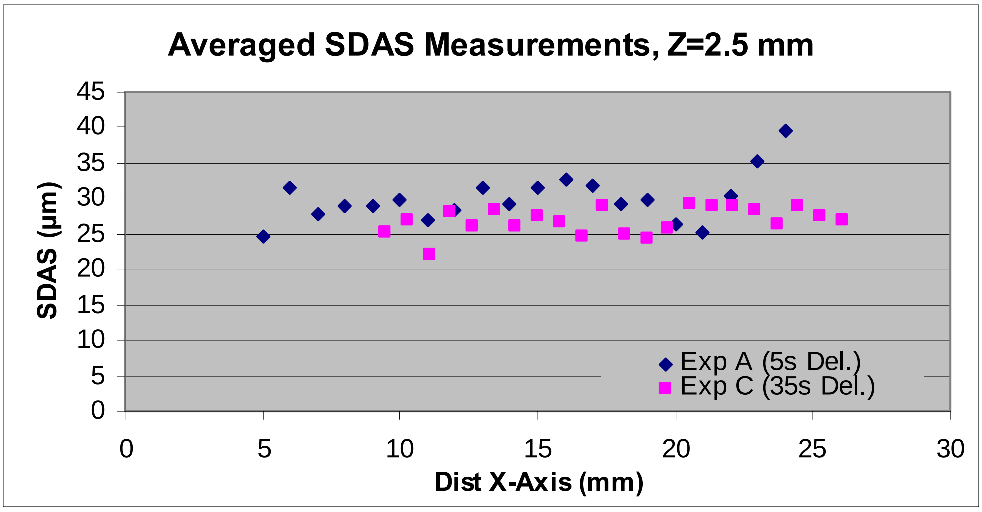

Figure 4-10 Averaged SDAS measurement at Z=2.5.

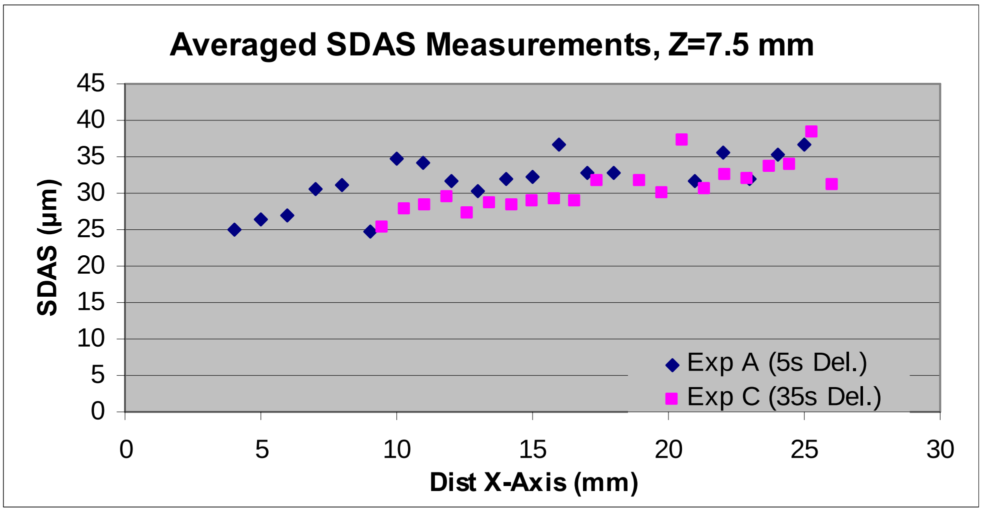

Figure 4-11 Averaged SDAS measurement at Z=7.5.

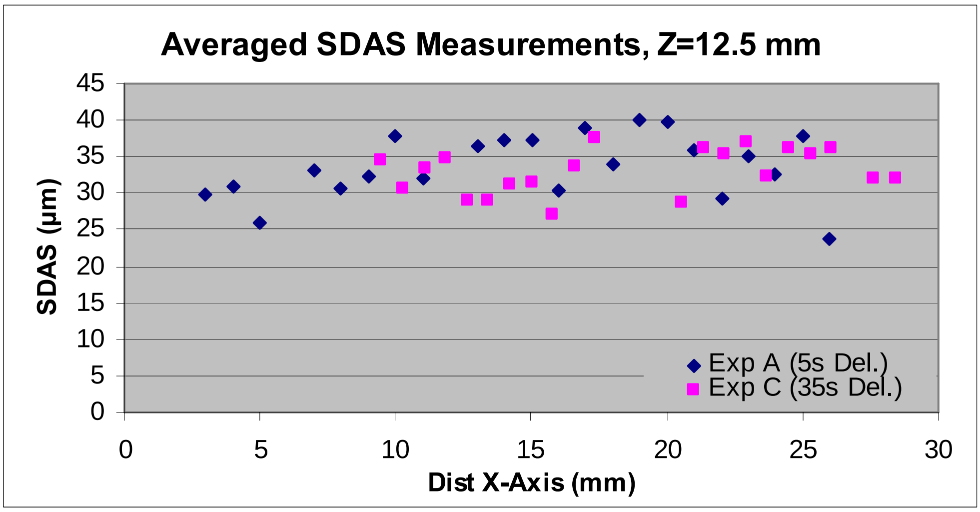

Figure 4-12 Averaged SDAS measurement at Z=12.5.

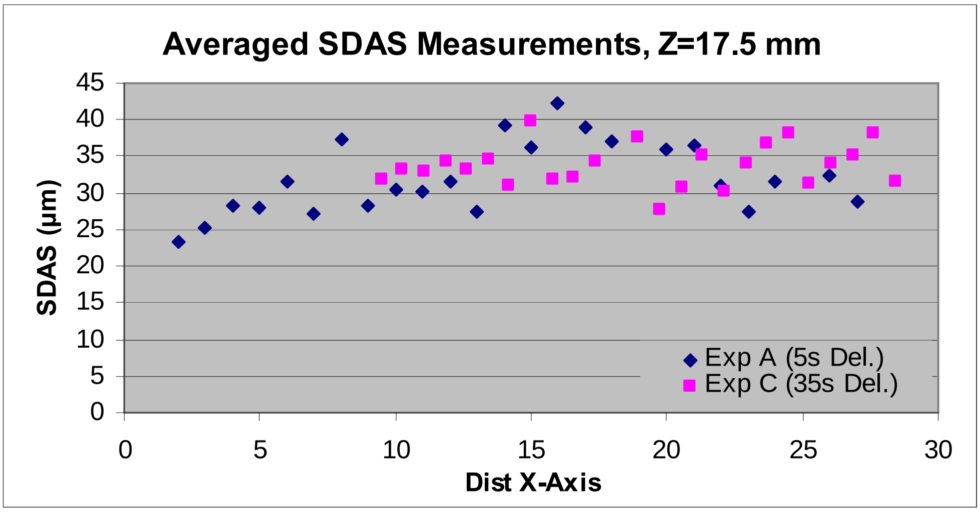

Figure 4-13 Averaged SDAS measurement at Z=17.5.

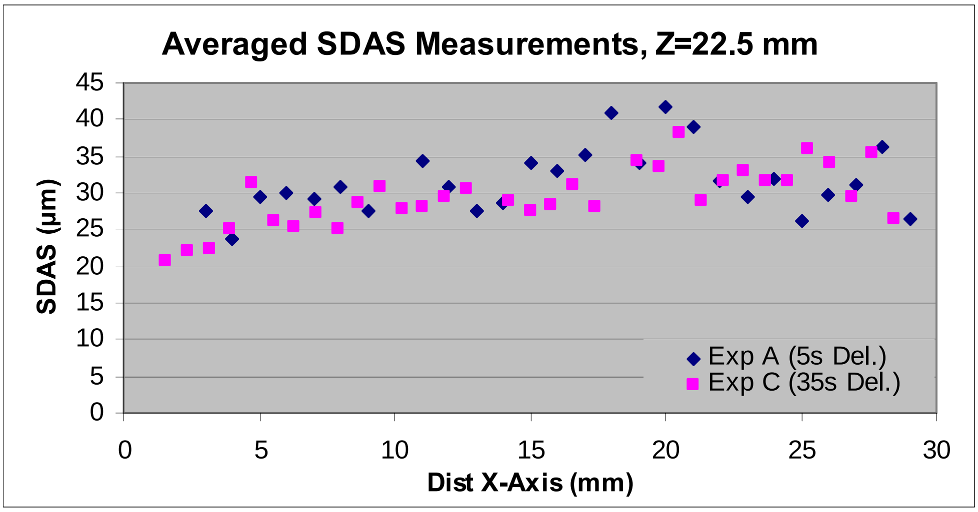

Figure 4-14 Averaged SDAS measurement at Z=22.5.

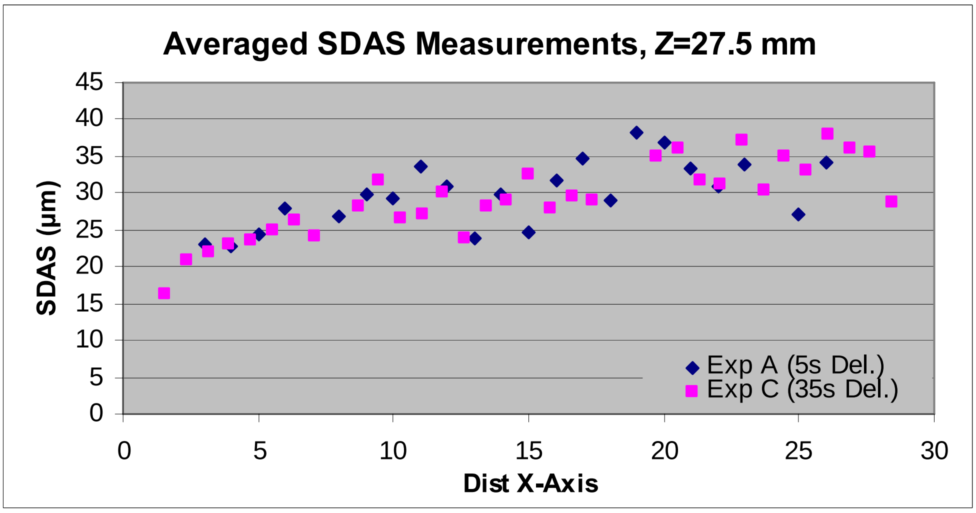

Figure 4-15 Averaged SDAS measurement at Z=27.5.

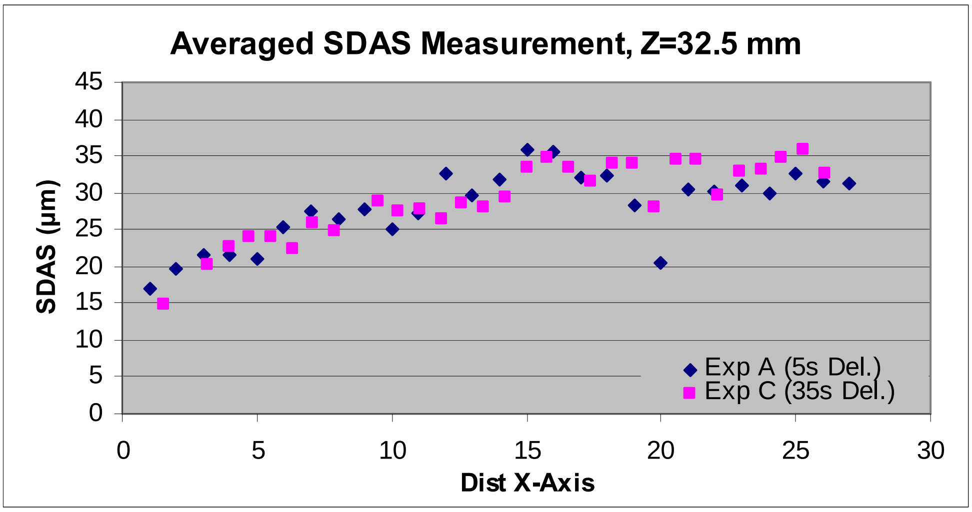

Figure 4-16 Averaged SDAS measurement at Z=32.5.

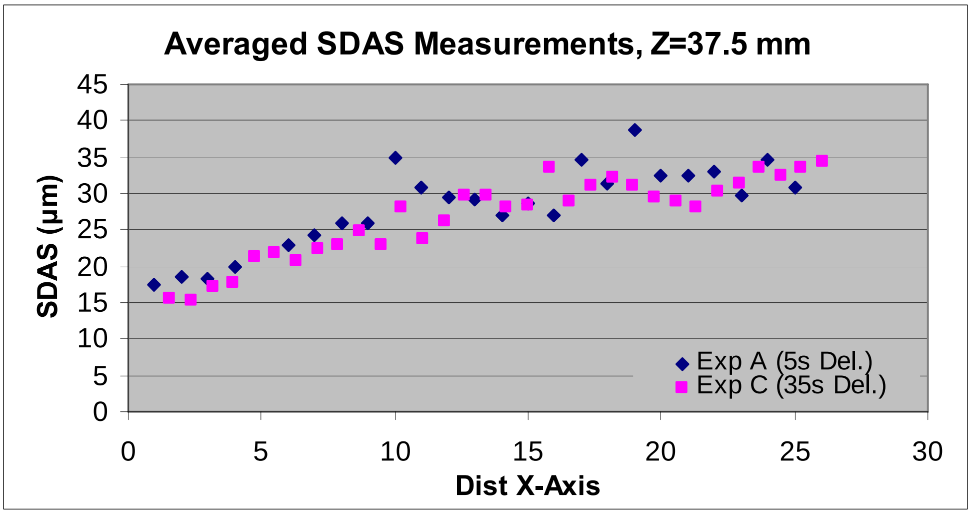

Figure 4-17 Averaged SDAS measurement at Z=37.5.

4.2.2 Discussions

First of all, in order to asses the effect of applied cooling on rim and spoke junction, averaged SDAS measurements at z-axis locations between 22.5 mm and 37.5 mm were analysed. These locations were selected as it corresponds to a direct interface to the cooling circuit. A logarithmic line of best fit is superimposed over the averaged SDAS measurement and they are shown in Figure 4-18 to Figure 4-21.

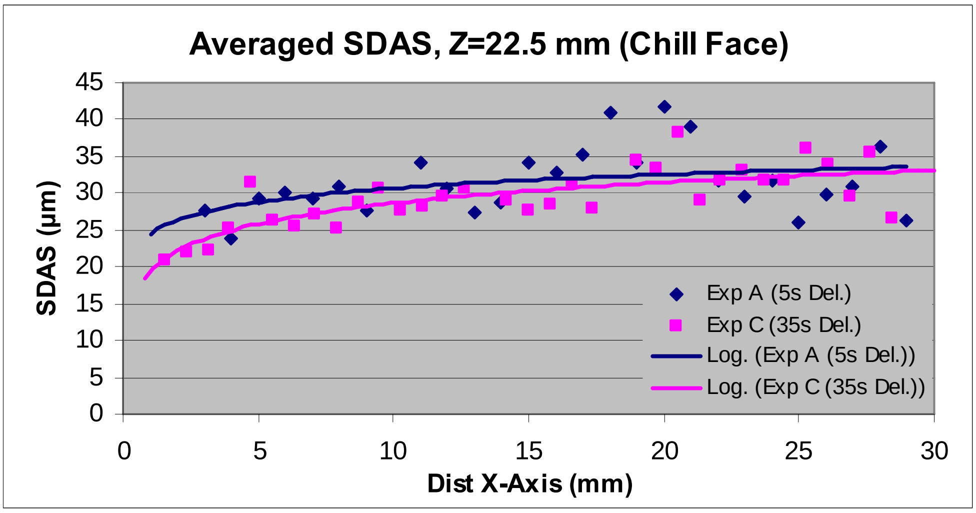

Figure 4-18 Averaged SDAS measurement with logarithmic line of best fit at Z=22.5.

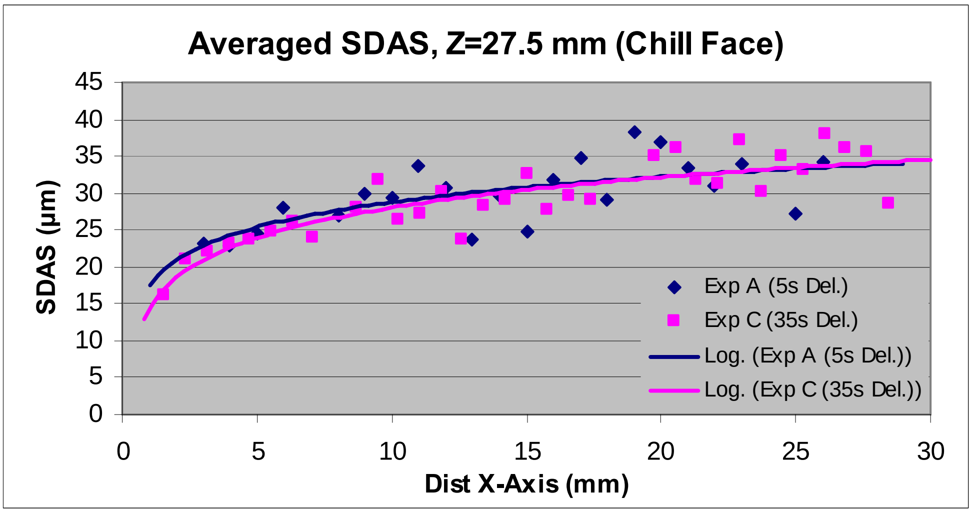

Figure 4-19 Averaged SDAS measurement with logarithmic line of best fit at Z=27.5.

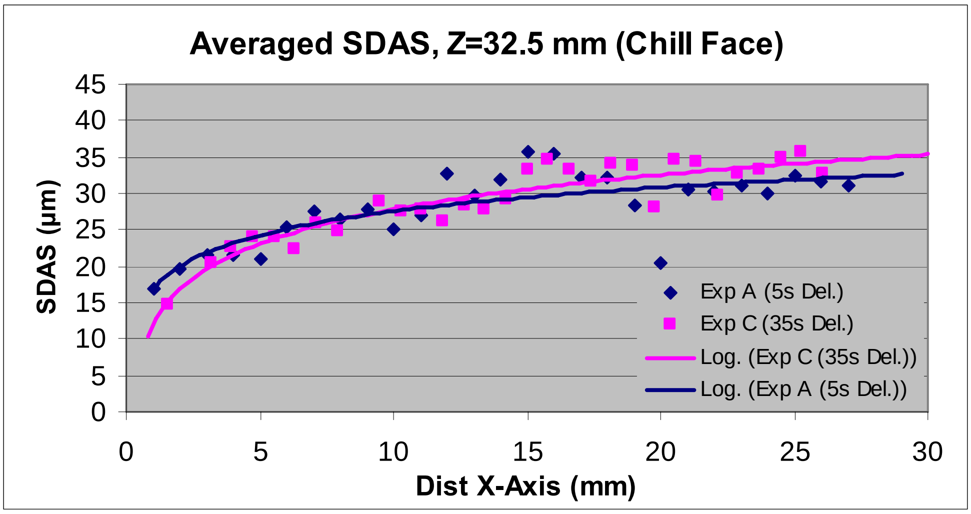

Figure 4-20 Averaged SDAS measurement with logarithmic line of best fit at Z=32.5.

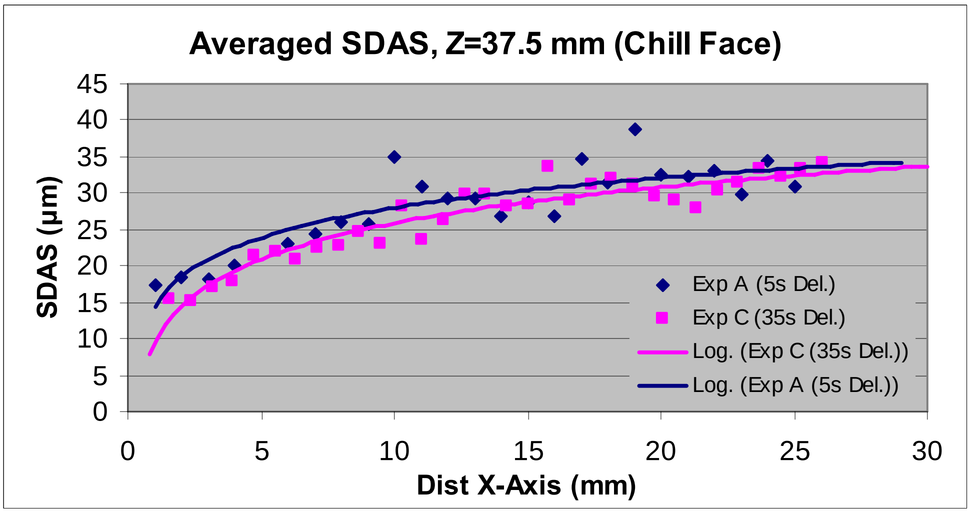

Figure 4-21 Averaged SDAS measurement with logarithmic line of best fit at Z=37.5.

General Observation

Relatively small dendrite arm spacing is observed between 0 to 10 mm along the x-axis. Also, more pronounced drop in average dendrite arm spacing is observed around 5 mm along the x-axis for all four heights along the z-axis. It is believed that chilling effect of cooling circuit, hence relatively rapid cooling rate or solidification time, is responsible for producing such small dendrite arm spacing measurements. Sample dendrite arm spacing image from a location close to the cooling circuit is shown in Figure 4-22 showing its fine dendritic structure, recorded measurement of 15.3μm. In contrast, much coarser dendritic structure, recorded measurement of 37.9μm, is shown in a sample image from a location further away from the cooling circuit is shown Figure 4-23. X and z coordinate indicating its approximate distance from the cooling circuit is also shown with the both image.

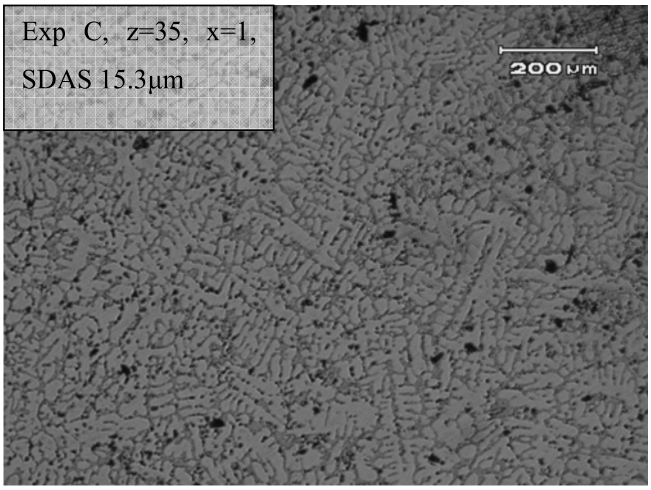

Figure 4-22 A sample image of fine dendritic structure seen near the chill face.

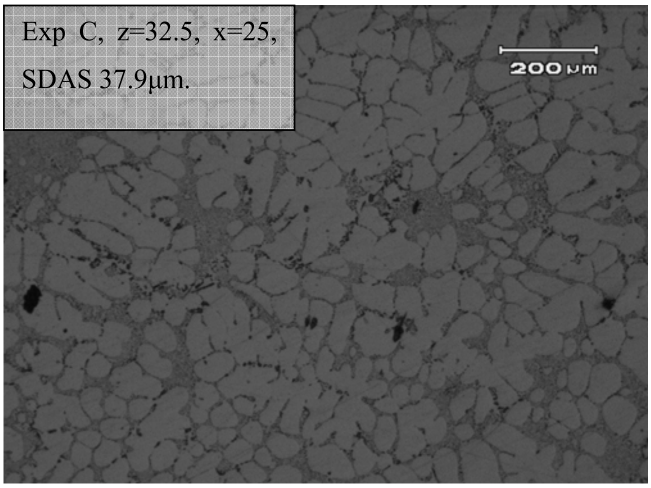

Figure 4-23 A sample image of coarse dendritic arms seen near the hot spot in rim spoke junction.

Effect of Cooling Timing

Contrary to the initial expectation of Exp A (5s Del.) producing finer dendrite arms near the chill face due to its longer duration of applied cooling, a conflicting trend was observed. Analysis of overlapped logarithmic line of best fit near the chill face shows that Exp C (35s Del.) shows stronger tendency of finer micro structure near the chill face than Exp A (5s Del.). Measurement error can be one of contributing factors, however consistent trend was evident at all locations as shown in Figure 4-18 to Figure 4-21. This indicates that there must be other factors for this conflicting trend.

It was discussed in the literature review, section 2.3.2, that increased interfacial heat transfer coefficient at mould and casting interface was observed when mould temperature was increased [26, 28]. It was explained that increased mould temperature would help molten metal to retain its superheat longer. Therefore the molten metal would retain much better fluidity and improved contact between the mould surface and molten metal. Assumption is made that reduced duration of applied cooling for Exp C (35s Del.) would contribute to increased mould temperature, hence increased interfacial heat transfer coefficient. Increased interfacial heat transfer coefficient would result in increased amount of heat removed from the casting and possibly greater local cooling rate. Therefore, it is possible to observe finer dendrite arms (greater local cooling rate) at the chill face, or mould casting interface, despite less duration of applied cooling as in Exp C (35s Del.) vs. Exp A (5s Del.). An illustration of this phenomenon is shown in Figure 4-24.

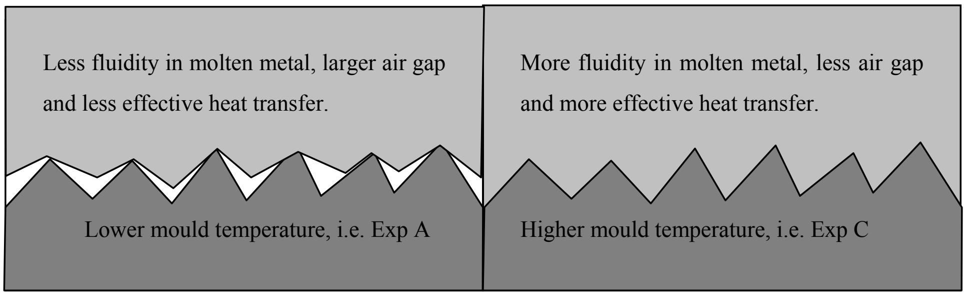

Figure 4-24 Illustration of a possible of reason for finer SDAS, hence faster local solidification time, for Exp C than Exp A.

It is also noted that there is insignificance difference in SDAS in the hot spot (areas between 15-25mm in x-axis). Initially it was expected that increased amount of cooling used in Exp A would aid reduction of hot spot in rim and spoke junction as shown in Figure 1-8 and local solidification of hot spot measured by SDAS would indicate quantify this. In this research, longest solidification time, hence the hot spot, is shown in the area along x-axis of 20-30mm. However, insignificant difference in local solidification time at this hot spot between Exp A (5s Del.) and Exp C (35s Del.) is clearly shown in Figure 4-18 to Figure 4-21. This suggests that duration of cooling circuit is somewhat ineffective to reduce the hot spot in the rim and spoke junction.

It is suggested that formation of air gap at the casting and cooling interface is responsible for this effectiveness of increased cooling duration. As discussed previously in Section 2.3, air gap formation takes place at the casting and cooling circuit interface as solidifying metal pulls itself away from the interface due to thermal contraction.

Reduction in efficiency of cooling circuit due to air gap formation has been reported using different cooling circuit materials elsewhere [25, 28, 29, 30]. It is now apparent in this research that air gap formation can also affect the efficiency of cooling circuits with different duration of applied cooling media.

Prediction of Hot Spot Location

Analysis of averaged SDAS measurements also revealed that relatively large sized dendrite arms (>35μm) were recorded at particular locations. Majority of these large dendrite arms were concentrated between 15-20mm along the x-axis and 12.5 -27.5mm along the z-axis, as shown in Figure 4-25. This indicates that the local cooling rate of the highlighted area in the diagram is relatively slower than its surrounding regions, suggesting the existence of a local hot spot. However, a visual analysis of x-ray radiography shows that the local hot spot indicated by dendrite arm spacing measurements did not overlap with the actual location of porosity shrinkage. It is clearly shown in Figure 4-25 that the actual location of typical porosity shrinkage in rim poke junction is much closer to the corner of the junction or between 25-30mm along the x-axis. Meanwhile, measurements of SDAS show that the local hot spot is located between 15-20mm along the x-axis.

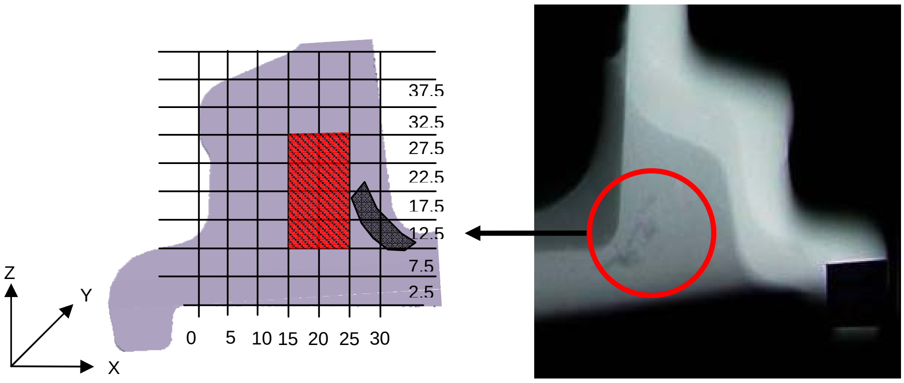

Figure 4-25 Location of identified hot spot by SDAS measurement and x-ray radiography.

Further examination of individual images of dendrite samples at two different locations along the x-axis, 20-25mm and 25-30mm, revealed some noteworthy differences in microstructure. First, sample images from the location 20-25mm of Exp A (5s Del.), which SDAS measurement indicated as a local hot spot, are shown in Figure 4-26. The microstructure of this region clearly shows large and densely packed dendrite arms reflecting its relatively slow cooling rate comparable to one shown in Figure 4-23. Sample images from the location 25-30mm of Exp A (5s Del.), which x-ray radiography indicated as the most common shrinkage porosity location, are shown in Figure 4-27. It is observed that there is a noticeable increase in portion of eutectic region compared to images shown in Figure 4-26. Surrounding these large pools of eutectic is a large number of fine dendrite arm structure. Some of the recorded measurements in these locations show a measurement as small as 24μm, which is more commonly found in regions much closer to the cooling circuit. Similar case is also observed in dendrite measurements of Exp C (35s Del.) and only difference being presence of visible porosity shrinkage in these pools of eutectic.

12 individual images from the location 25-30mm of Exp C (35s Del.) are combined together to show an example of the observation discussed previously. During solidification of rim and spoke junction, segregation of Si occurs due to possible thermal gradient across the rim and spoke junction. As a result of this segregation, a large pool of Si phase eutectic is evident in the location shown in Figure 4-28. Higher latent heat of Si than Al also means that the area of eutectic pool generates more amount heat. Therefore it is possible that this area remains much hotter than its surrounding region, where it contains relatively less amount of Si eutectic phase.

This suggests a possible limitation of using SDAS measurement to identify potential location of hot spot or solidification shrinkage. As shown in Figure 4-28, solidification shrinkage tends to occur at location where segregation of Si eutectic takes place and this is not indicated by simple measurement of SDAS. It is also important to note that x-ray radiography results shown in Figure 4-7 clearly shows increased number of shrinkage for Exp C, while SDAS results of Exp C failed to indicate.

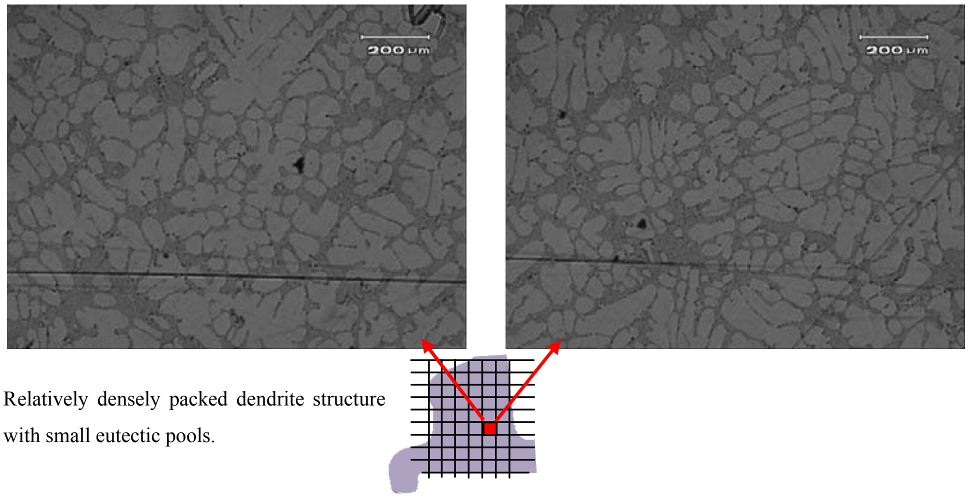

Relatively densely packed dendrite structure with small eutectic pools.

Figure 4-26 Sample images of hot spots identified by SDAS measurement.

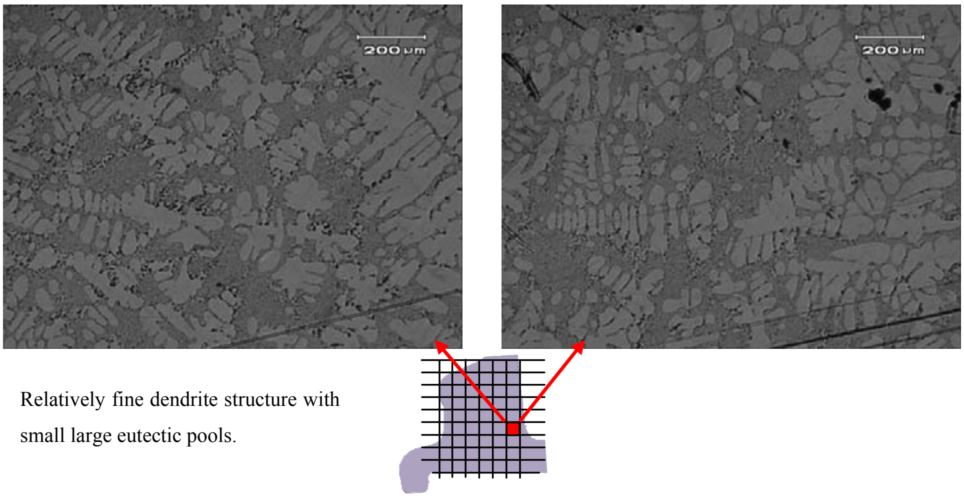

Relatively fine dendrite structure with small large eutectic pools.

Figure 4-27 Sample images of hot spots identified by x-ray radiography.

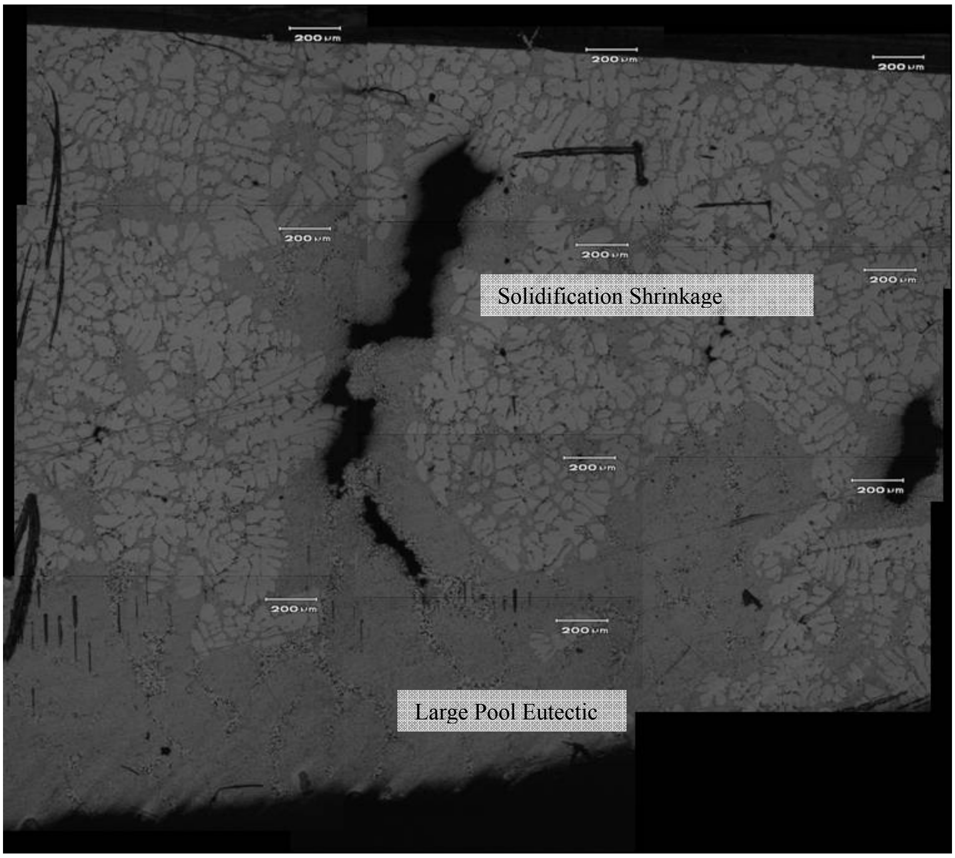

Figure 4-28 Combined images of an area where solidification shrinkage is found, shown in Figure 4-25.

4.3 Numerical Modelling

In this section of discussion, results of numerical modelling for both Exp A and C will be compared to experimental results to validate the effect of different cooling timing and numerical prediction of secondary dendrite arm spacing. Any identified limitations of numerical modelling will be discussed.

4.3.1 Processing of Results

Upon completion of numerical calculation, time and temperature data at each coordinate point specified was stored in text file format as shown in Figure 4-29. As shown in the figure, the results of numerical modelling are in a simple time and temperature format. As a part of an in-depth analysis, this data would need to be further processed and analysed.

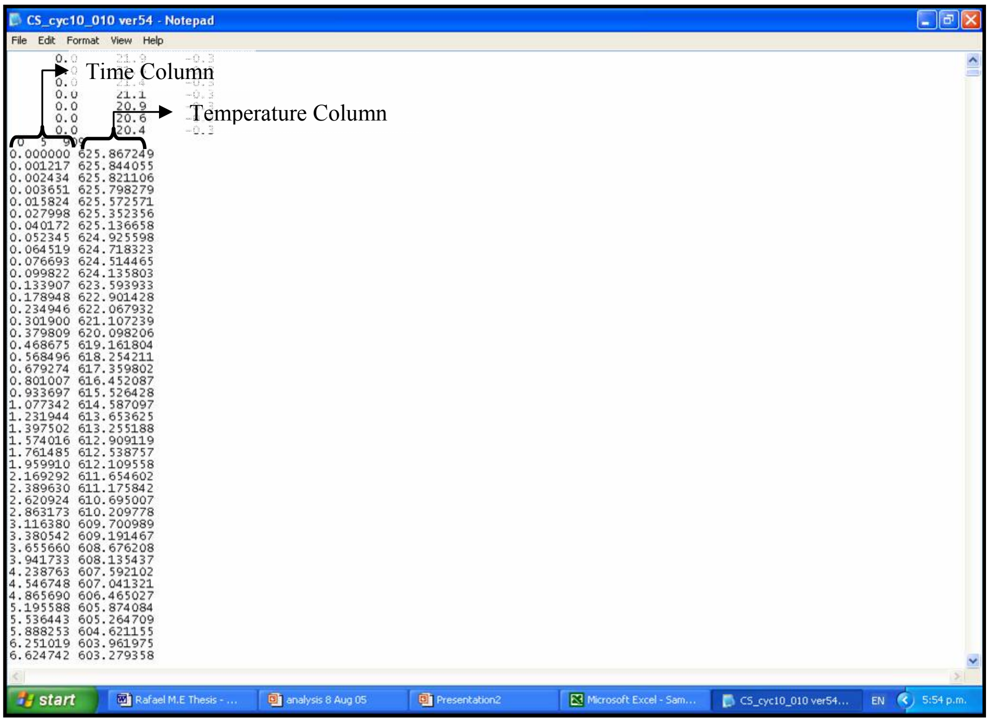

```
0.000000 625.867249
0.001217 625.844055
0.002434 625.821106
0.003651 625.798279
0.015824 625.572571
0.027998 625.352356
0.040172 625.136658
0.052345 624.925598
0.064519 624.718323
0.076693 624.514465
0.099822 624.135803
0.133907 623.593933
0.178948 622.901428
0.234946 622.067932
0.301900 621.107239
0.379809 620.098206
0.468675 619.161804
0.568496 618.254211
0.679274 617.359802
0.801007 616.452087
0.933697 615.526428
1.077342 614.587097
1.231944 613.653625
1.397502 613.255188
1.574016 612.909119
1.761485 612.538757
1.959910 612.109558
2.169292 611.654602
2.389630 611.175842
2.620924 610.695007
2.863173 610.209778
3.116380 609.700989
3.380542 609.191467
3.655660 608.676208
3.941733 608.135437
4.238763 607.592102
4.546748 607.041321
4.865690 606.465027
5.195588 605.874084
5.536443 605.264709
5.888253 604.621155
6.251019 603.961975
6.624742 603.279358
```

Figure 4-29 A sample image of typical data set from numerical modelling.

Time and temperature data was then imported to Microsoft Excel spreadsheet where local solidification time at each coordinate was calculated. Then using Kirkwood model, as shown in Equation 2-12 and Figure 4-30, secondary dendrite arm spacing (SDAS) was calculated. Detailed definition of local solidification time and its correlation with SDAS were discussed in the previous section, 2.4.2. Therefore any more detail of numerical modelling of SDAS based on solidification time calculation will not be discussed.

$$\lambda_2 = K(Mt_F)^{1/3}$$

Equation 2-12

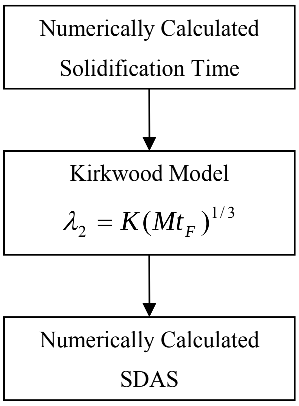

Figure 4-30 Steps of numerically modelling SDAS based on solidification time calculation results.

Again the chilled face, where casting comes in direct contact with cooling circuit, will be the main focus of analysis of numerical modelling of SDAS as in the previous section 4.2.2. The area of chill face is highlighted in Figure 4-31.

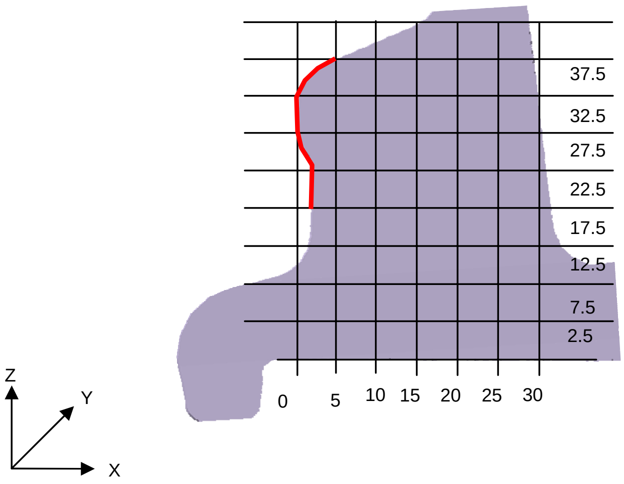

Figure 4-31 Locations of girds for analysis and the chilled face.

4.3.2 Discussions - Effect of Different Cooling Timings

A comparison of numerically calculated SDAS between Exp A and Exp C shows a very similar trend shown by their corresponding experimental data discussed previously in 4.2.2. An example of comparison plot is shown in Figure 4-32, clearly showing very insignificance difference in local cooling rate indicated by SDAS.

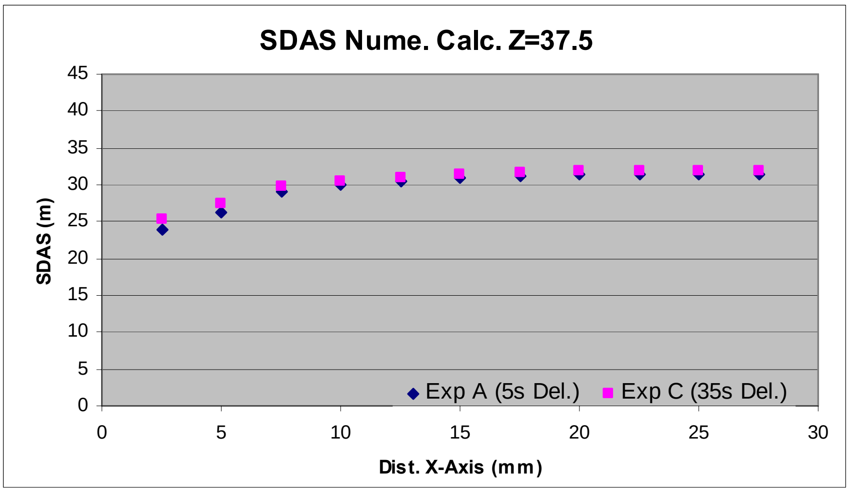

Figure 4-32 Comparison of numerically modelled SDAS for Exp A and Exp C.

This confirms the suggestion of reduced cooling circuit efficiency by air gap formation at the casting and cooling circuit interface. Empirically derived interfacial heat transfer coefficient at the casting and cooling circuit interfaces [17] as shown in Figure 4-33.

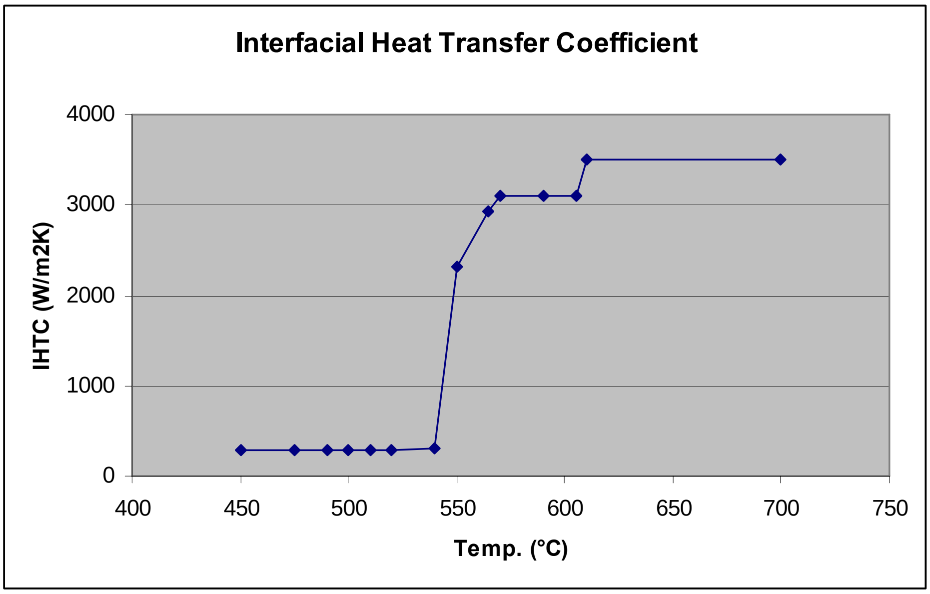

Figure 4-33 An example of interfacial heat transfer coefficient used for modelling air gap formation [17].

4.3.3 Discussions – Numerical Data vs. Experimental Results

Comparisons of numerically calculated SDAS, using the methodology shown in Figure 4-30, with experimentally measured SDAS are shown from Figure 4-34 to Figure 4-41. Results from both Exp A (5s Del.) and Exp C (35s Del.) are shown.

Analysis of Exp A (5s. Del.)

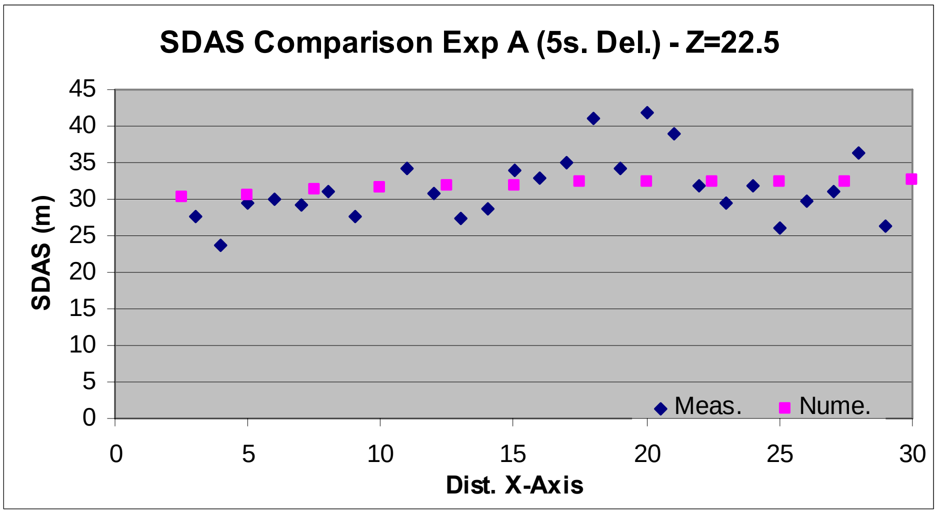

Figure 4-34 A comparison of numerically modelled and experimental measured SDAS for Exp A at Z=22.5.

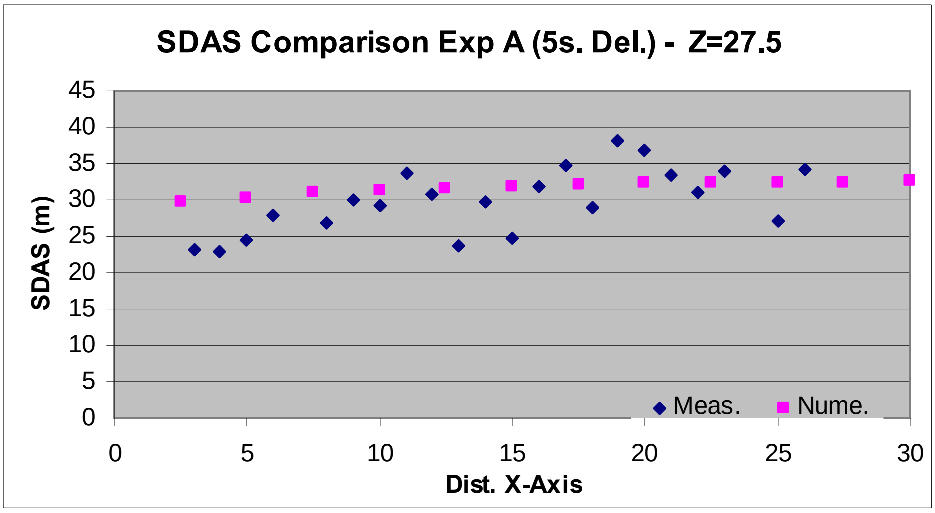

Figure 4-35 A comparison of numerically modelled and experimental measured SDAS for Exp A at Z=27.5.

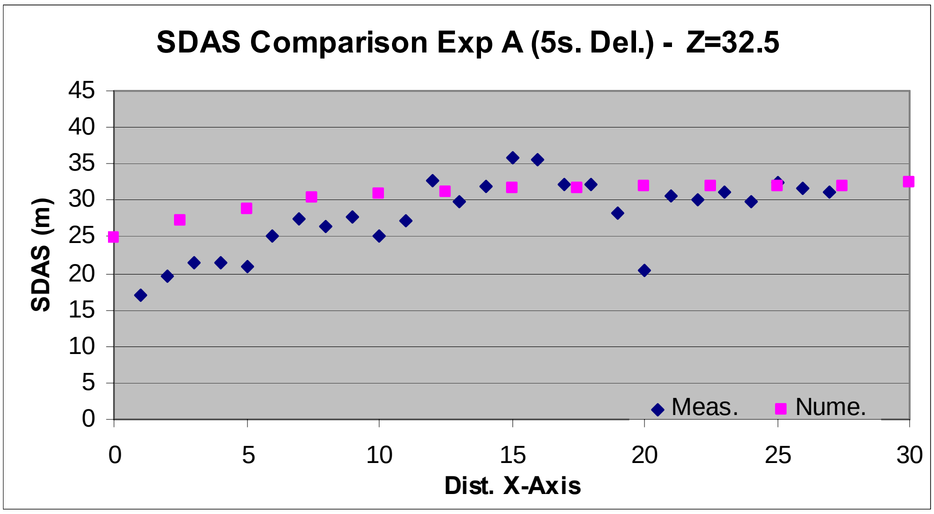

Figure 4-36 A comparison of numerically modelled and experimental measured SDAS for Exp A at Z=32.5.

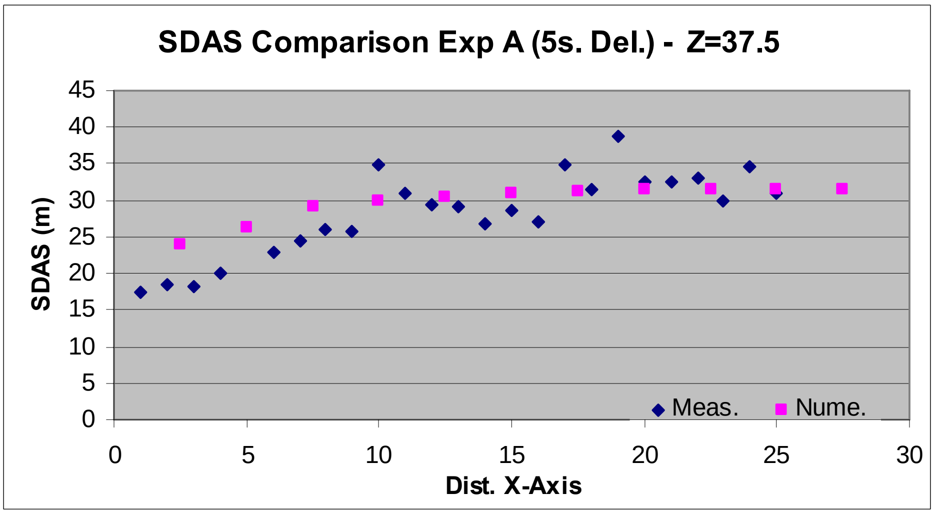

Figure 4-37 A comparison of numerically modelled and experimental measured SDAS for Exp A at Z=37.5.

Analysis of Exp C (35s. Del.)

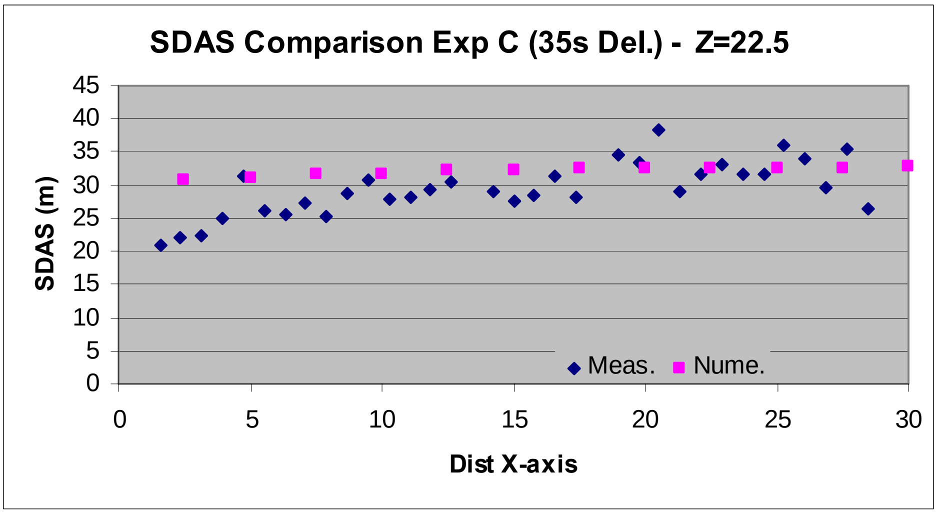

Figure 4-38 A comparison of numerically modelled and experimental measured SDAS for Exp C at Z=22.5.

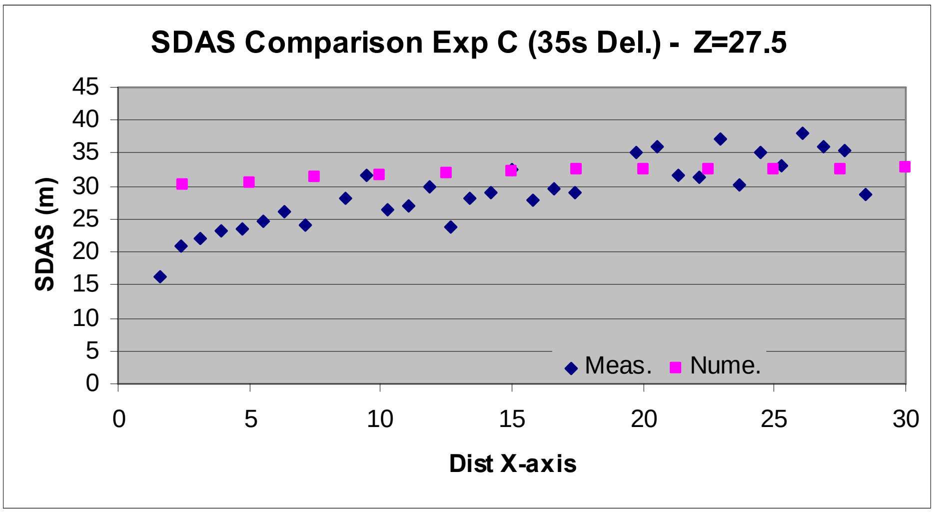

Figure 4-39 A comparison of numerically modelled and experimental measured SDAS for Exp C at Z=27.5.

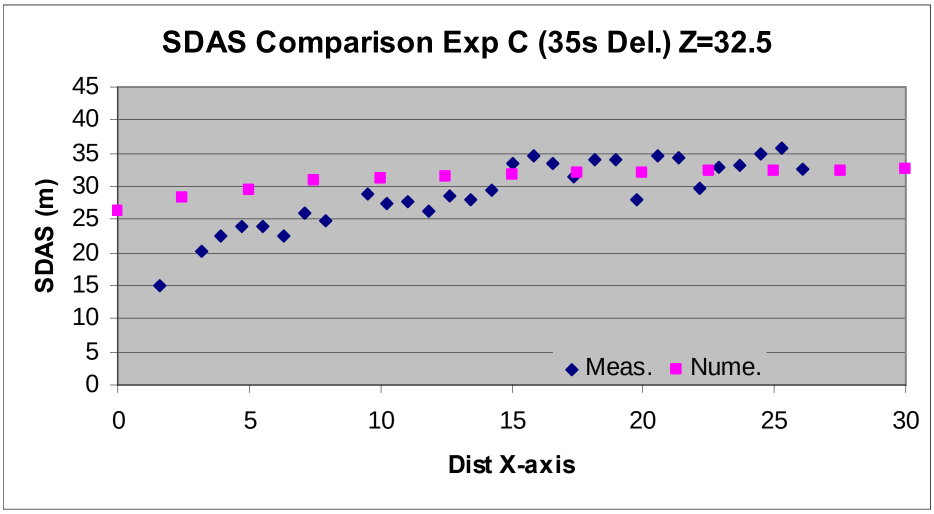

Figure 4-40 A comparison of numerically modelled and experimental measured SDAS for Exp C at Z=32.5.

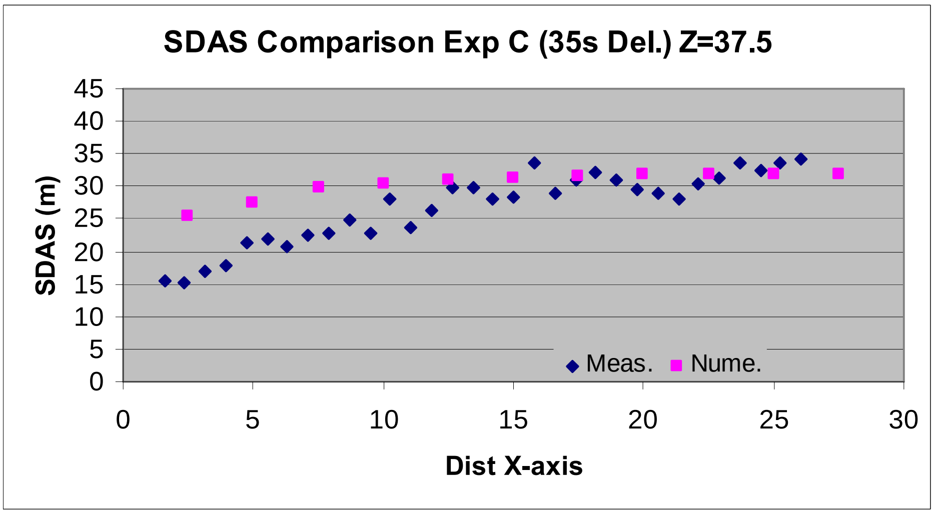

Figure 4-41 A comparison of numerically modelled and experimental measured SDAS for Exp C at Z=37.5.

A comparison between numerically calculated SDAS and measured values SDAS at various locations shows that areas of casting that are further away from chilled face demonstrated a reasonable agreement between and numerically calculated and measured values. This area corresponds to distance along x-axis between 15 and 30mm, where distribution of measured SDAS remains relatively constant along the x-axis. In contrast, a clear discrepancy between numerically calculated and measured SDAS values is shown in areas where its distance along x-axis is between 0-15 mm. This area, with clear discrepancy, is characterised by its rapid cooling rate as shown by its fine SDAS and referred to as chilled face.

The discrepancy between numerically calculated and measured SDAS at the chilled face area is shown by both experiments with different cooling timing settings (Exp A and Exp C). Therefore it is suggested that this discrepancy is not sensitive to cooling timing setting. The following limitations of the numerical modelling are suggested to explain this discrepancy.

1. Limitation of the current numerical modelling technique to analyse the influences of alloy modification methods commonly used in commercial alloys.

2. Limitation of numerical modelling in predicting microstructure, namely SDAS, in rapidly solidified region of casting due to homogeneous material property.

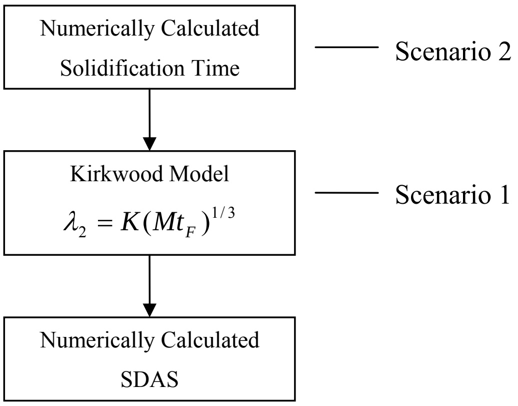

Figure 4-42 Suggested limitations of numerical modelling in predicting accurate SDAS at the chill face.

Limitation Numerical Modelling – Influences of Alloy Modification

The first case, shown as scenario 1 in Figure 4-42, is the potential of incorrect SDAS calculation due to incorrect use of ripening factor (or coarsening parameter). Ripening factor was used by Kirkwood model to numerically model the formation of SDAS as shown in Figure 4-30. The significance of ripening factor in Kirkwood model to describe the coarsening effect of secondary dendritic arms has been discussed in the literature review, in section 2.4.2. Although it was evident that the ripening factors for various alloys were reasonably well established, its applicability for commercial alloy was challenged [39].

There are several aspects of commercial alloys that could influence the coarsening effect of secondary dendrite arms. However, it is believed in this research that alloy modification treatment, particularly grain refinement, could be the most influential aspect. A suggested mechanism of how grain refinement can affect the coarsening behaviour of secondary dendrite arm is illustrated in Figure 4-43 and Figure 4-44.

First illustration of microstructure formation without grain refinement is shown in Figure 4-43. Nucleation of aluminium phase takes place and with a presence of adequate undercooling condition dendritic structure starts growing. Further coarsening of individual dendritic arm takes place until neighbouring arms impinge each other, reaching the fraction of solid known as dendrite coherency point. At this point overall impression of secondary dendrite arm spacing that particular condition is revealed, as impinged arms are locked and further growth is impeded.

In the case of microstructure formation with grain refinement, as shown in Figure 4-44, nucleation and coarsening of dendritic arms takes place using the same mechanism. However, the major difference is that the density of nucleation is much higher than the previous case due to presence of foreign particles, grain refiner, that act as additional nucleating sites. Higher density of particles then allows much less space for each dendritic particle to grow before it reaches dendrite coherency point. The result is that while both cases would reach the dendrite coherency point at a very similar fraction of solid, overall secondary dendrite arm spacing with grain refinement would be much smaller than the one without grain refinement.

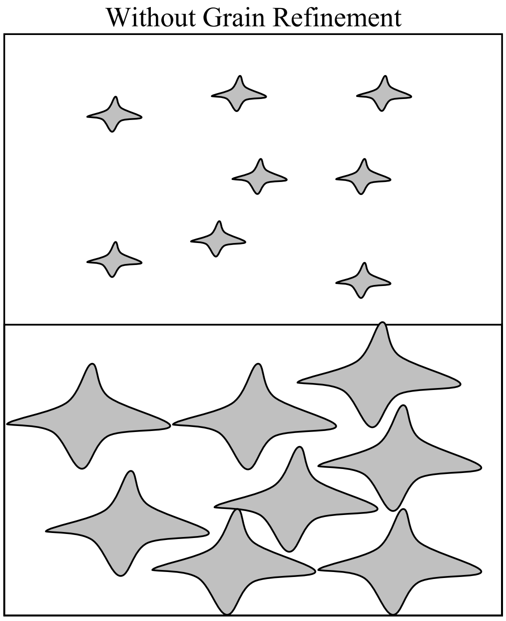
Without Grain Refinement

Less density of nucleated particles allows more room for an individual dendrite arm to grow before it reaches its coherency point. Therefore relatively large dendrite arm spacing.

Figure 4-43 Illustration of dendritic arm coarsening without grain refinement.

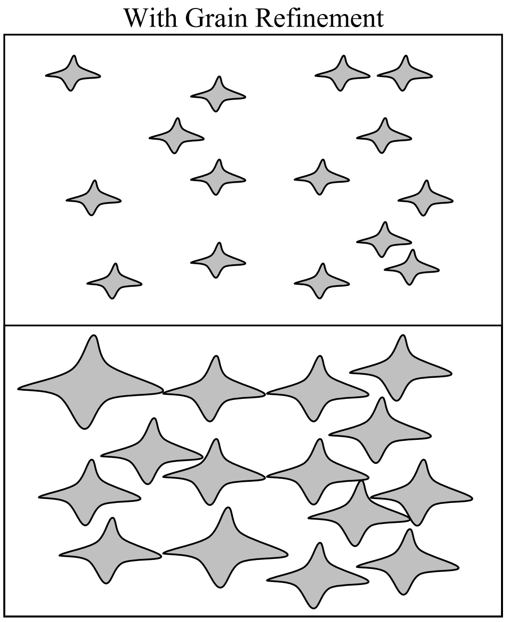

Higher density of nucleated particles, due to grain refinement, allows less room for an individual dendrite arm to grow before it reaches its coherency point. Therefore relatively fine dendrite arm spacing.

Figure 4-44 Illustration of dendritic arm coarsening with grain refinement.

It is shown in Equation 2-13, ripening factor (or coarsening parameter) of Kirkwood model is derived from the phase diagram of eutectic alloy. Therefore it is reasonable to suggest that Kirkwood model would have limited accuracy in predicting SDAS of commercial alloys with grain refining treatment used in this research.

Limitation of Numerical Modelling – Due to Homogeneous Material Property

The second case, shown as scenario 2 in Figure 4-42, is where incorrect solidification is predicted by numerical modelling used in this research. Further interrogation of numerical modelling shows its limitation in prediction of solidification time for an area with rapid cooling. Currently the material property of the modelling package is limited to homogeneous material property, where its material property does not vary upon local cooling rate. However, it is established that there are number of material properties, such as fraction of solid, that show significant changes depending the local cooling rate. Fraction of solid is particularly important in this research as it describes different stages of solidification process at different temperature. Detailed solidification process has been discussed previously, Section 2.4.2. Fraction of solid plots for Al-Si alloy with varying cooling rates, 0.2. 0.6 and 5°C/s, are shown in Figure 4-45. The current numerical modelling in this research applies fraction of solid plot at 0.6°C/s as a typical representation of cooling rate in casting applications. However, when rapid cooling experienced at the some part of the casting, it is reasonable to suggest that typical cooling rate at the chill face would be close to 5°C/s rather than 0.6°C/s in this case.

A comparison of fraction of solid plot between 5°C/s and 0.6°C/s, as shown in Figure 4-45, presents two distinctive differences. The first one is the differences in fraction of solid developed during solidification of aluminium, labelled Reaction 1. This part refers to transformation of liquid to Al phase as shown in Figure 2-13 and Table 2-1. It is evident that presence of increased cooling, in the case of 5°C/s cooling rate, allows increased undercooling. Therefore increased of amount of solid fraction is developed during this part of solidification process. Subsequently with reduced cooling rate, much less fraction of solid is developed, as shown in Figure 4-45.

The next part of solidification, labelled Reaction 2 & 2a, describes coarsening behaviour of dendritic arms (shown in Figure 2-13 and Table 2-2), hence determines SDAS. It can be seen from the plot that lower cooling rate, 0.6°C/s, would typically experience more coarsening takes place and fraction of solid increases from approximately 20% to 55%. Meanwhile, plot of 5°C/s shows relatively less volume of solid fraction developed during this phase, hence less coarsening of dendritic arms takes place.

Through this comparison, it is believed that use of homogeneous material property, where the same cooling rate of 0.6 °C/s is assumed for all parts of casting, could pose a significance limitation in accurate modelling of microstructure in the area of rapid cooling is experienced. The discrepancy shown between numerically modelled and experimentally measured SDAS at the chill face can be an example of this limitation.

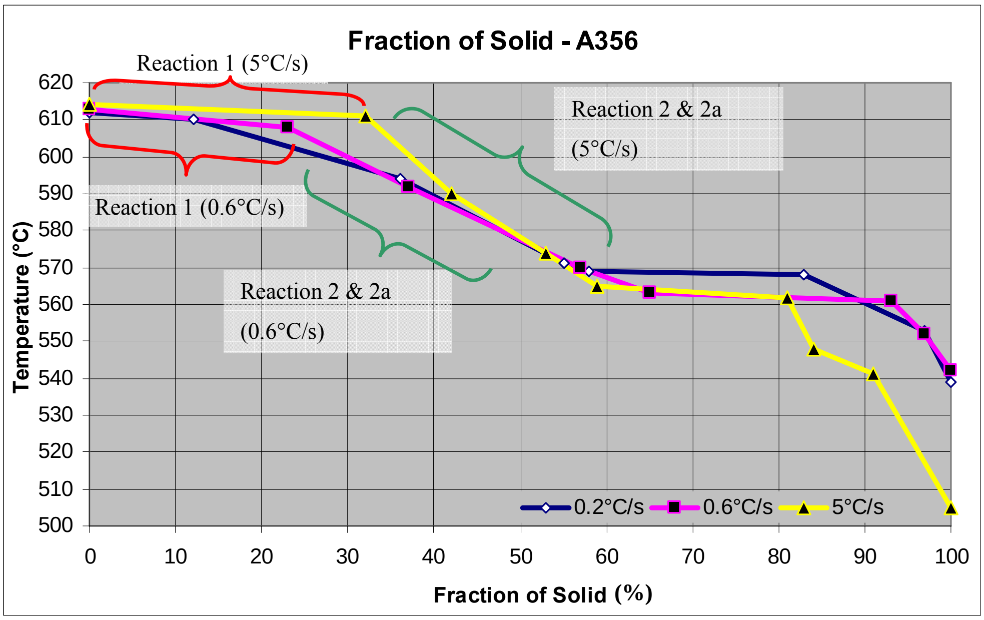

Figure 4-45 A comparison of fraction of solid plots for different local cooling rates.

5 Conclusions and Recommendations

Different cooling timing for rim and spoke junction of aluminium alloy wheel casting, as shown in Figure 1-8, was analysed to understand its effect on overall effectiveness of the thermal control. Casting experiments with different cooling timing settings were set to produce samples for secondary dendrite arm spacing measurements, where its relationship to local solidification time has been identified in the literature review. Also x-ray radiography of the same samples was conducted to qualitatively measure the level of shrinkage formation in the rim spoke junction. Numerical modelling of the casting experiment was also performed to validate the results of experiment and possibly suggests any limitations of numerical modelling to improve its accuracy and applicability in microstructure prediction.

The suggested findings are as follows.

1. Change in cooling timing between Exp A (5s Del) and Exp (35s Del) showed very minimal influence on local solidification time of rim and spoke junction area. Similar trend was observed in both experimental and numerical data. Rapid formation of air gap at the casting mould interface during solidification was suggested to explain this phenomenon.

2. Prediction of hot spot location (i.e. potentially shrinkage location) by SDAS measurement shows noticeable discrepancy, when compared with actual shrinkage location shown by x-ray radiography. Other microstrucral phenomena such as segregation of Si eutectic, which measurement of SDAS alone can not predict is suggested as a possible reason for this discrepancy.

3. Although numerical modelling successfully predicted the reduction in effectiveness of the thermal control by air gap formation, some possible

limitations were shown in predicting microstructure in certain areas. It was particularly noticeable in the area where rapid local cooling rate was experienced, such as the chill face (close to mould and casting interface). Two scenarios were presented in an attempt to explain this limitation, which were the limitation in modelling the effect of grain refinement and the limitation due to use of homogeneous material property.

Recommendations for further work are as follows.

1. Significance of air gap formation in determining the overall effectiveness of thermal control in casting system is suggested. It is recommended that the design of cooling circuits should consider possible direction of contraction of casting to minimise the effect of air gap formation and maximise the effectiveness of the thermal control.

2. Evident limitation of secondary dendrite arm spacing to predict location of hot spot suggests other microstrucral parameter. For the future research, it is suggested to develop a microstructure parameter related to Si eutectic segregation, such as fraction of eutectic etc.

3. It is recommended that further development of numerical modelling technique should consider the followings to increase its accuracy.

    a. Effect of grain refinement addition.
    b. Capability to model the segregation of Si eutectic combined with thermal analysis to provide better shrinkage location prediction.
    c. Capability to incorporate heterogeneous material properties for different local cooling within the casting.

Appendix A

X-ray Radiography Images.

Exp A

A1-1

A1-3

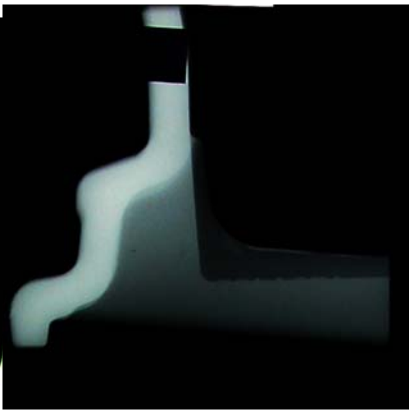

A1-5

A1-8

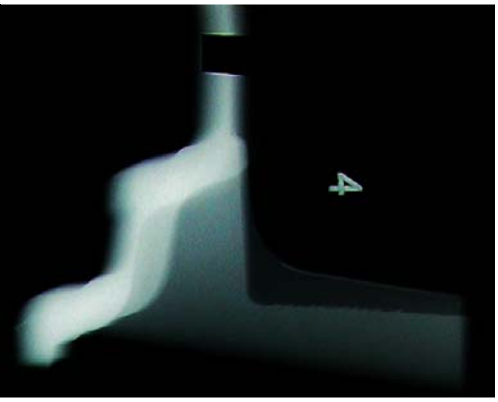

A1-10

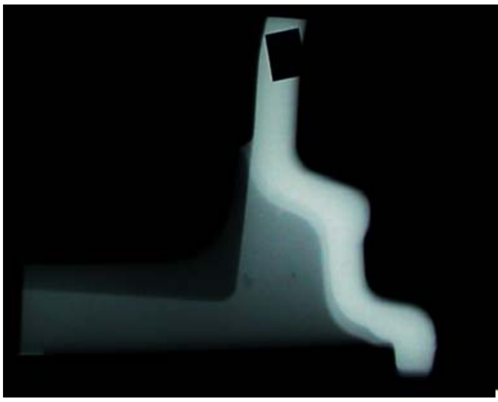

A1-12

A1-14

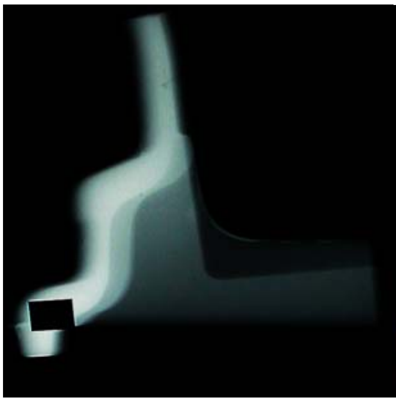

A4-1

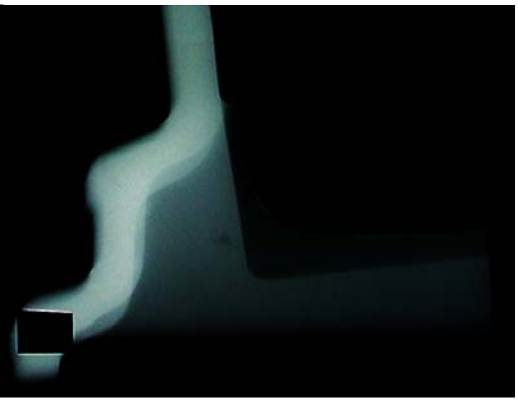

A4-3

A4-5

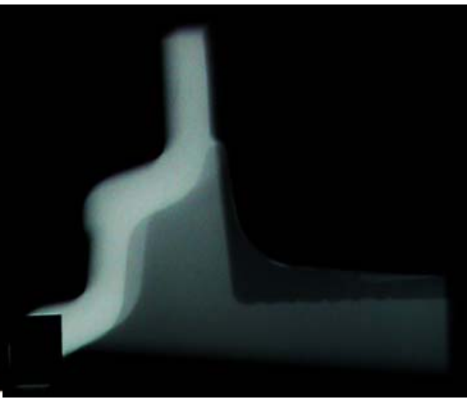

A4-8

A4-10

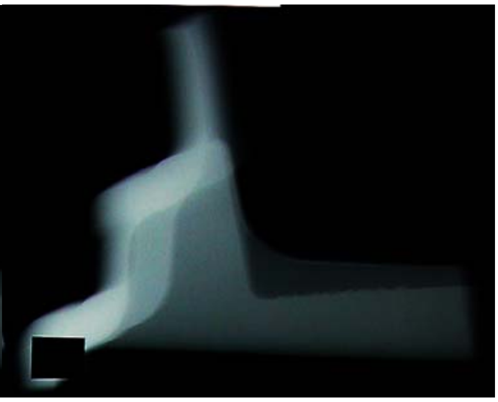

A4-12

A4-14

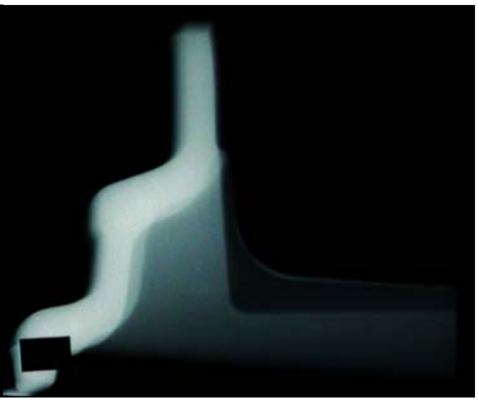

Exp B

B1-1

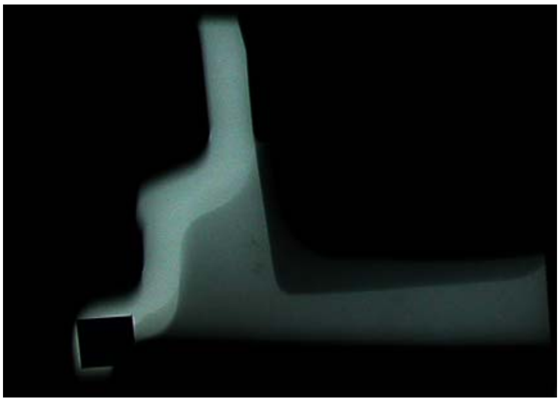

B1-3

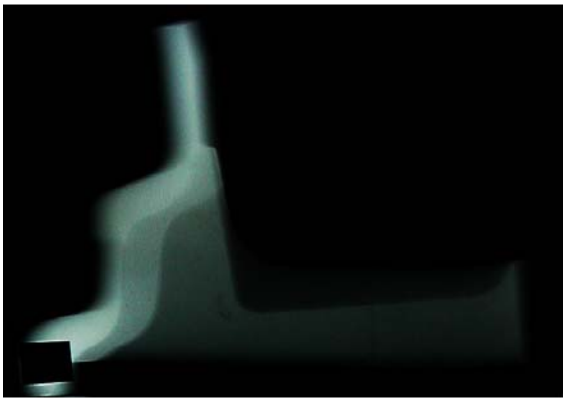

B1-5

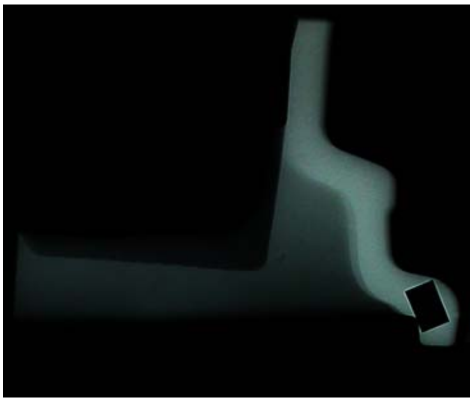

B1-8

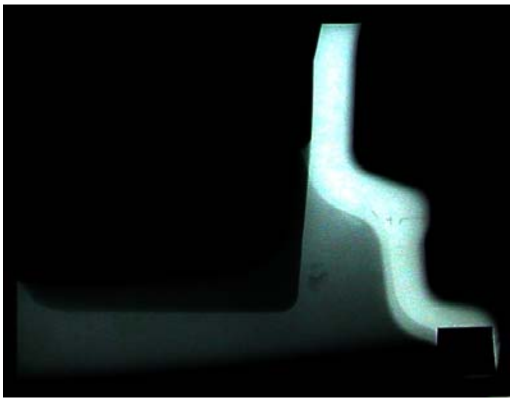

B1-10

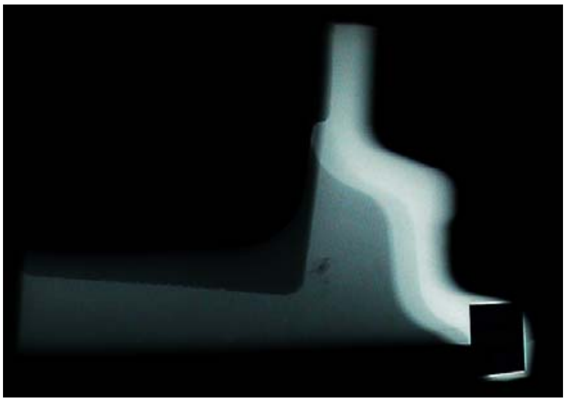

B1-12

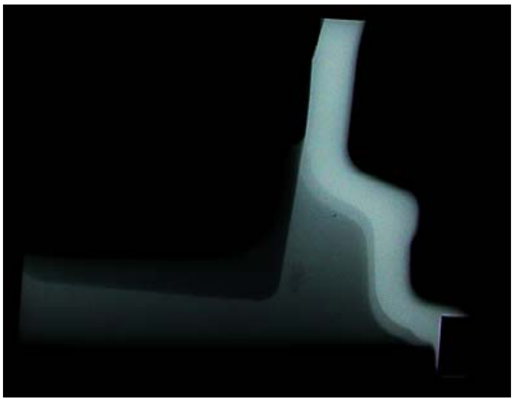

B1-14

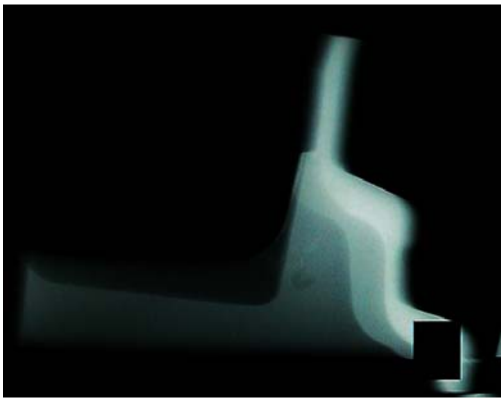

B4-1

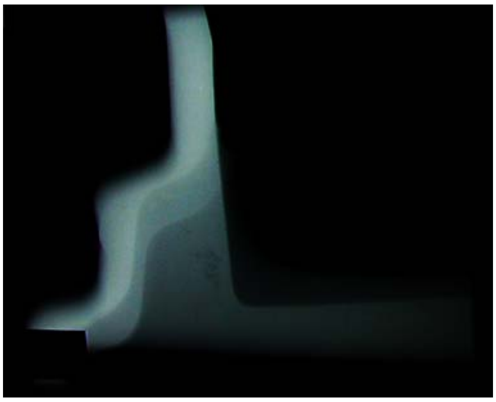

B4-3

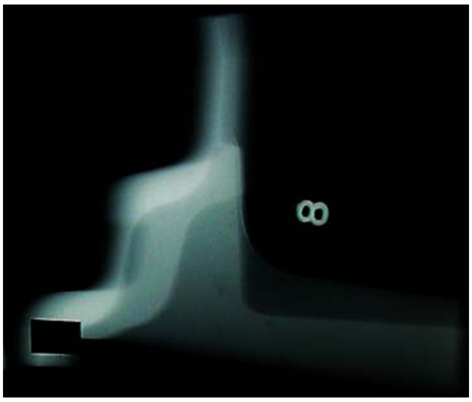

B4-5

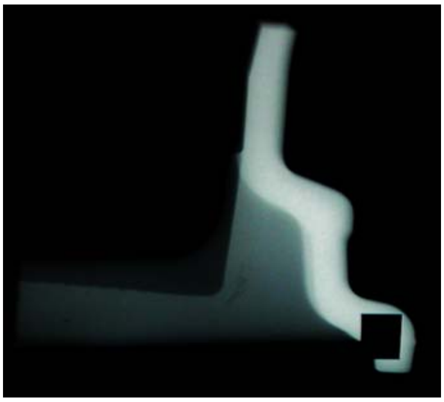

B4-8

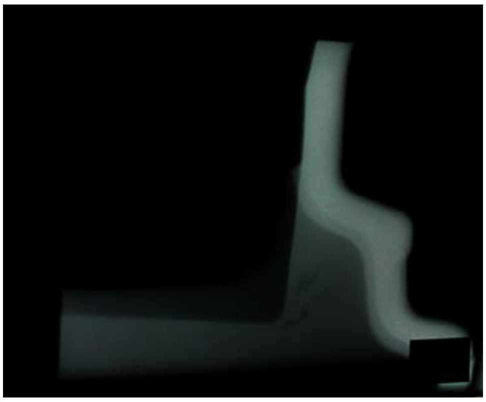

B4-10

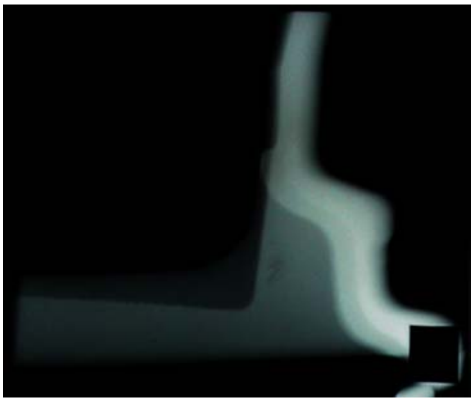

B4-12

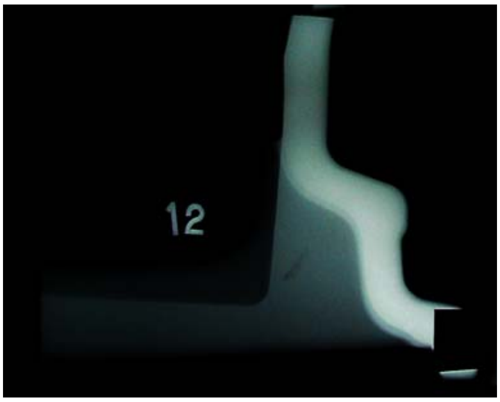

B4-14

Exp C

C1-1

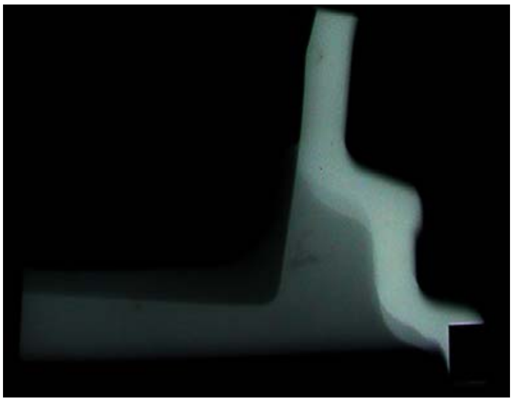

C1-3

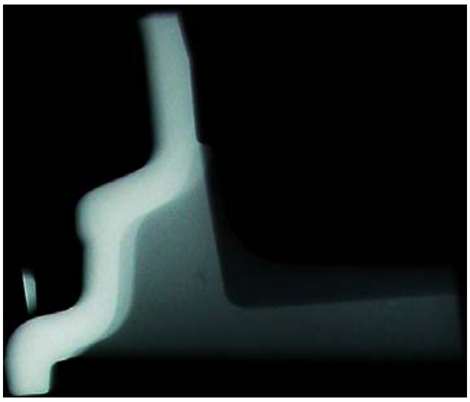

C1-5

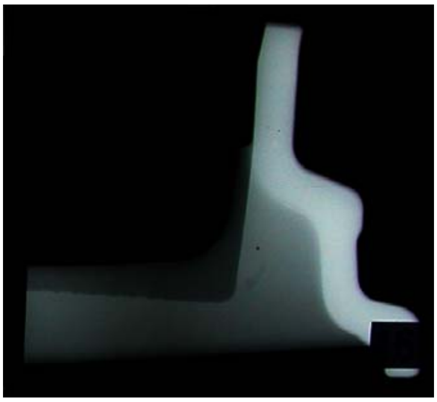

C1-8

C1-10

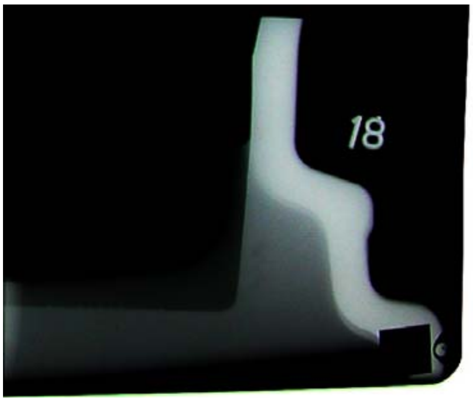

C1-12

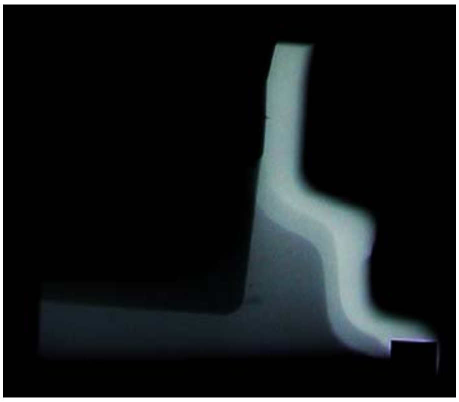

C1-14

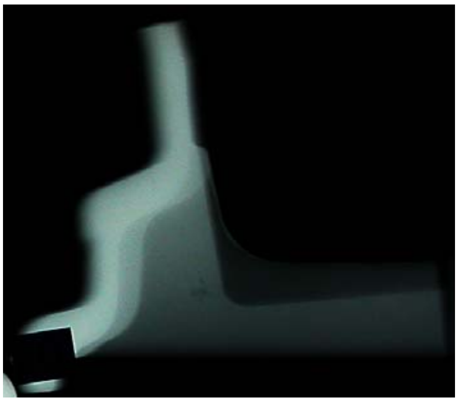

C4-1

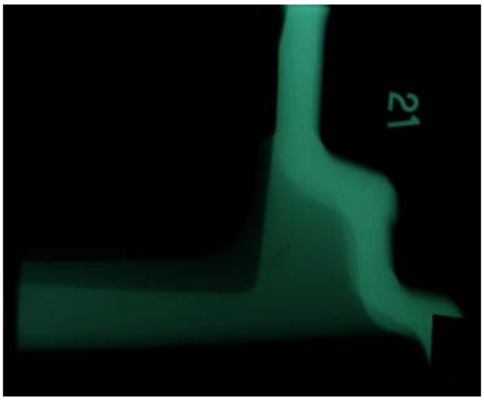

C4-3

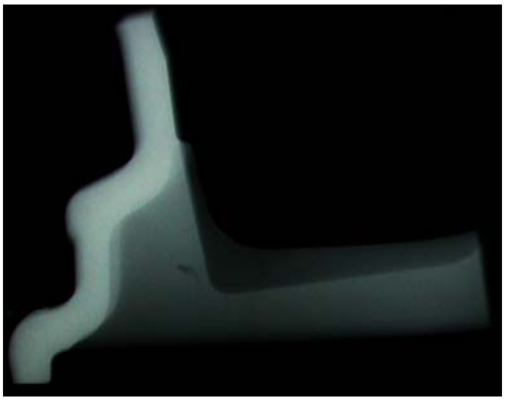

C4-5

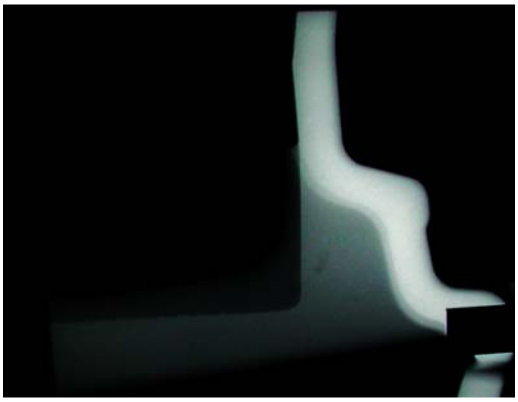

C4-8

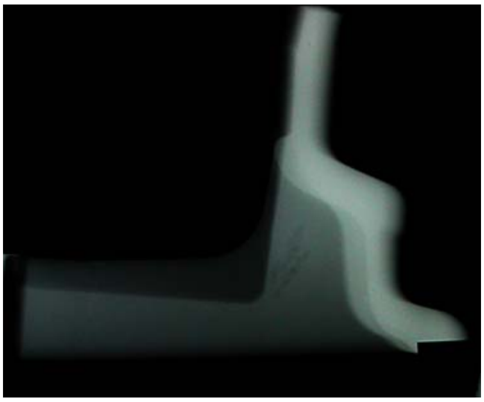

C4-10

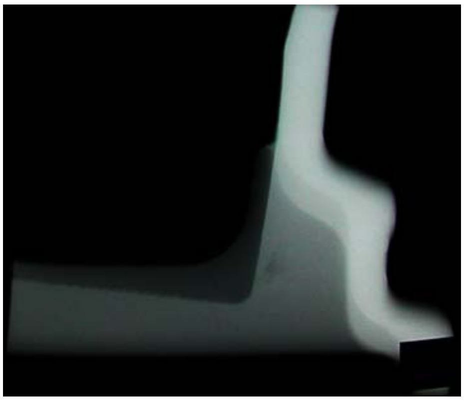

C4-12

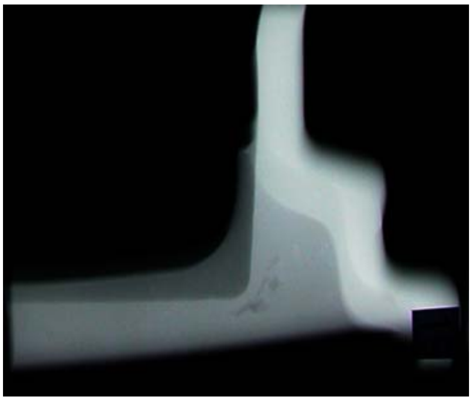

C4-14

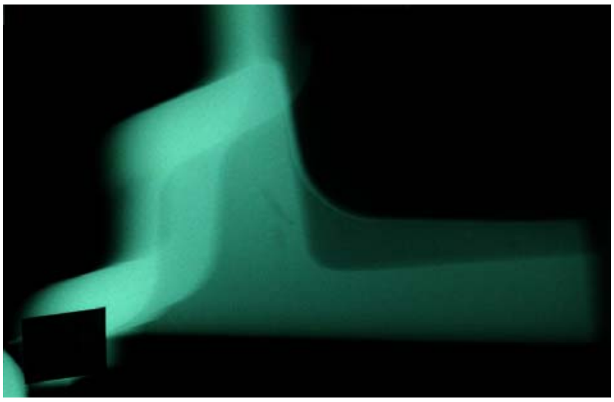

References

---

1 Bäckerud L, Chai G & Tammine J, *Solidification Characteristics of Aluminium Alloys:*USA, AFS/Skanaluminium, 1990, 128.

2 Stefanescu D. M, *ASM Hand Book: Vol. 15 Casting:*USA, ASM International, 1998.

3 Morikawa T, Niyama E, Saito S & Uchida T, *AFS International Cast Metals Journal*, 1982, September, 52-63.

4 Suri V. K. & Paul A. J, Modelling and Prediction of Micro/Macro Scale Defects in Castings: In Proceeding of 97th Casting Congress, American Foundry Society, Chicago, Illinois, USA, 1993, 93-144.

5 Hansen P. N., Sahm P. R. & Flender E., How to Select and Use Criterion Functions Solidification Simulation: In Proceeding of 97th Casting Congress, American Foundry Society, Chicago, Illinois, USA, 1993, 93-051.

6 Huang H. & Berry J. T., Evaluation of Criteria Functions to Minimise Microporosity in Long Freezing Range Alloys: In Proceeding of 97th Casting Congress, American Foundry Society, Chicago, Illinois, USA, 1993, 93-115.

7 Suri V. K., Huang H., Berry J. T. & Hill J. L., Applicability of Thermal Based Criteria to Long Freezing Range Aluminium Alloys: In Proceeding of 96th Casting Congress, Milwaukee, Wisconsin, USA, 1992, 92-165.

8 Taylor R. P., Berry J. T. & Overfelt A., Parallel Derivation and Comparison of Feeding Resistance Porosity Criteria Functions for Castings: In Proceeding of ASME 31st National Heat Transfer Conference, 1996, Vol. 1, 60-77.

---

9 Spittle J. A., Almeshhedani M. & Brown S.G. R., Cast Metals, 1994, vol. 7 – 1, 51-56.

10 Taylor R. P., Shenefelt J., Berry J. T. & Luck R., American Foundry Society Transactions, 2002, 02-042.

11 McLaughlin M. Kim C. W. & Kubo. K., American Foundry Society Transactions, 2002, 02-140.

12 Y. S. Çengel, “Heat Transfer – A Practical Approach”, McGraw-Hill, 141.

13 Beck J. V., Blackwell B. & Haji-Shekh A., Int. J. Heat Mass Transfer, 1996, vol 39, No. 17, 3649-3657.

14 Krishnan M. & Sharma D. G. R., Int. Comm. Heat Mass Transfer, 1996, Vol. 23, No. 2, 203-214.

15 O’Mahoney D. & Browne D. J., Experimental Thermal and Fluid Science, 2000, vol. 22, 111-122.

16 Huang ,C. H., Ozisik M. N. & Sawaf B., Int. J. Heat Mass Transfer, 1992, Vol. 35, No. 7, 1779-1786.

17 Singh, D. P. K., Palle, N., Mallinson, G. D. & Panton, S. M., Reducing the Cycle Time in Die Casting Using Solidification Modelling and Optimisation Techniques, in Proceedings of the International Modelling, Casting, Welding and Advanced Solidification Processes, 1998, Vol. VIII, B., San Diego, USA, 999-1007.

18 Booth S. E. & Allsop D. F., Transaction of 12th SDCE Congress, Cleveland, Ohio, USA, G-T81-056.

---

19 Manilal P., “Thermal Control of Dies”, B.E Final Year Report, Auckland University of Technology, Auckland, New Zealand, 2001.

20 Ho K. & Pehlke R. D., American Foundry Society Transactions, 1983, 83-080.

21 Prates M. & Biloni H., Met. Transactions 3A, 1972, 1501-1510.

22 Ho K. & Pehlke R. D., American Foundry Society Transactions, 1984, 84-061.

23 Ho K. & Pehlke R. D, Metallurgical Transactions B, 1985, 585-594.

24 Rapier A. C., Jones T. M. & McIntosh J. E., International Journal of Heat Transfer, 1963, Vol. 6, 397-416.

25 Muojekwu C. A., Samarasekera I. V. & Brimacombe J. K., Metallurgical and Material Transactions B, 1995, Vol. 26B, April, 361.

26 Gafur M. A., Haque M. N., & Prabhu K. N., Journal of Materials Processing Technology, 2003, Vol. 113, 257-265.

27 Michel F., Louchez P. R. & Samuel F. H., Heat Transfer Coefficient (H) during Solidification of Al-Si Alloys: Effect of Mould Temperature, and Coating Type and Thickness. In Proceeding of 99th Casting Congress, American Foundry Society, Kansas City, Missouri, USA, 1995, 95-009.

28 Carroll M., Walsh C. & Makhlouf M., Determination of Unidirectional Heat Ttransfer Coefficient during Unsteady-state Solidification at Metal Casting –Chill Interface**,** In Proceeding of Cast Expo, American Foundry Society, St. Louis, Missouri, USA, 1999, 99-148.

---

29 Santos C. A., Quaresma J. M. V.& Garica A., Journal of Alloys and Compounds, 2001, Vol. 319, 174-186.

30 Prabhu K. N. & Ravishankar B. N., Materials cience and Engineering, 2003, Vol. A 203, 293-298.

31 Chiesa F., American Foundry Society Transaction,1990, 90-010.

32 Kim T-G. & Lee Z-H., Int. Journal of Heat Mass Transfer, 1997, Vol. 40. No. 15., 3513-3527.

33 McDavid R. M. & Dantzig J. A., Interfacial Resistance in Foundry Castings. 1995.

34 Campbell, J., Castings, 2nd Edition, Butterworth-Heinemann Ltd., Oxford, 1991.

35 Bardes B. P. & Flemings M. C., American Foundry Society Transactions, 1966, Vol. 74, 406-412.

36 Flemings M. C., Kattamis T. Z. & Bardes B. P., American Foundry Society Transaction, Silver Anniversary Paper, Aluminium Div. 2, 1995.

37 D. H. Kirkwood, Mater. Sci. Eng. 1985, Vol. 73, L1-L4.

38 Peres M. D., Sequeria C. A. & Garcia A., Journal of Alloys and Compounds, 2004, Vol. 381, 168-181.

39 González-Rivera C., Campillo B., Castro M., Herrera M. & Juárez-Islas J., Materials Science and Engineering, 2000, Vol. A279, 1499-159.

---

40 Okamoto T. & Kishitake K., Journal of Crystal Growth, 1975, Vol. 29, 137-146.

41 MAGMASoft™ User Manual, MagmaSoft, 2003.